2024

MICROSTRUCTURAL FINITE ELEMENT MODELING OF HIGH-PERFORMANCE CARBON FIBER-REINFORCED COMPOSITES TO CHARACTERIZE MICROSCALE MATERIAL PROPERTIES AND FIBER-DIRECTION COMPRESSIVE STRENGTH

Quy Tung Ling Vu

MICROSTRUCTURAL FINITE ELEMENT MODELING OF HIGH-PERFORMANCE CARBON FIBER-REINFORCED COMPOSITES TO CHARACTERIZE MICROSCALE MATERIAL PROPERTIES AND FIBER-DIRECTION COMPRESSIVE STRENGTH

by

QUY TUNG LINH VU

DISSERTATION

Submitted in partial fulfillment of the requirements
for the degree of Doctor of Philosophy at
The University of Texas at Arlington
International cotutelle with ISAE-Supaero, MEGEP, Toulouse, France

December, 2023

Arlington, Texas

Dissertation Committee:

Andrew Makeev, Supervising Professor
Erian A Armanios
Endel Iarve
Paul Davidson
Frédéric Lachaud, Supervising Professor
Yves Gourinat, Supervising Professor
Christian Hochard, External Referee
Marco Gigliotti, External Referee

ABSTRACT

MICROSTRUCTURAL FINITE ELEMENT MODELING OF
HIGH-PERFORMANCE CARBON FIBER-REINFORCED COMPOSITES
TO CHARACTERIZE MICROSCALE MATERIAL PROPERTIES
AND FIBER-DIRECTION COMPRESSIVE STRENGTH

Quy Tung Linh Vu, Ph.D.

The University of Texas at Arlington, 2023

International cotutelle with ISAE-Supaero, MEGEP, France

Supervisors:

Andrew Makeev

Guillaume Seon

Frédéric Lachaud

Miguel Charlotte

Yves Gourinat

Carbon fiber-reinforced composites are increasingly used in aerospace application thanks to their excellent specific stiffness and strength. However, incomplete understanding of their failure behaviors leads to composite components often being designed with a high Safety Factor, limiting their advantages. Using computational methods, this project studies carbon fiber-reinforced composite microstructures for the objective of understanding and improving material performances under compression load which is one of the main considerations in primary aerospace structure design. A Finite Element (FE) model for the evaluation of composite compression behaviors was

developed, allowing the identification of several key material properties affecting composite performance.

The numerical micromodels require information of the microscale components including the reinforcing fibers, the matrix and the fiber-matrix interface. An extensive literature review was done on the microscale component properties including their potential impact on composite strength. Combined with results from the FE modeling, a strategy was decided where the assessment of important material properties was given priority.

Several authors, numerically and experimentally, demonstrated the significant impact of microscale residual stress on composite strengths. Yet, there was no established method for the characterization of residual stress in matrix at microscale. This project proposes a new method for the assessment of microscale residual stress in composite matrix. The new method is based on the fiber push-out experiment that creates local matrix deformation induced by the relaxed stress and evaluation by the Finite Element Method Updating technique for the inverse characterization of residual stress field in the corresponding specimen.

Literature review and FE modeling results identified the Interfacial Shear Strength (IFSS) as a key material property affecting composite strength. Meanwhile, the IFSS measurement using the standard push-out method suffers from several unwanted effects, potentially lowering its accuracy. These effects were analyzed using FE modeling. Notably, the results suggest that the effect of microscale residual stress on the IFSS measurement is rather insignificant.

ACKNOWLEDGEMENTS

I would like to express my gratitude to my supervisors: Dr. Guillaume Seon, Professor Frederic Lachaud, Professor Miguel Charlotte, Professor Yves Gourinat and Professor Andrew Makeev for their guidance, advice, and support during my PhD project.

I would like to thank the members of my Supervisory Committee and Dissertation Committee: Professor Erian Armanios, Professor Paul Davidson, Professor Endel Iarve, Professor Warda Ashraf, Professor Christian Hochard, and Professor Marco Gigliotti for their insightful comments and reviews.

I would like to thank my colleague, Dr. Sarvenaz Ghaffari, for her help and for the cooperation with my research. Dr. Ghaffari provided significant experimental data which helped with verification and validation of my hypotheses and numerical results.

I would like to thank my colleague, Mr. Brian Shonkwiler, for his insights into the experimental aspects of composite materials behaviors and for providing experimental data which helped with development and verification of my numerical models.

I would like to thank my colleague, Dr. Yuri Nikishkov for his helpful advice on the application of various mathematical and computational techniques in my research topic.

I would like to thank my friends, Mr. Hong Anh Vu and Dr. Thanh Huy Nguyen for the excellent discussions and advice regarding mathematical aspects and computational techniques which were subsequently applied to my research project.

The PhD project received full funding through Research Assistantships from the ISAE-Supaero, France and the University of Texas at Arlington, USA.

This research was partially funded by the U.S. Government under Agreement No. W911W6-17-2-0002. Such support is gratefully acknowledged. The U.S. Government technical monitor is Dr. Mahendra Bhagwat. The views and conclusions contained in this document are those of the author and should not be interpreted as representing the official policies, either expressed or implied, of the U.S. Government.

DEDICATION

In addition to the academic assistance directly related to this scientific work, I received valuable support and inspiration in life in the upcoming of and during my time as PhD student.

I would like to thank my family who have always been beside me during my academic adventure. My grandparents, grand aunt, and grand uncle, for teaching me the value of education, the love for sciences and the aspiration for academic achievements. My parents, for not only giving me a strong body and a smart brain, but also teaching me the value of hard work, independence and integrity which all scaled so well into my life as an engineer and a scientist. My aunts and my uncles, for the encouragement, the helpful advice and teaching, and for lending me their wisdom, all free of charge. My little sister and my cousins, for the fun we shared and the discussions on different aspects of life with various levels of seriousness. Nhon The British Longhair, for the unlimited amount of entertainment over my long honorable years in the quest for the graduate degrees.

I would like to thank my dearest cutest girlfriend Lan Lam Le, for the love and care, for the memories we made together, for patiently watching me slowly graduating from a high school cowboy into a slightly wiser man today. Trying to express my gratitude to you, words don’t come easy.

All through my education, I have been blessed with excellent teachers. I would like to thank my professors and advisors Guillaume Seon, Frederic Lachaud, Miguel Charlotte, Yves Gourinat and Andrew Makeev for their teaching in sciences, in aerospace engineering, in airmanship, and for the wisdom they lent to me. I would like to thank my physics teacher Cong Toan Nguyen and my math teacher Thi Nhuy Dam, for not only teaching sciences to the younger me, but also offering me continuous advice and encouragements throughout my academic voyage.

My special thanks go to my teachers, mentors, senior fellow graduates Guillaume and Yves for showing me the way. Your wise words at the direst of times were and still are a treasure.

My deepest gratitude goes to my godfather Jean-Jacques Augier for the guidance, encouragement and inspiration to pursue my dreams in life.

My deepest gratitude goes to my life mentor Thoa Nguyen for the words of wisdom and the inspiration to follow through hardship and achieve what is dearest in life.

I would like to express my special appreciation to my brothers-in-arms, Hong Anh Vu and Thanh Huy Nguyen. Our brotherhood that was forged through thousands of hours of combat for the Defense Of The Ancient certainly is immortal.

I would like to convey my special gratefulness to my bros-at-lab, Louis Sponton, Maksim Larionov and Abdullah Metiner. Our brotherhood that was hardened through science, engineering, culture and inflation shall be eternal. I would like to express my special gratitude to my friends and colleagues Brian Shonkwiler, Yuri Nikishkov, Sarvi Ghaffari and Bastiaan van der Vossen. The time we shared contributed to the shaping of my PhD student life into a The-Big-Bang-Theory-like experience.

I would like to mention my wonderful friends, Pham Truong Son, Thi Thu Hien Nguyen, Thi Thanh Huyen Nguyen and Phuong Anh Nguyen, for the timely precious support at the hardest moment of my life. Words fail to express my gratitude towards everything that they have done for me.

I would like to express my deepest gratitude to my new friends (no longer new at the moment of writing of this document), Duc Tam Vu, Quang Truong Pham, Kieu Trinh Pham and Phuong Mai Trinh, for having appeared at a critical time of my life, offering valuable help and support such that we might soon have a Dr. Vu Quy reborn.

List of Abbreviations

For the sake of brevity, in this document, the term “composite” refers to the Fiber-Reinforced Composite (FRC) which is the main object of study of this project.

For a quick reference, below is a list of common abbreviations utilized in this document.

BC	Boundary Condition
CFRP	Carbon Fiber-Reinforced Polymer
CDP	Concrete Damaged Plasticity
CTE	Coefficient of Thermal Expansion
DIC	Digital Image Correlation
DOC	Degree of Cure
FE	Finite Element
FEM	Finite Element Method
FEMU	Finite Element Method Updating
FRC	Fiber-Reinforced Composite
HM	High-Modulus
IFSS	Interfacial Shear Strength
IM	Intermediate-Modulus
PBC	Periodic Boundary Conditions
RVE	Representative Volume Element
SEM	Scanning Electron Microscope
UD	Uni-Directional

Table of Contents

CHAPTER 1
Introduction

1.1. Background

The composite materials are finding increasing usage in aerospace engineering, particularly in the vertical lift aircraft structures, thanks to their superior stiffness and strength for a given weight. However, the optimization of composite structures still suffers from the incomplete understanding of their damage mechanism and their often sudden and brutal failure. As a result, composite structures are often designed with a high safety factor, limiting their advantages in weight-saving applications.

Amongst the design constraints of the aerospace primary structures, component compressive strength including post-damage residual compressive strength has been one of the main considerations [1]–[7], especially in the development of aircraft with high use of lightweight composites including the traditional fixed-wing aircraft and the newer tiltrotor vertical lift aircraft [5], [7], [2]. Fiber-direction compression strength of common aerospace fiber-reinforced composites is significantly lower than tension strength, while the understanding of the mechanism of compression failure is incomplete. The high demand for high-performance composites in aerospace engineering, coupled with their weakness in axial compression strength and the incomplete understanding of this important failure mode, prompted very active research seeking better knowledge on axial compressive failure mechanism and improving axial compressive strength in new composite materials [8]–[18].

Recent development of High-Modulus (HM) Carbon Fibers permits stiffer carbon-fiber reinforced plastic (CFRP) composites compared to the legacy Intermediate-Modulus (IM) Carbon Fibers, promising applications in manufacturing even lighter-weight aerospace components. However, these HM-based composites suffer from lower compression strength in fiber-direction than traditional IM-based materials. Coupling with their well-known sudden and brutal rupture characteristics, this complicates the design of aerospace components using these novel HM-based CFRPs.

To overcome the weaknesses of HM composites, researchers at AMSL-UTA developed a hybrid composite with a mixture of HM and IM fibers. The result is promising: the hybrid material possesses higher Modulus (stiffer), all the while having only a small reduction in fiber-direction compression strength [17]. It is important to note that hybridizing fibers in a composite is not a straightforward task: in some cases, hybrid composite is weaker than its parent, such as the glass-carbon composite [9].

This PhD project is part of an effort at the AMSL laboratory at Department of MAE, UTA with cooperation from the international partner DMSM-ICA laboratory, ISAE-Supaero (Toulouse, France) for the development of diagnostics and prognosis methods relying upon 3D imaging and performance prediction based on computational tools. The new methods might offer significant reduction of costly and lengthy experimental iterations in the development of new composites through the (1) – high-fidelity 3D non-destructive measurements; (2) – experimental methods to determine key material properties; and (3) – computational techniques relying on key structure and material properties to predict lifetime performance.

This PhD project focuses on the study of composite at microscale using numerical methods to evaluate effects of microscale component properties (fiber, matrix, interface etc.) on the macroscale composite properties. As key microscale properties affecting composite performance are gradually identified, the project seeks to propose, evaluate, and calibrate experimental methods for the measurement of these microscale properties using computational tools.

1.2. Objectives

Chapter 2 deals with the fiber-direction compression failure of Uni-directional (UD) composites. An extensive literature review is provided, including existing analytical, numerical and experimental studies, offering some clues on the potentially important material properties and effects to be considered in the FE modeling of the phenomenon. The FE models and numerical results are then presented along with some conclusions and suggestions for future works on the topic.

Chapter 3 deals with material properties and material models at microscale. An extensive literature review on both the relevant microscale material properties and their measurement methods is provided. Some material properties are identified as critical to the composite performance. The PhD works on some of the identified-as-important material properties are presented.

Chapter 4 deals with the microscale residual stress in the composite, where a new method for the characterization microscale residual stress is proposed. Literature reviews suggest the very significant effects of microscale residuals stress on the composite performance. Combined with the lack of experimental measurement method at the time, this study was given a high priority in the PhD project. The new method for microscale residuals stress characterization consists of the fiber push-out experiment where matrix deformation due to stress relaxation are evaluated using the Finite Element Method Updating (FEMU) for the reproduction of the residual stress field in the FE models. Results, the ongoing work along with proposals for future improvements are presented.

Chapter 5 deals with the calibration of the Interfacial Shear Strength (IFSS) measurement using the fiber push-out method. Results from Chapter 2, supported by other studies from the literature, indicate a strong effect of the IFSS on the composite fiber-direction compression strength. At the same time, the IFSS measurement using the common fiber push-out method suffers from unwanted effects affecting its accuracy. In this Chapter 5, interfering effects from different material and specimen properties are evaluated, providing ground for a better interpretation of experimental results as well as suggestions for a better design of the fiber push-out experiment.

Chapter 6 summarizes the conclusions and perspectives of the project.

CHAPTER 2

Study Uni-directional (UD) Carbon Fiber-reinforced Plastic (CFRP) compression strength in fiber direction using Finite Element Method

2.1. Introduction

This Chapter presents the PhD work on the Research Topic: *Study Fiber-direction Compression Failure of Uni-directional (UD) Composites using Analytical and Numerical methods*.

Composite materials are widely considered as being used under potential due to the complexity and variety of their damage and failure, hence the notorious difficulty of predicting their failure properties. As a result, components using composites (including CFRPs) are usually designed with a large Safety Factor, partially decrease their advantage in weight-saving. Particular attention is paid to the compressive damage properties of composite, where *Fiber-Direction Compressive Strength (σ_{c11}^{o})* is usually 2 times lower than in tensile strength [19]. There are many compression failure modes of composite which depend on properties of component fiber, matrix, and the cohesion of fiber-matrix interface [10]. Composite may fail via. longitudinal splitting, shear crippling or simple compression. Fiber may fail in shear, in kinking or in bending. Ductile matrix fails via. plastic flow while brittle matrix fails via. shear banding.

To address the limitations of the HM-based composites, researchers at AMSL-UTA develop new hybrid composites by mixing the HM and IM reinforcing carbon fibers. A new design, the HS40/MR70/3831 hybrid material, is significantly stiffer, with only a small reduction in axial compression strength comparing to the legacy aerospace IM composites [17]. This promising result motivated the breaking down of the Research Topic into smaller questions/objectives:

- Question 1: Explain the low axial compression strength of HM composites compared to IM composites.
- Question 2: Explain the improvement of axial compression strength of the new hybrid composite designed at AMSL.

- Question 3: Propose an optimal configuration of IM/HM hybrid FRC to maximize axial compression strength.

2.2. Literature reviews

This section reviews the analytical and numerical methods that have been employed to study axial compression failure of FRC. This section also reviews the studies on the hybrid composites and on the kink-band formation, likely the principal axial compression failure mechanism in high-performance carbon FRC.

Analytical methods

Analytical models have been proposed to explain the failure mechanics and attempt to predict composite's σ_{c11}^{o}. By their nature, analytical models can be classified into two groups. The *first group* predicts compressive strength based on *properties of the components* (fiber, matrix, interface etc.). The *second group* predicts compressive strength based on *other macroscopic properties of composite* such as shear modulus or shear strength (Barbero et al. [20]). Models of the *second group* require composite specimens to be manufactured first (and have macroscopic properties measured), hence are of little interest in our project which focuses on composite properties prediction from components' properties.

In the *first group,* Rosen's 2D analytical model [8] might be the first to propose a compressive strength value based on the buckling of fibers in two modes: Extension mode (or Out-of-phase) where:

$$\sigma_c^* = 2V_f \left[\frac{V_f E_m E_f}{3(1-V_f)}\right]^{\frac{1}{2}} \quad (1)$$

and Shear Mode (or In-phase) where:

$$\sigma_c^* = \frac{G_m}{1-V_f} \quad (2)$$

In most applications, compressive strength given in (1) is much higher than (2), and (2) is frequently cited as the Rosen model's compressive strength. Nevertheless, this value is widely recognized as being much higher than the normally measured compressive strength [11], [12]. Later authors proposed various models (Steif et al. [11], Budiansky et al. [21], Gutkin et al. [14]) with added complexity and refinement, including various component parameters such as fiber's Young Modulus, fiber geometry and misalignment, matrix shear strength etc.

Due to the complex failure mechanics and heterogenous nature of the composite materials, it might be complicated for analytical models to capture all these effects. The difficulty increases further with the more complex geometry of hybrid composites. Considering these difficulties and potential limitations, my research efforts focus on numerical modelling.

Numerical methods

Numerical simulation using Finite Element Method (FEM) has been employed to study the fiber-matrix and fiber-interface-matrix systems. A 2D FEM model was developed by Gutkin et al. [14] to validate their analytical model with good correlation on the kink-band formation part of the failure envelope. In addition, Gutkin's FEM model also created the shear-driven compressive fiber failure of the failure envelope which was not described by their kink-band formation analytical model. Naya et al. [15] studied a multiple fiber Representative Volume Element (RVE) with random fiber distribution, matrix and fiber-matrix interface. However, due to high computation costs, their parametric studies were run on a single-fiber RVE. One of the most notable results is the observed composite strength reduction due to weaker fiber-matrix interface, which is confirmed by Herraez et al. [22] and Ghaffari et al. [23] also by analyzing a single-fiber RVE. The use of Periodic Boundary Conditions on the RVE by Naya and Herraez means a realistic non-zero kink-band boundary angle cannot be reproduced.

With the increasing computation power and improved sophistication of numerical models, computer simulation is especially useful in studying and engineering heterogeneous composite material with complex geometry. As part of my project, FEM

numerical models are being developed and calibrated using experimental data from works at AMSL and from literature.

Hybrid composites

Considering the advantages and the setbacks of IM-based and HM-based composites, it might be a natural idea to combine their strengths in a “Hybrid Composite” (from now shortened as “hybrid”), which offers high stress resistance of IM with high rigidity of HM composites. Makeev et al. successfully designed an IM/HM carbon fiber hybrid system having a longitudinal Modulus at 32% higher than reference IM composite, while being only 5% weaker in compression strength [17]. This approach is, however, not straightforward. Indeed, Piggott et al. [9] reported that Carbon-Glass hybridization actually *reduced* Compression Strength compared to either pure Glass or pure Carbon reinforced composite. Other studies [24], [25] confirmed this possibility of (severe) strength reduction in hybrids.

Aveston et al. [26] proposed a simple theoretical model and failure mechanism for hybrid composite in tension. Their model was compared with experimental results on a Carbon-Glass-Epoxy hybrid, showing relative correspondence, differences can be explained by the fact that *not all reinforcing fibers fail at once*.

Piggott et al. [9] studied experimentally the behavior in compression of a range of different hybrids: Glass-Kevlar, Glass-Carbon, Kevlar-Carbon, Carbon-Carbon, with varying ratio of mixing. The most important conclusion is that the “mixture rule” is not valid in most cases for strength i.e., the observed strength deviates positively or negatively from the “linear prediction line”. Particularly, in the case of carbon-glass composite, compression strength is reduced. Yerramalli et al. [24] confirmed this observation. They proposed different theoretical mechanisms of failure for hybrids with different mixture ratios which offered an explanation for their experimental results. These results also confirm the complexity and variety of failure mechanisms of hybrid – which is unsurprising, given that even non-hybrid composites exhibit different mechanisms according to their specific configuration (fiber and matrix properties, fiber volume fraction, etc.).

There are few numerical studies on hybrid composites. Koppisetty et al. [16] studied the effect of fiber distribution in Glass/Carbon hybrid using FEM on a RVE containing different distributions of fibers. The studied configurations appear relatively simple and idealistic. Nevertheless, the simulations confirmed the dependence of Compressive Strength on fibers' placement and suggested positive effects of glass/carbon hybridization if fibers placement could be controlled at tow-level.

Kink-band formation as a mode of longitudinal compressive failure

Kink-band formation is widely agreed as the principal mode of longitudinal compressive failure in UD composite [10], [27]. Therefore, any credible FE model of fiber-direction compressive composite failure should be able to reproduce kink-bands similar to the experiments. Thus, it is helpful to review the literature on the kink-band properties including their formation mechanics in the UD composites.

Kink-band is typically created due to the structural buckling of oriented material. As a result, kink-band can be formed at both meso/ply-scale [28] and micro/fiber-scale [13]. At microscale, kink-band is supposed to be formed through local fiber buckling, fracture and rotation. Kink-bands frequently appear in conjunction and might have causality relation with other failure modes such as composite shear failure and shear splitting, in which shear splitting can initiate kink-band formation and vice versa [29], [30].

Wang et al. [30] studied kink-band formation in notched UD CFRP under four-point bending, and described the two main types of kink-band geometry: 1-Shear type and 2-V-Shaped type. Figure 1 illustrates the kink-bands of these two types. Meanwhile, several experimental studies show the more frequent presence of Shear-type kink-bands [29], [31], [32]. As a result, my project concentrates on the Shear-type kink-band.

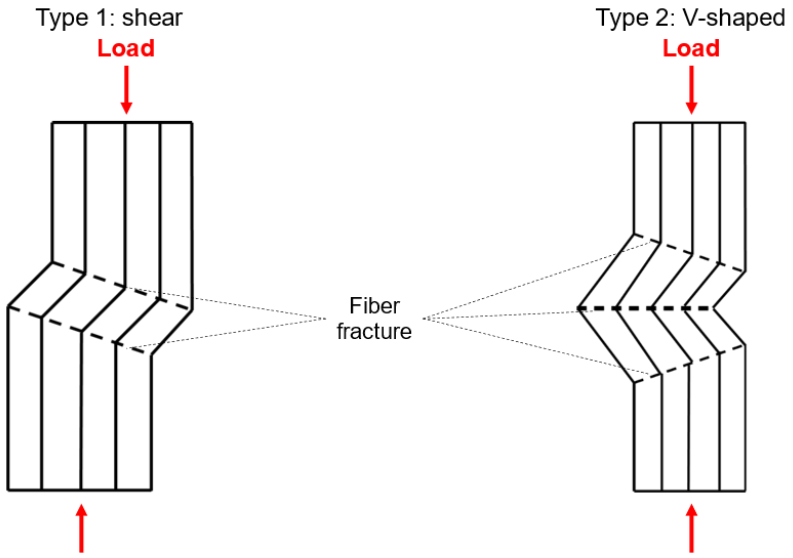

Figure 1. Illustration of two main types of kink-band geometry: shear and V-shaped.

Figure 2 provides an illustration of the shear-type kink-band with its important geometric features including:

- Kink-band width along fiber direction: w
- Kink-band fiber rotation angle, relative to original fiber direction: α
- Kink-band inclining angle, relative to original transversal plane: β
- Kink-band orientation: out-of-plane, in-plane

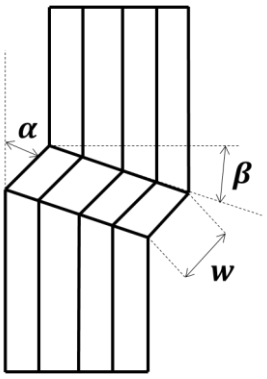

- Figure 2. Label system of kink-band geometric properties: width w; fiber rotation α; inclining angle β.

For shear-type kink-band on the T800 CFRP, Wang et al. [30] reported the following properties: kink-band width $w = 15 - 30\,\mu m$; kink-band inclination $\beta = 20^o -$

35^o; fiber rotation angle $\alpha = 45^o - 60^o$ under load and $\alpha = 20^o - 50^o$ when unloaded. It seems obvious that kink-band width and inclination are crack properties so they do not change after unloading, while fiber rotation would be reduced when the applied load is relaxed. Hahn et al. [10] summarized kink-band geometry of several FRC types. For carbon FRC, fiber breaks are usually observed at kink-band boundaries. Fiber kinking without fracture is typical for the less brittle Kevlar FRC. Glass FRC even shows extreme fiber bending without fiber fracture. Hahn et al. also reported the approximate relation between the angles: $\alpha \approx 2\beta$. This relation is supported by some analytical models on the kink-band formation. Daniel et al. [29] studied kink-band features on the thick specimen (72 plies, $9.1mm$ thick) of the CFRP IM6G/3501-6. Daniel et al. reported some important behaviors of the initiation and development of the kink-bands:

- First failure mechanism: failure seems to be initiated by matrix shear yielding/failure precipitated by local fiber misalignment, leading to kink-band formation.
- Fiber buckling and fracture: follows matrix shear yielding/failure. Fiber fracture increases shear stress in its vicinity, favoring matrix yielding and leads to further propagation of fiber buckling and fracture. This cascade of events eventually leads to the formation of kink-bands.
- Kink orientation angle: starts very small, observed to be $\alpha_0 = 5.3^o$, but increases with higher compressive stress. The angle α can increase up to a maximum value of $\alpha_{max} = 2\beta$.
- Once the maximum rotation angle α_{max} is reached, further stress increase leads to kink-band multiplication and broadening. In parallel, kink-band multiplication and broadening leads to decreased fiber rotation angle α, suggesting a relation in which the local stress is partially relaxed by the kink-band propagation.
- Multiple kink-bands can originate from one source region.

- There is no clear relation between kink angles α and β. However, the maximum value of local α is reported to be: $\alpha_{max} = 2\beta$, which is similar to the observation of Hahn et al. [10]. α and β are frequently but not always equal.
- Fiber rotation angle α ranges from very small to up to 60^o.
- Kink inclination β seems to depend on both local and global states of stress. Its value varies between $20^o - 30^o$.
- Kink-band width w varies between 4 to 20 fiber diameters. For IM6 carbon fiber, these equal to $20 - 100\ \mu m$.
- Within the same kink band, both width w, kink angles α and β, and kink-band orientation (in-plane, out-of-plane) could vary along the kink band.
- Insignificant effect of specimen thickness on compressive strength. However, kink-band geometry is more complex in thicker specimens.

The most interesting result from the study of Daniel et al. [29] is probably the observation that, for CFRP with high performance fiber such as the IM6G/3501-6, *kink-band formation occurs before fiber fracture* at kink-band boundaries. This strongly supports the hypothesis that *fiber buckling leading to kink-band formation is the principal initiator and mode of compressive failure* in high-performance CFRP.

2.3. Analysis of composite fiber-direction compressive strength using FEM

The FE models are developed in Abaqus using integrated Python Scripting feature, allowing the flexibility and rapidity of modifying and parameterizing the FE models, saving time both in building the models and processing the results.

By definition, the RVE is the smallest volume over which an estimation of a certain property of the material as a whole can be extracted with a given precision. For elastic properties, RVE size can be small (an RVE containing five fiber is sufficient, see Appendix A), while damage properties study requires RVE of much larger size. RVE numerical studies by Gonzalez et al. [33] suggested that a RVE containing 30 fibers (with 50% fiber volume fraction, the cross-section size is about 13.7 times fiber radius)

is sufficient to capture damage behaviors. Naya et al. [15] utilized an RVE containing 50 fibers with 60% fiber volume fraction (the cross-section size is therefore 16 times fiber radius) for compressive strength analysis. Due to high computational cost, Naya utilized a RVE containing 1 fiber for parametric studies, reasoning that 1-fiber RVE produces the same compressive strength as the 50-fiber RVE. However, this equivalence was shown on only one single configuration (fiber distribution, fiber misalignment), and has not been verified on other configurations.

In this project, Periodic Boundary Condition (PBC) is applied on the RVE using the algorithm and technique of “dummy nodes” as explained by Gomez et al. [34]. The current algorithm applies PBC to any 3D rectangular cuboid meshed volume where the meshes on opposite surfaces/edges are periodic. Details of the PBC and the RVE size convergence study are presented in Appendix A.

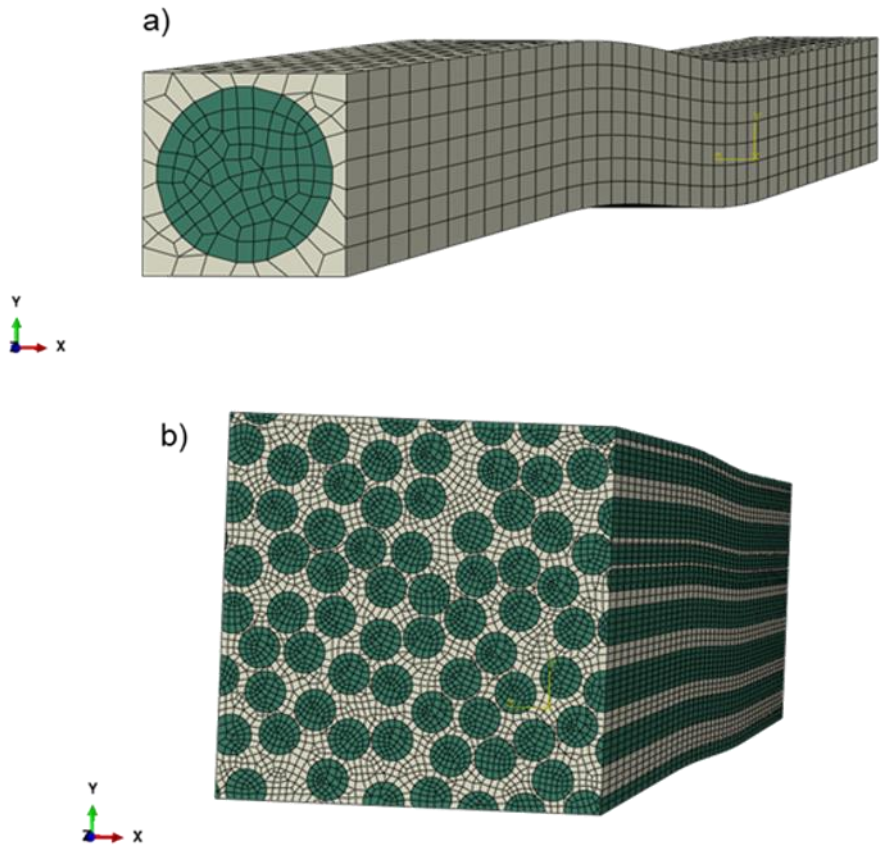

Figure 3. Example of FE RVE with PBC, fiber waviness for longitudinal compression test: a) 1-fiber RVE; b) 65-fiber RVE

Figure 3 presents the RVE for compression strength study. To create FE model geometry, circular cross-sections of fibers are randomly generated as circles on a 2D square surface, then the 3D model is created by extruding this 2D surface along the fiber direction. For each square area, the number of fibers is appropriately calculated so that the RVE has the same Fiber volume fraction $V_f = 0.591$ as the reference material. PBC is applied on the model with some modifications accounting for hypotheses of a fiber-direction compression test. Fiber misalignment is introduced by applying sinusoidal coordinate displacements to RVE's nodes. Fiber's material orientation is defined following the finite elements' inherent geometry, hence the local fiber material orientation always follows the fiber geometrical orientation, including their misalignment/waviness. Fiber and Matrix are modelled by a mixture of C3D6 and C3D8-types 3D elements.

The FE RVE models the fibers, the matrix and the fiber-matrix interface. Fiber material model is homogenous, orthotropic elastic. The Matrix material model is homogenous, isotropic, with non-linear behavior modelled using the Concrete Damaged Plasticity available in Abaqus. Interface is modeled with Surface-to-Surface cohesive, damageable contact. The RVE presented in this study utilizes the IM7/8552 CFRP composite as reference. Component material properties of the IM7/8552 composite are presented in detail in Chapter 3. The current fiber material model does not describe its damage behaviors. However, literature reviews shows that fiber material damage has potentially important role in kink-band formation and propagation as well as geometry. As a result, future improvements to the FE model should include fiber damage behavior.

The composite RVE represents an elastic column prone to compressive buckling. Therefore, the Riks method available in Abaqus is implemented as an efficient strategy to study the RVE structure buckling.

2.4. Effects of some microscale properties on UD composite longitudinal compression strength

In this Section and the Section that follows, “Stress” result refers to the global compression stress, which equals applied Load divided by the RVE cross-section Area orthogonal to fiber direction. “Strain” refers to change of RVE length in the original fiber direction.

Figure 4 presents a preliminary analysis of fiber misalignment effects over RVE compression strength. The model consists of a single fiber (Figure 3.a). Misalignment is varied by changing the amplitude of the sinusoidal waviness. The results indicate that the Peak Load is reduced with increasing misalignment. The configuration with 0.9^o misalignment (similar to the standard deviation of typical experimentally measured fiber misalignment [35], [36]) produced a buckling load/ peak load higher than the experimental results. The tendency indicates that lower fiber misalignment would lead to even higher buckling loads. These results are similar to the numerical results by Naya et al. [15].

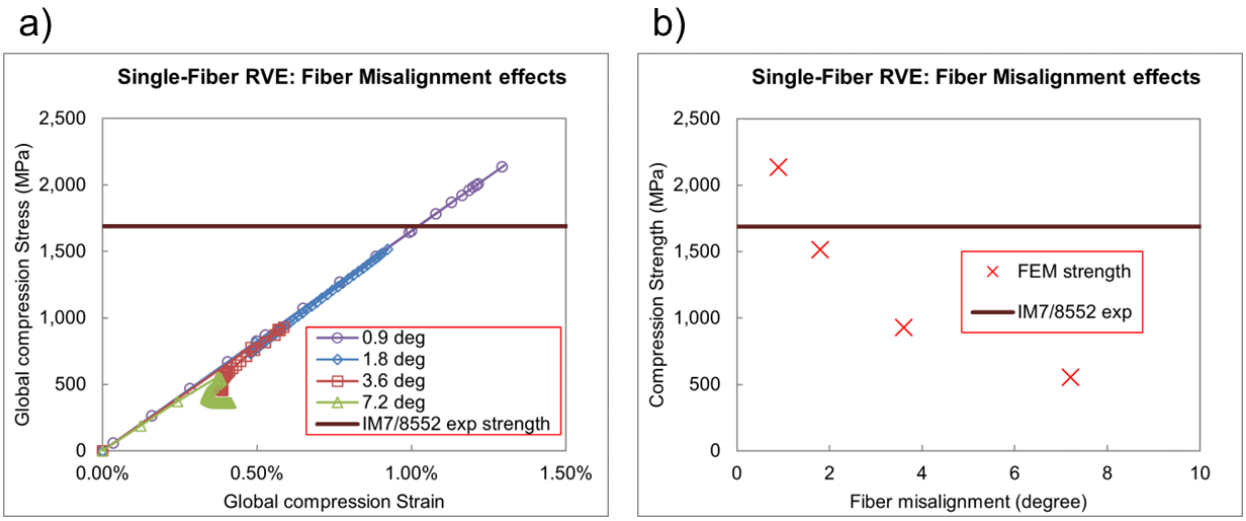

Figure 4. Effects of fiber misalignment on compressive behavior of 1-fiber RVE: a) Stress-Strain curves of different misalignment angles; b) Peak-Load in function of fiber misalignment angle.

Figure 5 presents the FEM results on effects of weak fiber-matrix interface on the RVE buckling stress. FE RVEs with 65 fibers and 1 fiber (depicted in Figure 3) were studied. Fiber misalignment angle is 0.9^o. The simulation of 65-fiber models took approximately 25 hours to finish, while the 1-fiber model took approximately 10 minutes.

Stress-Strain results are compared between the two cases: 1-interfacial damage is deactivated, and 2-the interface is weak and damageable. Interfacial strength is taken from experimental measurement of IFSS on IM7/8552 composite [23]. On the FE RVEs of both sizes, weak and damageable interface leads to lower Compressive Strength, a tendency observed in FEM numerical results on single-fiber RVE by Naya et al. [15], Herraez et al. [22] and Ghaffari et al. [23].

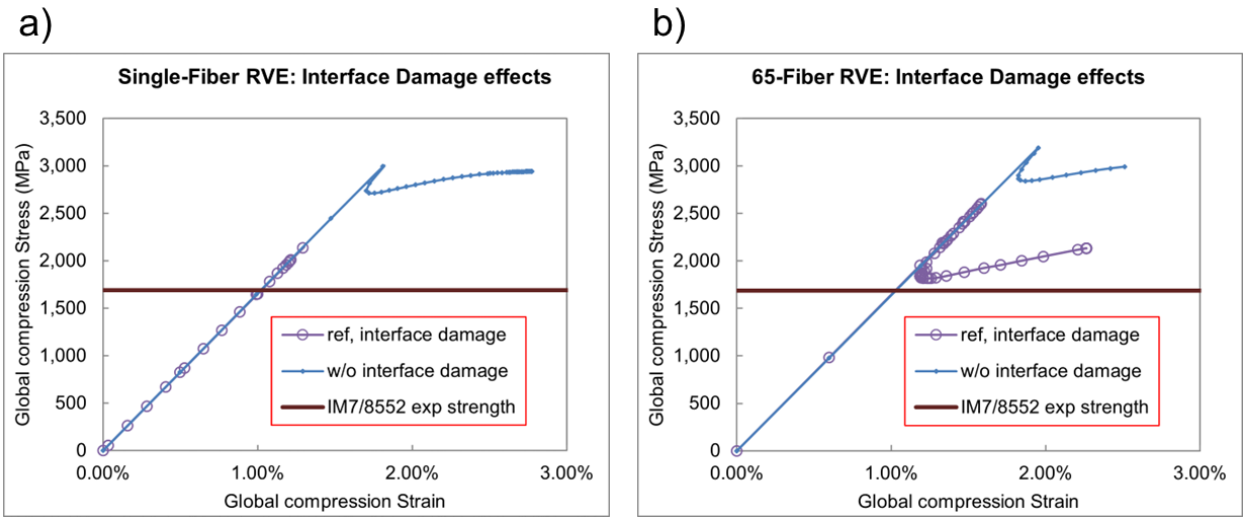

Figure 5. Damageable interface leads to lower compressive strength in fiber-direction. Stress-Strain curves of: a) 1-fiber RVE; b) 65-fiber RVE

Figure 6 compares compression stress-strain curves of the 65-fiber RVE and the 1-fiber RVE (shown in Figure 3), both having the same fiber volume fraction and fiber misalignment (0.9^o). Figure 6.a compares results from models without interface damage, and Figure 6.b compares results from models with interface damage activated. Mesh densities on both RVEs are approximately the same. The initial, linear part of the two curves shows no difference, due to similarities in material compositions and fiber volume fraction. However, in both cases with interface damage and without interface damage, 1-fiber RVE shows a significantly lower peak-load than the 65-fiber RVE: 6% lower in case of no interface damage, and 18% lower in case with interface damage. These results suggest that RVE containing only 1 fiber is insufficient for composite's σ_{c11}^{o} strength analysis.

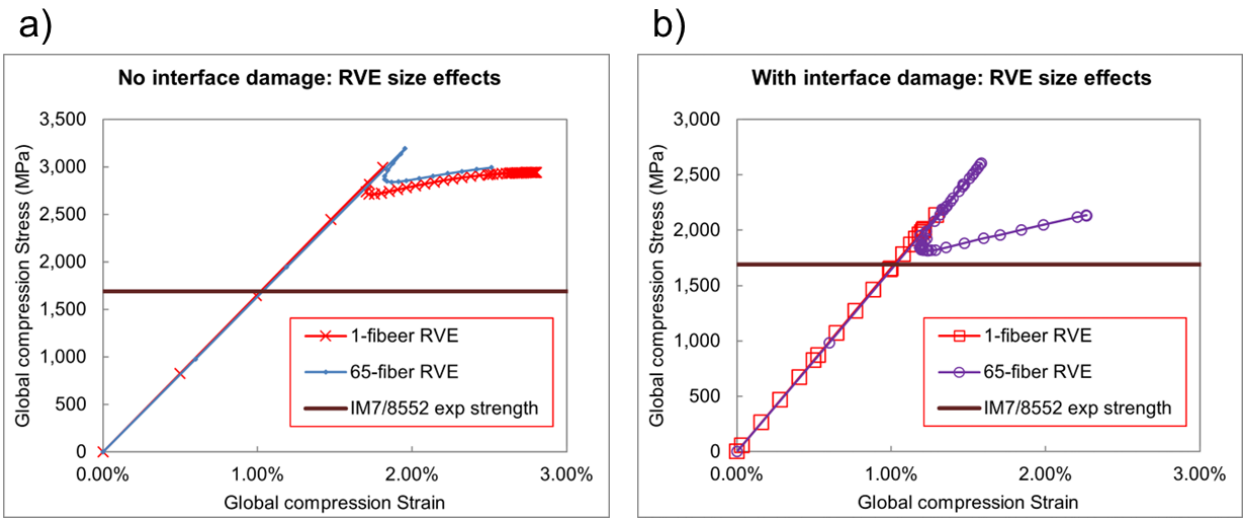

Figure 6. Comparing stress-strain curves of 65-fiber and 1-fiber RVEs: a) Without interface damage; b) With interface damage activated

2.5. Parametric analysis: comparing axial compression strengths of HM and IM composites

Using the 1-fiber RVE at $0.9°$ of misalignment, this Section presents an analysis of axial compression strengths of the MR70/3831 (IM) and the HS40/3831 (HM) carbon/epoxy composites.

Table 1 presents the reference elastic parameters of HS40 and MR70 carbon fibers in the model. The axial modulus values (E_{11}) are provided by the manufacturer. Other properties are assumed equal to the IM7. Table 2 presents the elastic and plastic properties of the 3M 3831 epoxy. Modulus and Tension Strength are provided by the manufacturer. Other properties are estimated based on the 8552 epoxy. For a detailed presentation on the micro-properties of IM7 carbon fiber and 8552 epoxy, please refer to Chapter 3. Table 3 presents the reference IFSS of MR70/3831 and HS40/3831 composites which were obtained experimentally through fiber push-out test [18].

Table 1. Reference mechanical properties of HS40 and MR70 carbon fibers.

	E_{11} (GPa)	E_{22} (GPa)	E_{33} (GPa)	ν_{12}	ν_{13}	ν_{23}	G_{12} (GPa)	G_{13} (GPa)	G_{23} (GPa)
HS40 (HM)	455	15.0	15.0	0.20	0.20	0.07	15.0	15.0	7.03
MR70 (IM)	325	15.0	15.0	0.20	0.20	0.07	15.0	15.0	7.03

Table 2. 3M 3831 reference mechanical properties

Elastic	E (GPa)	ν_m			
	6.16	0.39			
Concrete Damaged Plasticity	Ψ	ϵ	σ_{b0}/σ_{c0}	K_c	μ
	29	0.1	1.29	1	1E-5
Yield Stress	Tensile (MPa)	Compressive (MPa)			
	125	180			
Fracture Energy	Mode I (J/m^2)				
	100				

Table 3. Experimental IFSS of HS40/3831 and MR70/3831 carbon/epoxy composites.

	IFSS (MPa)
HS40/3831	109
MR70/3831	154

The IM and HM carbon fibers show a very apparent difference in fiber axial modulus. In addition, experimental data show a significant difference of IFSS between the two types [18]. As such, sensitivity studies on the effects of these parameters on the composite strength are performed. Using the HS40/3831 as a baseline, Figure 7 presents the effects of fiber axial modulus (Figure 7.a) and of the IFSS (Figure 7.b) on the RVE compression Stress-Strain response. Fiber Modulus visibly affects the initial slope, but has almost negligible effects on the Buckling Stress. On the other hand, IFSS has significant influence on the Peak/Buckling Stress. Figure 7.c presents the effects of IFSS on the RVE compression strength. At lower values of IFSS, the effects on compression strength are very significant. The effects become less significant at higher values of IFSS as stronger interfacial strengths produce the results approaching the case of perfect interface with no damage.

Figure 7.d compares the RVE Stress-Strain responses of the HS40/3831 (HM) and MR70/3831 (IM) composites. A 30%-lower IFSS in HM composite RVE leads to an 8% reduction of compression strength compared to the IM. This reduction is less

significant than experimental observations (from 20% to 30% reduction [18]). The difference might come from the incomplete RVE (in size, fiber distribution representation, material models etc.).

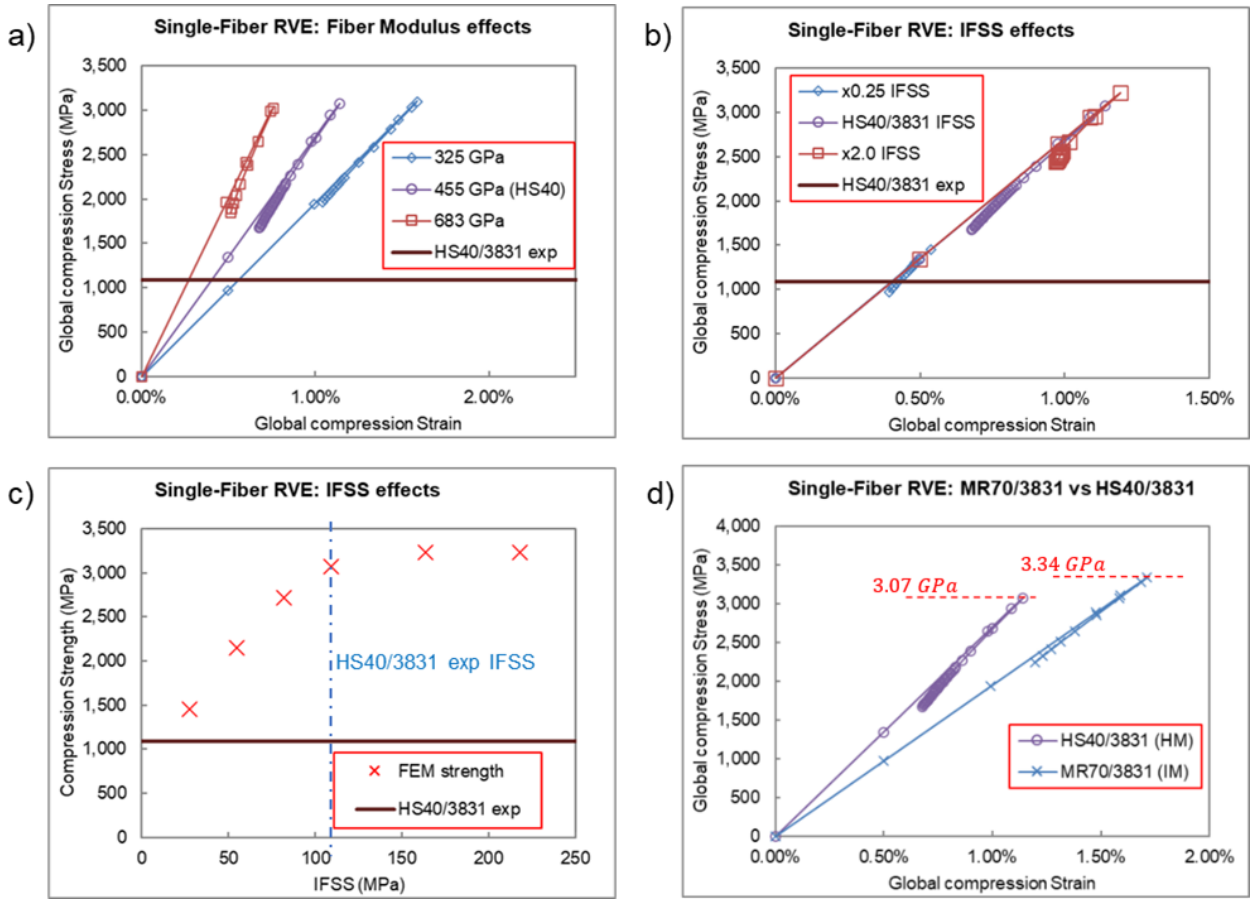

Figure 7. On 1-fiber RVE: a) Fiber Modulus effects on Stress-Strain response; b) IFSS effects on Stress-Strain response; c) IFSS effects on Buckling Stress; d) Stress-Strain responses of HS40/3831 (HM) and MR70/3831 (IM) composites.

These results might offer an explanation to the Question 1 regarding the low axial compression strength of the HM composite. The analyses suggest a strong correlation between the IFSS and the Buckling Stress of the Composites. As micro-buckling is likely the principal mechanism of axial compression failure in high-performance carbon FRCs, *low IFSS is likely the cause of lower axial compression strength in HM composites*.

2.6. Proposals for improvements and future works

Validation of Micromodel: 4-point-bending notched specimen

The microscale RVE has traditionally been implemented with Periodic Boundary Conditions [15], [23], [37], representing a small volume located deep within the specimen of much larger scale. Literature review suggests that for damage analysis purposes, the RVE cross-section should be of at least 50 times the fiber radius [38], [39]. In HS40/3831, this minimum size equals $125\,\mu m$. Meanwhile, UD composite plies have the typical thickness of $400\,\mu m$. The RVE size is therefore of almost the same scale as the ply thickness, making the argument of “small volume located deep inside the specimen” and the application of Periodic Boundary Conditions questionable. As a result, a direct validation of the micromodel is difficult due to the uncertainty in determining appropriate boundary conditions.

To alleviate this difficulty to validate the micromodels due to uncertain boundary conditions, the AMSL/UTA Research Team proposed the experiment of 4-point-bending notched specimen (Figure 8.a). Due to stress concentration at the notch, the location of initial compression failure can be easily predicted (Figure 8.b, 8.c). As a result, with the micromodel being inserted at the notch, compression failure analysis can be conducted on the micromodel with boundary conditions being determined precisely. Thus, this experimental setup potentially offers a strong, direct validation of the micromodel without any assumption required on the boundary conditions. Figure 8.d presents the FE model of the 4-point bending notched specimen with the composite micromodel embedded at the central notch.

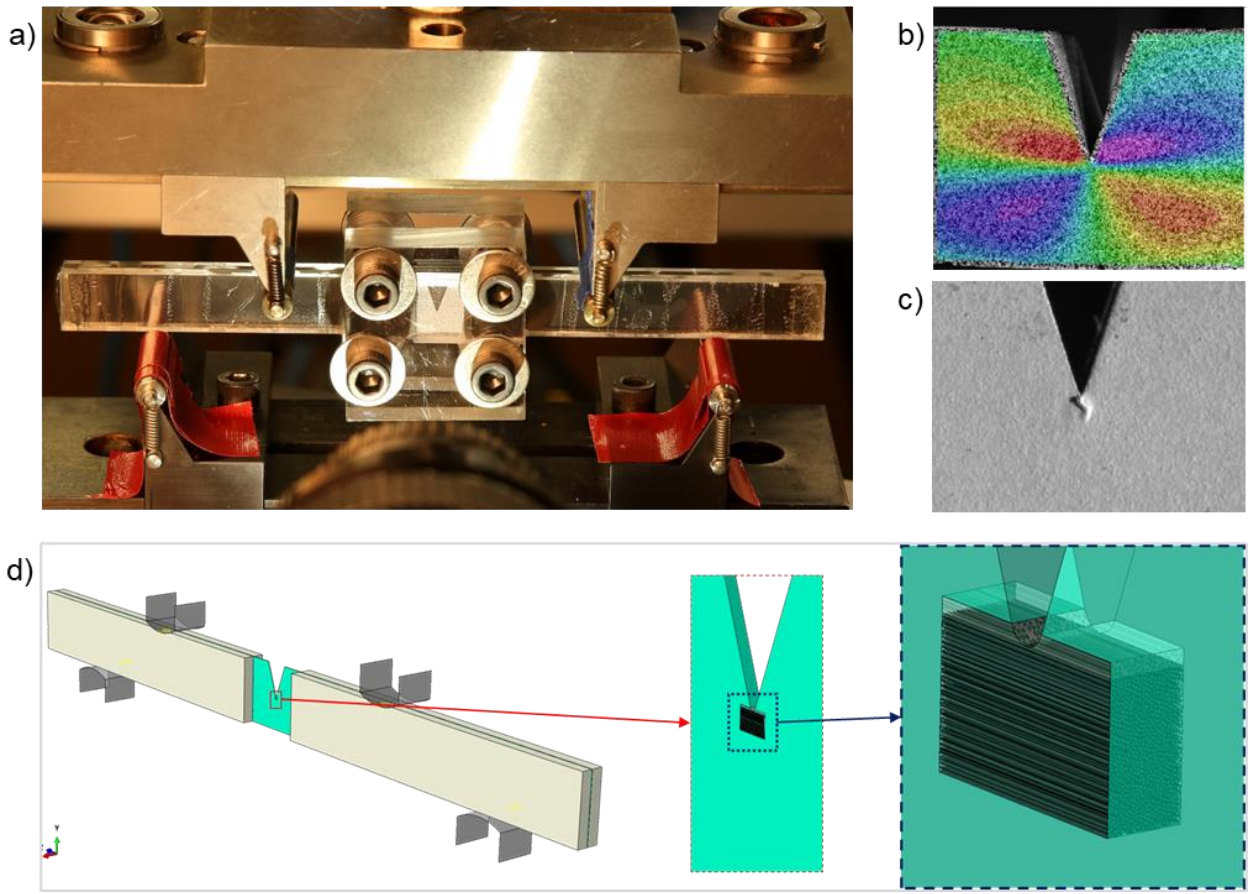

Figure 8. Four-point bending notched specimen: a) Experiment setup; b) DIC image of the notch area, showing ε_{xy}; c) Compression fracture initiation at the notch; d) FE model of the experiment, with micromodel embedded at the notch.

Proposals for future works

Below are some perspectives on numerical simulation model:

- Improve geometry of the RVE: fiber misalignment should be random and follow a configurable distribution. Figure 9 compares the current RVE having uniform fiber misalignment and the nano-CT image of a microscale composite volume where random fiber misalignment is apparent.

- Calibrate the stress concentration field at the notch where the embedded micromodel is located. Figure 10 presents an example of longitudinal stress concentration in this area of interest where a token material volume with homogenized composite properties is embedded (Figure 10.a). The low computational cost of the

homogenous token material volume is useful at the stage of feasibility and calibration study. Figure 10.b presents the global Load-Displacement response registered at the numerical Loading Heads in the 4-point-bending model, showing good correlation up to the point of abrupt failure.

- Develop a simulation strategy to optimize calculation resources. Both the microscale RVE and the 4-point-bending FE model are potentially very expensive in terms of computational cost due to the complex geometry of huge number of fibers in the micromodels.

- Improve Abaqus simulation model: add damage model to fiber material model, refine material and interface properties. Perform mesh and size convergence analyses.

- Validate the numerical micromodel using the 4-point-bending notched specimen setup which offers precise determination of the Boundary Conditions applied on the embedded micromodel.

- Once the micromodel for axial compression strength has been validated, perform parametric studies to determine the impact of different material parameters on composite axial compression strength σ_{c11}^{o}. Identify key parameters with the most significant impact on σ_{c11}^{o}.

- The method of Barbero et al. [20] provides an interpretation on effects of fiber misalignment distribution on composite σ_{c11}^{o} at microscale and at macroscale. This method might offer a prediction of material strength *without the need for a RVE with realistic fiber misalignment distribution*. However, an improved RVE geometry with realistic fiber misalignment distribution, combined with direct micromodel validation using the 4-point-bending notched specimen presented above, is believed to provide a more robust representation of composite failure and would be more useful for the optimization of new hybrid composite designs.

- With the RVE having realistic fiber misalignment representation and the micromodel being validated, these FE micromodels can be applied to the engineering of hybrid composites. Optimize hybrid compressive strength by studying the impact of

different design variables, including the choice of fibers, distribution and placement of two types of fiber, etc.

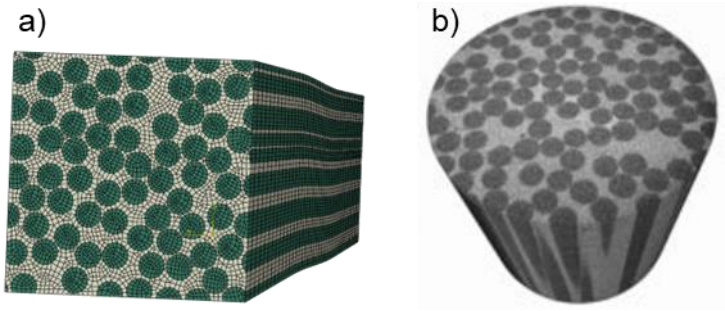

Figure 9. a) Current RVE with uniform fiber misalignment; b) Nano-CT image showing realistic, random fiber misalignment within a small composite material volume [31].

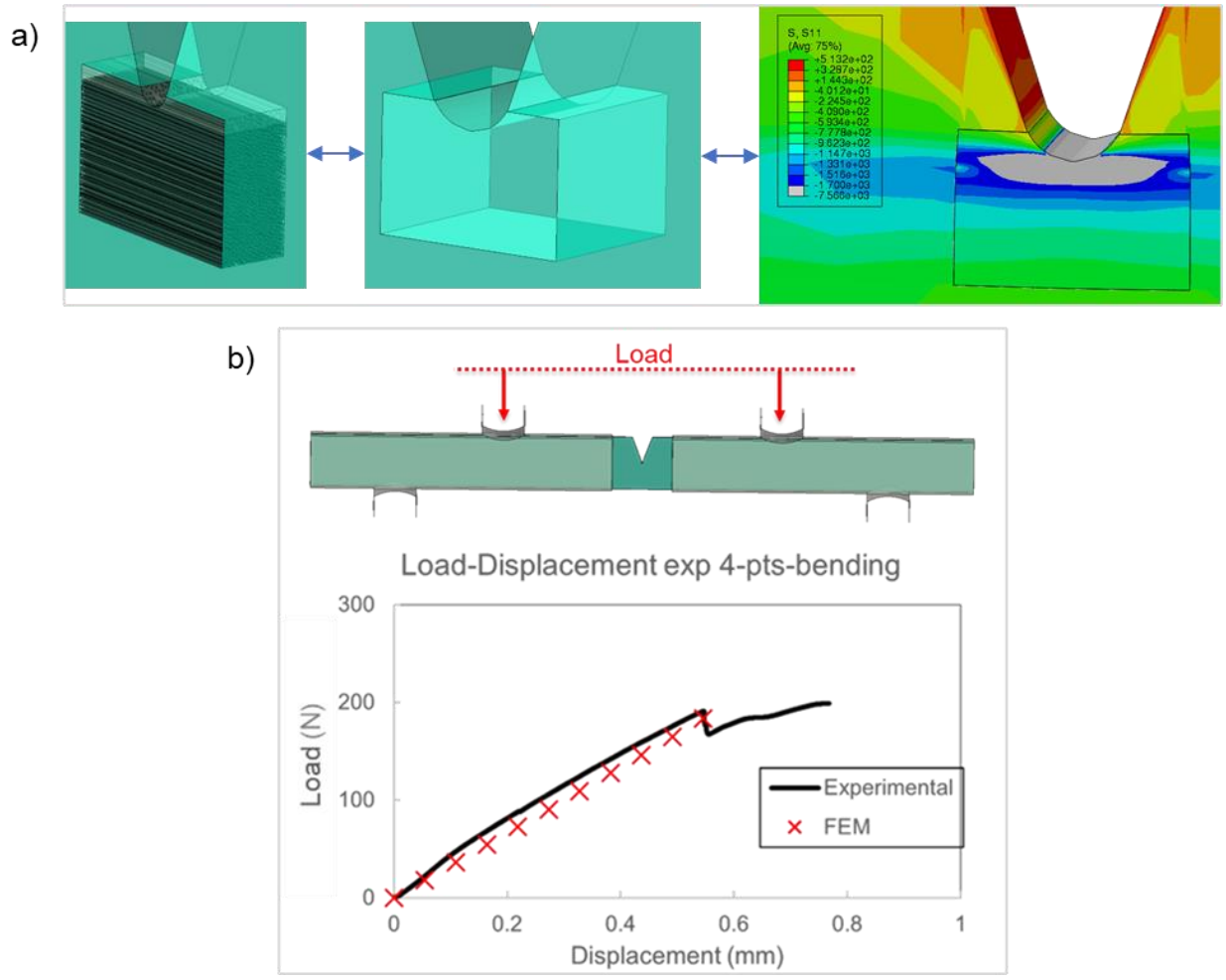

Figure 10. a) Heterogenous embedded micromodel is replaced by homogenous volume with homogenized composite properties for efficient stress concentration calibration analysis; b) Comparing Load-Displacement response at Loading Heads, FEM and experiment.

2.7. Conclusions

A literature review was performed on the analytical and numerical methods for the analysis of UD composite axial compression failure in carbon FRC as well as their applications in hybrid composites that combine different types of reinforcing fibers. The numerical FE modeling is suggested as the preferred methodology for the project thanks to its ability to represent complex material models, complex failure mechanisms, and the complex geometry of the hybrid carbon FRCs at microscale. The literature review also found the kink-band formation to be a principal compression failure mechanism in high-performance CFRP composites. Common geometric features of kink-bands in different types of FRC were reviewed and summarized, which would serve as a helpful reference for the future studies on numerical modeling of kink-band in FRC materials.

An RVE with uniform fiber misalignment was developed and analyzed for instability/buckling failure under longitudinal compression. Parametric analyses identified several microscale properties with significant impact on composite axial compression strength: fiber misalignment and fiber-matrix IFSS. An RVE containing one fiber is likely insufficient to represent axial compression failure in composite.

A study comparing HM and IM carbon FRC compression strength was performed using parametric analysis. Fiber axial modulus has almost negligible effects on composite strength, while IFSS has very pronounced effects. Lower IFSS in HM composites is likely the reason for the lower compression strength compared to IM composites due to the lower resistance to compression instabilities/buckling failure.

The application of Periodic Boundary Conditions on the micromodel RVE was discussed and questioned. Direct validation of the micromodel has long been difficult due to the inability to represent precise, realistic boundary conditions in the microscale numerical model. To alleviate this difficulty, AMSL/UTA Research Team proposed the 4-point bending notched specimen experimental setup. In this experiment, boundary conditions on the micromodel embedded at the notched can be determined precisely. An FE model of the experiment was developed, and preliminary feasibility and calibration analyses were performed.

Future works on the research topic of composite axial compression failure were proposed. Microscale RVE needs improvement to represent realistic, random fiber misalignment. Further development of the 4-point-bending notched specimen FE model is required for the strong validation of the micromodel with realistic boundary conditions. Numerical models need to incorporate improved material models, including fiber damage for realistic kink-band formation. With the improved RVE validated to represent axial compression failure in FRC composite, works could then be done on the optimization of hybrid composites with different types of reinforcing fibers using the numerical micromodel.

CHAPTER 3

CFRP component materials properties at microscale: review and suggestions for future experimental works

3.1. Introduction

The FEM has the advantage of explicitly representing different phases of the heterogenous Fiber-reinforced Composite (FRC) at microscale. However, the understanding of the microscale component properties (fiber, matrix, interface etc.) is incomplete. In addition, measurement methods for some microscale properties cannot be found in the literature. On the other hand, for the specific objective of modelling UD FRC fiber-direction compression strength, preliminary numerical results and literature review suggest some material properties have more significant effects than others. It is therefore unnecessary to measure precisely some properties i.e., a good estimation within an order of magnitude is sufficient.

This Chapter provides an extensive review of FRC components microscale properties, their available measurement methods, the significance of their effects on the UD FRC compression strength whenever possible, and the recommendation if future experimental measurement of that material property should be conducted. The relatively well-studied IM7/8552 carbon/epoxy CFRP is also the reference material for this review.

Color Code for physical parameters review table

Physical properties of each component of the FRC system (fiber, matrix, fiber-matrix interface) are summarized in a review table at the beginning of each corresponding section. Each physical parameter is described by:

1. Value: is this parameter's value available from literature (for IM7/8552 CFRP)?
2. Importance on the study of composite's fiber-direction compressive strength σ_c^{crit}: based on numerical sensitivity studies and literature review.
3. Measurement methods available.

4. Recommendation for experimental work: considering the parameter's availability, impact and importance towards the microscale modelling project at AMSL laboratory.

To visualize the availability and the importance of parameters and corresponding measurement methods, a system of color is applied. Table 4 defines the color code for some scenarios.

Table 4. Color code for material properties summary tables.

Parameter	1-Value	2-Important? Impact?	3-Measurement method	4-Recommendation for experimental works
	Green: determined or estimated	Green: Unimportant	Green: established	
	White: unknown	Red: Important	Orange: Value is estimated or dubious method	
		White: Unknown	White: unknown	

3.2. Fiber microscale properties

Summary

Table 5 summarizes mechanical properties of the IM7 carbon fiber.

Table 5. Mechanical properties of IM7.

Parameter	1-Value	2-Important? Impact?	3-Measurement method	4-Recommendation for experimental works
E_{11}	276 GPa [40]	Unknown, likely important	FEMU; Supplier-provided	FEMU available at AMSL
E_{22}	15.0 GPa	Unknown	FEMU; Ultrasound eigenfrequencies etc.	FEMU available at AMSL
G_{12}	15.0 GPa	Unknown, likely important	FEMU; Torsional Pendulum	FEMU available at AMSL
G_{23}	7.03 GPa	Unknown	FEMU	FEMU available at AMSL
ν_{12}	0.2	Unknown	FEMU	FEMU available at AMSL
ν_{23}	0.072	Unknown	FEMU	FEMU available at AMSL
Longitudinal Compressive Strength	Unknown	Important	Bending Beam; Micro-Compression; etc. Related to ε_{c11}^{o}	Recommended due to high importance

σ_{c11}^{o}				
Longitudinal Compressive Critical Strain ε_{c11}^{o}	Unknown	Important	Bending Beam; Micro-Compression; etc. Related to σ_{c11}^{o}	Recommended due to high importance
Longitudinal Tensile Strength σ_{t11}^{o}	5516 MPa [40]	Unknown	Supplier-provided; Tension test	–

Experimental measurement methods

Longitudinal Modulus E_{11} and Longitudinal Tensile Strength σ_{t11}^{o}

Experiments determining carbon fiber microscale properties are difficult due to the small scale involved. The longitudinal tension properties E_{11} and σ_{t11}^{o} are the exceptions thanks to the fiber physical length that allows easy tension test setup. In addition, these properties are typically provided by the fiber manufacturers.

It is important to note that CFRP composite's longitudinal modulus in compression is different from the longitudinal modulus in tension. The compression modulus is typically equal to 90% the tension modulus [40]–[42]. By rule of mixture, we can infer the relation between carbon fiber longitudinal modulus in compression and in tension:

$$\frac{E_c^{fiber}}{E_t^{fiber}} \approx \frac{E_c^{composite}}{E_t^{composite}} \approx 90\%$$

Transversal Modulus E_{22}

The Raman spectroscopy method was applied by Miyagawa et al. [43] to measure E_{22} and compare with results from other methods: Dynamic Mechanical Analysis, Berkovich Nano-indentation and FEM analysis. They found significant difference amongst the values obtained by different methods. Amongst these methods, Gross et al. [44] demonstrated the weaknesses of the Nano-indentation technique on anisotropic materials. Mounier et al. [45] proposed a method to measure E_{22} using laser resonant ultrasound spectroscopy and FEMU analysis.

Amongst the E_{22} measurement methods, the FEMU for inverse determination of fibers' microscale properties might be the most efficient. Measurement of composite macroscale mechanical properties and implementation of FEMU are typically inexpensive and comparatively easier than other proposed methods.

Longitudinal Shear Modulus G_{12}

Deteresa et al. [46] described the Torsional Pendulum experimental method for measuring a single Fiber's Shear Modulus and Shear Strength. Based on a radial distribution of shear strain over the fiber cross-section, from maximum at the surface to zero at the core, Deteresa suggested the formula to calculate Shear Modulus G_{23}:

$$G = \frac{8\pi LI}{r^4\tau^2}$$

With fiber length L, fiber radius r, disk angular moment of inertia I, system oscillation period τ. In 1999, Tsai and Daniel [47] proposed a similar system, with a more sophisticated analytical model which also considers pendulum's damping, but their experiments showed the damping effect can be neglected, hence giving the same formula as Deteresa.

The Shear Modulus G_{12} can also be measured using the FEMU technique.

Transversal Shear Modulus G_{23}, longitudinal Poisson ratio ν_{12}, transversal Poisson ratio ν_{23}

Apart of the FEMU technique for inverse characterization of properties, my literature review found no experimental measurement methods for G_{23}, ν_{12} and ν_{23}.

For an ideal transversely isotropic material, transversal shear modulus G_{23} can be related to transversal Poisson ratio ν_{23} and transversal tension modulus E_{22} via the equation:

$$G_{23} = \frac{E_{22}}{2(1+\nu_{23})} \quad (3)$$

However, Gusev et al. [48] demonstrated the high error of the equation (3) in application to UD composites. The microstructure of carbon fibers also shows transversal anisotropy [49]. Therefore, the three elastic parameters G_{23}, E_{22} and ν_{23} are considered independent in my studies for both the macroscale composites and microscale carbon fibers.

Longitudinal Compression Strength σ_{c11}^{o} and Critical Strain ε_{c11}^{o}

In UD CFRP composites, literature review and preliminary FEM analysis suggest the high importance of carbon fiber longitudinal compression strength σ_{c11}^{o} on both the compression peak load and the post-failure behaviors including kink-band formation. Since carbon fiber exhibits linear behavior prior to its brittle fracture, it can be assumed that σ_{c11}^{o} and ε_{c11}^{o} are linearly correlated, and thus the determination of the two parameters is equivalent:

$$\sigma_{c11}^{o} = E_{11} \times \varepsilon_{c11}^{o}$$

Several methods exist in the literature for measurement of σ_{c11}^{o} (and/or ε_{c11}^{o}). The Elastica Loop method was first developed by Sinclair et al. [50] to measure σ_{c11}^{o} of glass fiber. Furuyama et al. [51] utilized the method to study carbon fibers. The method has the advantage of a relatively simple and inexpensive setup. However, the precise moment of fiber damage initiation is hard to determine, complicating interpretation of results. Deteresa et al. [46] proposed the Bending Beam method. In the setup, the microfiber is bonded on the upper surface of an elastic beam with rectangular cross-section. The bonded microfiber follows the beam's upper surface strain while the beam is bent under either cantilever or three-point bending setup. Using beam theory, bonded fiber compression strain can be demonstrated to have a linear distribution along beam length. By observing the extent of fiber damage, fiber critical compression strain ε_{c11}^{o} can be deduced. This method allows complete prevention of Euler buckling in tested fiber which is the main difficulty in σ_{c11}^{o} measurement. The Micro-Compression method allows direct measurement σ_{c11}^{o} by pushing a free-standing part of a microfiber in the

longitudinal direction. The free-standing fiber part is short to prevent Euler buckling. The microfiber itself is typically held in place by some kind of fixation (glue, polystyrene etc.). Oya et al. [52], Shioya et al. [53], Ueda et al. [54], Leal et al. [55] proposed different setups and sample preparation techniques of the Micro-Compression method. The method requires careful monitoring of fiber damage to avoid possible unwanted effects (matrix damage, fiber-matrix interface damage etc.). In fact, deduced fiber critical compressive strain ε_{c11}^{o} from micro-compression results from the literature [52] is *lower than* critical compressive strain of the corresponding composite (view Table A6), suggesting an unrealistic situation where the reinforcing fibers failed but the composite is still intact. This comparison suggests that these fiber compressive strength results might be underestimated due to multiple unwanted effects affecting Micro-Compression measurements. Another disadvantage of the method is the time-consuming preparation of samples, which was partially alleviated by the sample preparation technique of Leal et al. [55]. In the Recoil Test method [56], the fiber is put under tensile loading with two ends fixed on a frame. When the fiber is cut (typically using laser), the elastic recoil fractures the fiber in compression. This method's greatest advantage is its simplicity. However, the interpretation of the result relating compression strength to initial tension stress might be difficult. Newell et al. [57] provides an analytical expression of axial stress history in microfiber which suggests strong dependence of axial stress on various assumptions on boundary condition (BC) as well as uncertainties in measures. The Embedded In Resin method was proposed by Hawthorne et al. [58], where a rectangular cuboid of transparent elastic material contains one single fiber. Fiber is monitored for damage while compression strain parallel to the fiber is applied on the cuboid specimen. The method provides a straightforward test procedure and result interpretation is simple. However, sample preparation in this method is extremely laborious, with the author having to discard many specimens due to fiber orientation issue.

Due to the importance of reinforcing fibers σ_{c11}^{o} on the modelling of composite strength, it is advised that σ_{c11}^{o} measurement is performed on interested fiber. The Bending Beam technique by Deteresa et al. [46] is proposed as the preferred method thanks to its relatively simple and inexpensive experimental setup, as well as the

robustness and the simplicity of result interpretation. In addition, this method was demonstrated on carbon fibers [59].

3.3. Matrix microscale properties

Summary

Table 6 summarizes mechanical properties of the 8552 epoxy resin. The Concrete Damaged Plasticity (CDP) model available in Abaqus is commonly used to describe non-linear behavior of the brittle epoxies [60], [61]. Table 7 summarizes the properties/parameters for the CDP modelling of the 8552 epoxy.

Table 6. Mechanical properties of the 8552 epoxy.

Parameter	1-Value	2-Important? Impact?	3-Measurement method	4-Recommendation for experimental works
Modulus E	$4670\ MPa$ [62]	Yes	Tensile Test; Supplier-provided [62]	
Poisson ratio ν	0.35 [60]	Unknown	Typical of Epoxy. Ultrasonic Velocity Measure [63]; Fluid Compressibility [64]	
Compressive Yield Stress σ_c^y	$174\ MPa$ [60]	Unknown, likely important	Nano-indentation [65]	Equipment and FEM analysis available at UTA
Tensile Yield Stress σ_t^y	$121\ MPa$ [62]	Yes	Provided by Supplier [62]; Potentially different at microscale [66]	Recommended, using microfiber tensile test [66]
Fracture toughness K_{IC}	$1.62\ MPa\sqrt{m}$ [62]	Not known yet	Provided by Supplier [62]	
Energy release rate G_{1C}	$679.5\ N/m$ [62]	Not known yet	Provided by Supplier [62]	
Fracture energy G_f	$100\ N/m$ [65]	Yes	Provided by Supplier [65]; Or estimated based on G_{1c}	Potentially important

Table 7. Concrete Damaged Plasticity model parameters for the 8552 epoxy.

Parameter	1-Value	2-Important? Impact?	3-Measurement method	4-Recommendation for experimental works
Dilation Angle	29^o [65]	Unknown	Assumed equal Friction Angle (associated flow assumed [65]); Triaxial Test [67]; Parametric	Significant effects on nano-indentation Load-Displacement

			study [68]	curve.
Eccentricity	0.1	Unknown	Typical value for concrete [69]; Triaxial Test [67]; Parametric study [68]	
$fb0/fc0$	1.29	Unknown	Calculated from Internal Friction Angle – obtained from nano-indentation [65]	
K_c	1.0	Unknown	Assumed associated flow [65]; Parametric study [68]	
Viscosity Parameter	0.00001	Numerical value for stabilization	Recommended small or zero [70]	

Experimental measurement methods

In the topics studied during my PhD Project (the Composite Compressive Strength, Residual Microstress and IFSS Measurement using Push-Out method), the following matrix properties were identified as important and have significant impact:

- Modulus E: significant effects on microscale residual stress.
- Tension Yield σ_t^y: significant effects on microscale residual stress and IFSS measurement using Push-Out method.
- Tension Yield at microscale σ_t^y: various authors [66], [71]–[73] studied epoxy tensile behavior at microscale using tensile test on epoxy microfiber samples. They demonstrated very significant size effects: microscale epoxy is ductile while macroscale epoxy is brittle; ultimate failure strain and stress of microscale epoxy is much higher than macroscale epoxy. This suggests the importance of determining microscale epoxy matrix σ_t^y in modelling composite at microscale.
- Compression Yield σ_c^y: sensitivity study was not conducted on this parameter, but matrix compression yield is likely important due to its role in keeping reinforcing fibers orientation under compression load.

Matrix Modulus E

Epoxy Modulus can be obtained using tension test. Results from literature [73] and preliminary results at AMSL, UTA suggest that at small, elastic strain, the epoxy Modulus at microscale (microfiber testing) and macroscale (dog-bone specimen testing) are similar.

Tension Yield σ_t^y and size effects

Different authors [66], [71]–[73] have consistently demonstrated the different behaviors of epoxy at micro- and macro-scales. The most common measurement method of microscale σ_y^t is microfiber specimen tension testing. Different methods exist for stress-strain result analysis, including direct fixture load-displacement readings [72], [73] and in-situ Scanning Electron Microscope (SEM) observation [66].

The epoxy microfiber tension testing method is being investigated at AMSL, UTA.

Compression Yield σ_c^y

Epoxy microscale behaviors in compression can be characterized using nano-indentation test. For example, the Berkovich indentation technique was successfully applied by Sanchez-Carmago et al. [74] to extract elasto-plastic behavior of the 316 L austenitic stainless steel. Unlike steel however, thermoset epoxy exhibits different properties in tension and in compression, at least at macroscale. Naya et al. applied the technique to extract compression properties of the Hexcel 8552 epoxy [65]. A potential advantage of the nano-indentation technique is the ability to realize in-situ measurement of the composite epoxy matrix at easily selected positions.

To investigate the capabilities of the nano-indentation technique to measure matrix microscale properties, Berkovich-indentation experiments were realized at UTA on the 8552 epoxy matrix, and a FEM model for result analysis were developed. Details on this study are presented later in Section 3.5.

3.4. Fiber-matrix interface properties

Summary

Table 8 summarizes properties of the reference composite IM7/8552 fiber/matrix interface.

Table 8. Mechanical properties of the IM7/8552 fiber/matrix interface.

Parameter	1-Value	2-Important? Impact?	3-Measurement method	4-Recommendation for experimental works
Interfacial Normal Strength IFNS	$64.0MPa$	No	Estimated 2/3 IFSS [75]; Single Fiber Specimen in Tension with strain [76], [77] or debonding [78] measure	No
Interfacial Shear Strength, longitudinal IFSS	$95.8MPa$ [23]	Yes	Fiber Push-Out [23]	Equipment for Push-Out experiment available at UTA
Interfacial Shear Strength, transversal IFSS	$95.8MPa$	No	Assumed equal IFSS in longitudinal; Single Fiber Specimen in Tension with strain [76], [77] or debonding [78] measure	No
Normal Fracture Energy G_I^c	$2\ N/m$ [75], [79], [80]	No	Assumed similar to Glass/Epoxy interface. Transverse single fiber test for interfacial debonding [80]	No
Shear Fracture Energy, transversal G_{III}^c	$50\ N/m$	No	Estimated with $\delta_s^c = 1\mu m$ [75] Transverse single fiber test for interfacial debonding [80]	No
Shear Fracture Energy, longitudinal G_{II}^c	$50\ N/m$	Yes	assumed equals G_{II}^c [75] Measurement Method Unavailable	Measurement method unavailable
Benzeggagh-Kenane (BK) exponent η^{BK}	1.45 [75], [81]	Unknown	Assumed similar to ply-level parameter [75] Mixed-Mode Fracture Test Unavailable at Fiber scale	
Interfacial Friction μ	0.4 [60]	YES (kink-band formation)	Fiber direction: Measurement method under development Transversal direction: Mixed-Mode transversal Load [60]	Under development. Residual stress combined with friction stress measurements.
Viscosity for Damage stabilization η	0.0005	Numerical value	Numerical parameter for simulation stabilization, should be near-zero	

Experimental measurement methods

First of all, it is important to note that the term “interface” between fiber and matrix in composite is not clearly defined. Cech et al. [82] supported the assessment that the “interphase” between glass fiber and polyester matrix has non-zero thickness – it is instead a 3D region extending into both sides of the “interface” where the local matrix and fiber properties are modified and discernable from bulk properties.

Meanwhile, SEM images of Fiber Push-Out experiment aftermath by Ghaffari et al. [31] show a “clean” fiber surface which was previously separated from matrix during the Push-Out test. This suggests the simplification of “infinitesimally small interface thickness” is acceptable for the purpose of studying fiber/matrix composite system at the fiber diameter scale.

On the other hand, there exists the situation where the fiber (or the matrix) surface post-test is not smooth with pieces of matrix still attached to the fiber surface, such as the Fiber Push-Out test results by Medina M et al.’s 2015 [83]. This phenomenon might occur due to the high Interfacial Shear Strength compared to the matrix material strength. Precise interpretation of interface properties and its nature in this case might be complicated.

Preliminary FEM analysis on the fiber-direction buckling stress of the UD composite (Section 2.3) suggests a very significant effect of the fiber-matrix IFSS (longitudinal, fiber-direction) on the composite longitudinal compression strength. This strong effect was also confirmed by other authors [15], [22], [23]. It was therefore concluded that the precise determination of the IFSS is essential for the accurate modeling of the UD composite compression buckling.

The fiber-matrix IFSS can be characterized by the Push-Out or the Push-In method [83], each method having its own advantages and disadvantages. The Push-Out method is considered more complicated and more time-consuming due to the need of polishing the thin membrane specimen, but allows comparatively simpler and more robust result interpretation. In addition to the traditional membrane polishing technique,

Ghaffari et al. utilized a new sample preparation technique where a “cave” is carved into a block of material [61] using femtosecond laser. The material above the cave becomes the “membrane” for the fiber Push-Out test. The new technique allows much faster production of specimens at much higher volume. Considering the relative robustness and the ease of sample preparation thanks to the new technique, the Fiber Push-Out test is the preferred method for the IFSS evaluation. My PhD works on the evaluation of IFSS using Fiber Push-Out and FEM analysis are presented in Chapter 5.

FEM analysis suggests a very significant effect of interfacial shear fracture energy, longitudinal G_{II}^{c} on the accuracy of the IFSS measurement using Fiber Push-Out method. However, my literature study did not find any conclusive method for the measurement of this parameter. The reference value for G_{III}^{c} is an estimation made by the assumption that $G_{II}^{c} = G_{III}^{c}$, similar to the approach taken by Herraez et al. [75]. In turn, G_{III}^{c} was not measured for carbon-epoxy interface and was taken to be similar to the glass-epoxy interface [75], [80]. Because of importance of G_{II}^{c}, of the dubious estimations for the current value and the lack of experimental method to determine this parameter, G_{II}^{c} is often the subject of many parametric studies in my PhD project.

FEM analysis of the Fiber Push-Out test in the presence of residual stress shows the very significant effect of the interfacial friction μ on test results. However, the effects of the matrix residual stress (squeezing the fiber) and interface friction on the measured Load are coupled, making it difficult to conclusively determine μ without knowing the residual stress beforehand. Works are being performed on the characterization of matrix residual stress, after which interfacial μ can be decoupled and deduced.

Regarding other interface properties: normal strength IFNS, normal fracture energy G_{I}^{c}, transversal shear strength IFSS, transversal shear fracture energy G_{III}^{2}, FEM analysis suggested the weak to negligible effects of these parameters on both the composite fiber-direction compression strength and on the IFSS measurement using Fiber Push-Out method. Therefore, it might be unnecessary to obtain precise values for these parameters, and a reasonable estimation is sufficient for the current purposes.

3.5. PhD works on the microscale material characterization

PhD work has been done on the characterization of microscale material properties. Extensive work has been done on the two topics: 1- Microscale residual stress in composite and 2- Evaluation of IFSS measurement using Fiber Push-Out method and effects from different factors including micro-residual stress. Therefore, each of these topics is covered in their own respective Chapter 4 and Chapter 5.

This Section presents other works on microscale material characterization at different stages of completeness:

3- The FEMU method for inverse characterization of fiber elastic material. The method implements FEM analysis combined with the Newton-Raphson algorithm. This method is relatively simple but extremely helpful in providing fiber elastic properties, some of which have no known experimental measurement method available.

4- The nano-indentation to characterize microscale compression properties of the matrix. Preliminary analysis demonstrated the feasibility of the method and identified some microscale matrix properties that can be studied with this method. This technique enables the in-situ characterization of matrix at precisely selected locations, which is potentially useful since material properties at microscale might have significant spatial variations, and might differ from bulk material properties at macroscale.

5- The Bending Beam to measure fiber compression strength σ_{c11}. Literature review and analytical analysis have been done to demonstrate the feasibility of the technique with results interpretation, as well as provide important recommendations regarding engineering requirements for the experiment. The characterization of micro-fiber compression failure is strongly recommended, as literature review on the kink-bands clearly show fiber breakage at the kink-band boundaries in high-performance carbon FRCs. As kink-band formation is a principal failure mode in high-performance carbon composites under axial compression, accurate representation of fiber damage is

important in reproducing realistic kink-band formation which is necessary for a good prediction of composite compression failure.

FEMU method to determine carbon fiber orthotropic elastic properties

The Representative Volume Element (RVE) is the smallest volume over which an estimation of a certain material property can be extracted with a given precision. Size convergence study suggests that a relatively small RVE containing five (5) fibers with random cross-sectional distribution is sufficient to reproduce macroscopic elastic properties for UD FRC materials. Details on the implementation of the RVE with Periodic Boundary Condition (PBC) and the convergence analysis are presented in Appendix A.

In the study concerning fiber and composite orthotropic elastic properties, the FE RVE takes the following inputs:

- Fiber orthotropic elastic properties: $P^{fiber} = E_{11}, E_{22}, \nu_{12}, \nu_{23}, G_{12}, G_{23}$. It is assumed that properties in transversal directions equal, thus: $E_{22} = E_{33}$ and $\nu_{12} = \nu_{13}$.
- Matrix elastic properties: E_m, ν_m
- Fiber volume fraction: V_f. Fiber cross-sectional distribution is randomly generated using the Improved Random Search Algorithm (IRSA) that is described in Section 4.3.

The FE RVE produces the following outputs:

- Composite orthotropic elastic properties:

$$P^{composite} = E_{11}, E_{22}, \nu_{12}, \nu_{23}, G_{12}, G_{23}$$

Amongst the input parameters, matrix elastic properties E_m, ν_m and fiber volume fraction V_f are fairly easy to determine experimentally and are considered constants. E_m, ν_m of 8552 epoxy (Table 9) are provided by the manufacturer [62]. Therefore, the RVE FE simulation can be represented as a function:

$$P^{fiber} \xrightarrow{RVE\ FE\ simulation} P^{composite}$$

Both the input P^{fiber} and output $P^{composite}$ are vectors of 6 independent dimensions. It is thus possible to implement the FEMU scheme to determine fiber properties inversely from composite macroscopic properties. In this study, the inverse algorithm is implemented using the Python scripting feature of Abaqus/CAE. This FEMU procedure utilizes the Newton-Raphson algorithm with the Jacobian matrix computed through the finite difference method. Figure 11 presents the flowchart of this FEMU procedure. A consistent result on fiber properties is typically obtained within three iterations. Table 9 presents elastic properties of IM7/8552 carbon/epoxy matrix which were obtained through in-house experiments with macroscale specimens.

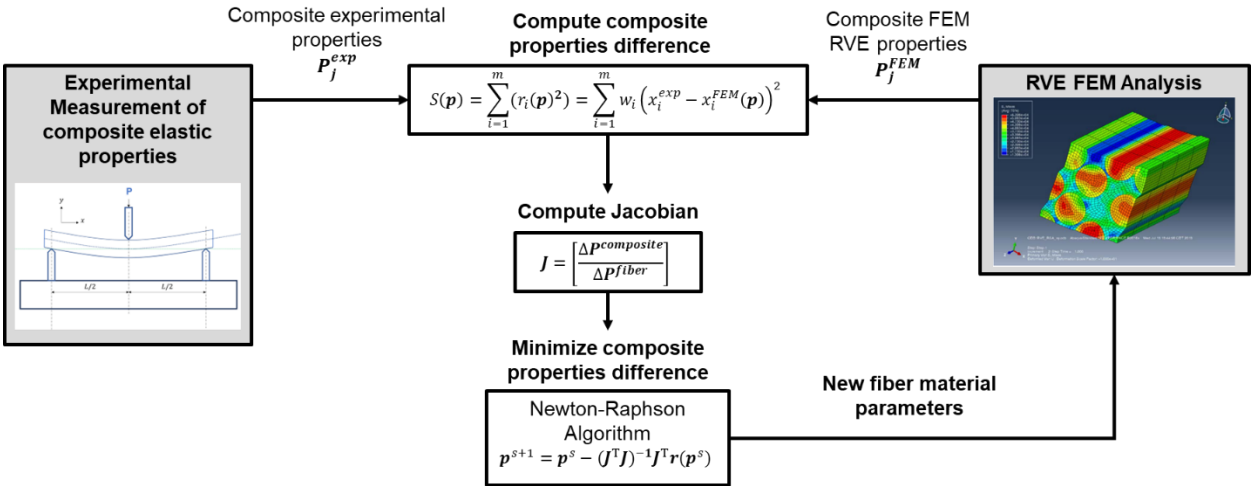

Figure 11. Flowchart of the FEMU process to determine reinforcing fiber elastic properties inversely from composite elastic properties.

Convergence study (details presented in Appendix A) suggests that a 5-fiber RVE is sufficient for elastic properties homogenization analysis. Using a 5-fiber RVE the FEMU analysis, IM7 carbon fiber's elastic properties result is presented in table 10 and compared with some values from the literature. The FEMU results are very close to the IM7 properties that Arteiro et al. utilized for their micromodel [84], while some results (most notably ν_{23} and G_{12}) differ significantly from the properties utilized by Shah et al. [85] and Pagano et al. [86]. In these articles, however, the authors did not provide information on how those properties were obtained. FEMU results are rather close to the properties found by Ballard et al. using a similar inverse characterization technique

with FE modeling [87]. Differences are possibly due to the difference of composite laminate properties provided to the FEMU algorithms.

Table 9. Elastic properties of IM7/8552 composite $P^{composite}$ for objective function. Elastic properties of 8552 epoxy matrix are considered constant.

	E_{11} (GPa)	E_{22} (GPa)	ν_{12}	ν_{23}	G_{12} (GPa)	G_{23} (GPa)
IM7/8552 composite	157	10.3	0.20	0.07	4.65	3.01
	E_m (GPa)	ν_m				
8552 epoxy matrix	4.67	0.39				

Table 10. Elastic properties of IM7 carbon fiber. Result from FEMU analysis of IM7/8552 composite.

	IM7 orthotropic elastic parameters					
	E_{11} (GPa)	E_{22} (GPa)	ν_{12}	ν_{23}	G_{12} (GPa)	G_{23} (GPa)
FEMU Results	276	15.0	0.20	0.07	15.0	7.03
Arteiro et al. [84]	276	15.0	0.20	–	15.0	7.00
Shah et al. [85]	276	19.5	0.28	0.25	70.0	7.80
Pagano et al. [86]	276	27.6	0.30	0.80	138	–
Ballard et al. [87]	276	22.4	0.27	–	12.0	7.53

Fiber longitudinal compression strength: Bending Beam

Figure 12 provides an illustration of the Bending Beam experiment for measurement of fiber critical compressive strain. The method measures the fiber compressive critical stress ε_{c11}^{o}, from which the compressive strength σ_{c11}^{o} can be deduced.

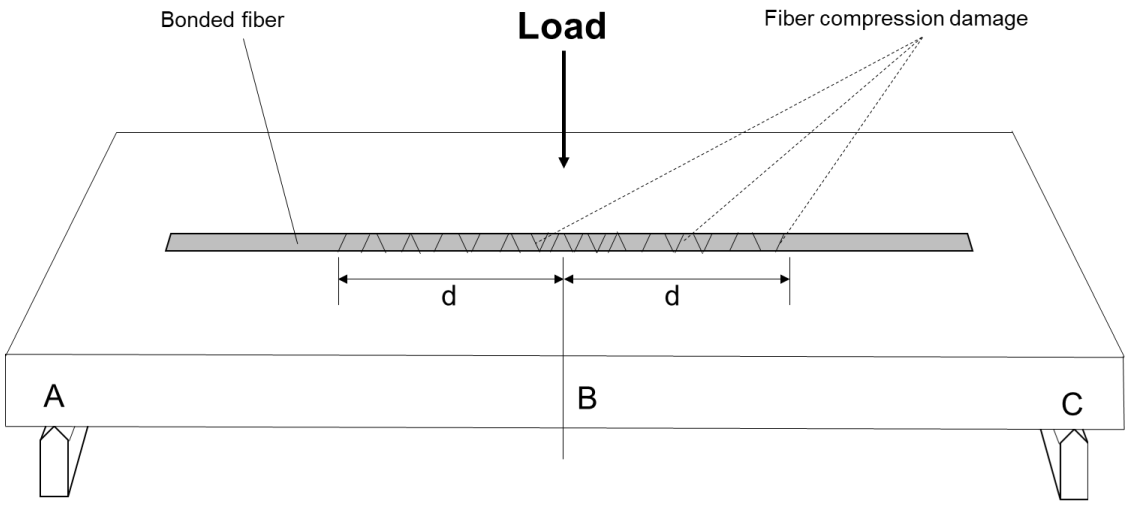

Figure 12. Concept of the Bending Beam method for fiber critical compression strain measurement. From fiber compression damage extension and beam dimensions, fiber critical strain can be deduced.

For the detailed presentation of the analytical analysis and feasibility study, please refer to Appendix B. Below are some important results from the analysis:

- Fiber critical compressive strain can be deduced from the dimensional extension of fiber damage d (Figure 12) through a linear relation:

$$\varepsilon_{c11}^{o} = C \times d$$

  where the coefficient C depends on the parameters: Load, beam material Modulus, beam geometry which are relatively easy to measure. This allows easy and robust result interpretation.

- Result interpretation can be further supported by FEM analysis and DIC analysis of the Bending Beam strain field.

- Bending Beam material should be PolyCarbonate thanks to its advantages: high Yield Strains allowing a wide range of compressive strain measurement for the bonded fiber; relatively low Modulus requiring lower Load from the bending machine; being ductile thus safer and easier to handle during test.

- Clear Acrylic or Urethane spray coating can be used as adhesive to bond the fiber to the Bending Beam. These adhesive agents were used and demonstrated by Deteresa et al. [46] and Fidan [59] in their studies. The

strength of these adhesives was reviewed and demonstrated to be sufficient to securely bond the fiber to the Beam.

- A reasonable example of Bending Beam dimensions was proposed and demonstrated to be compatible to all engineering requirements: maximum bonded fiber compressive strain; shear stress at fiber-bonding adhesive interface; maximum Load available from the bending test machine.
- Several recommendations regarding the test setup and specimen preparation to avoid some potential interference on the experimental results.

Berkovich indentation technique for epoxy microscale properties

Berkovich Tip assumes perfect geometry as described in ASTM - E2546 - 15. The manufacturer of the Berkovich Tip at AMSL provided the half angle $\alpha = 65.3$. Sanchez-Carmago et al. demonstrated significant effects of the imperfect tip geometry on the nano-indentation results (Load-Displacement curve) [74]. To verify the FEM model's geometry, total included angle of FEM Tip geometry is measured to be $\alpha + \theta = 142.3$. The SEM image of the newly purchased Berkovich tip also shows no sign of wear or damage (Figure 13).

Figure 14 presents the Abaqus FEM simulation of the nano-indentation test with the Berkovich tip on the 8552 epoxy.

The Berkovich tip is modelled as an analytical rigid, having infinite stiffness. The infinite stiffness simplification is taken thanks to the huge difference in Modulus of the diamond tip (order of $1000\,GPa$) and the epoxy sample (order of $5\,GPa$). The tip dimension is chosen to make sure the tip-sample contact area is fully covered within the pyramid surface.

The 8552 epoxy is modelled as an isotropic material. The epoxy is linear elastic before yield. Non-linear behavior is modelled with Concrete Damaged Plasticity properties. Reference properties and material parameters of the 8552 epoxy are presented in Table 6 and Table 7.

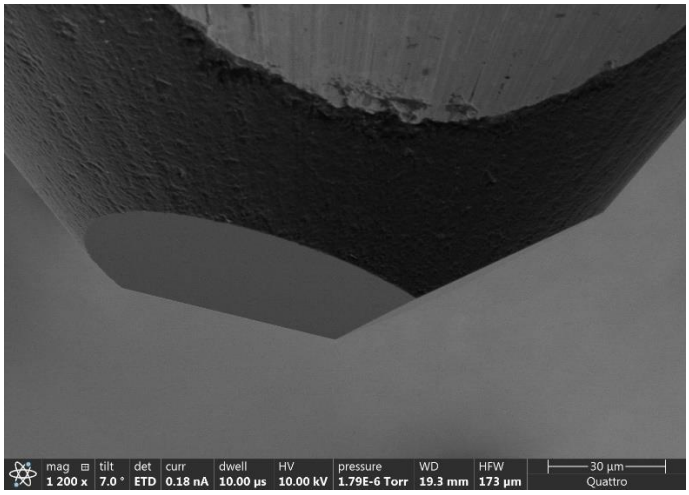

Figure 13. The newly acquired Berkovich tip shows no wear or damage.

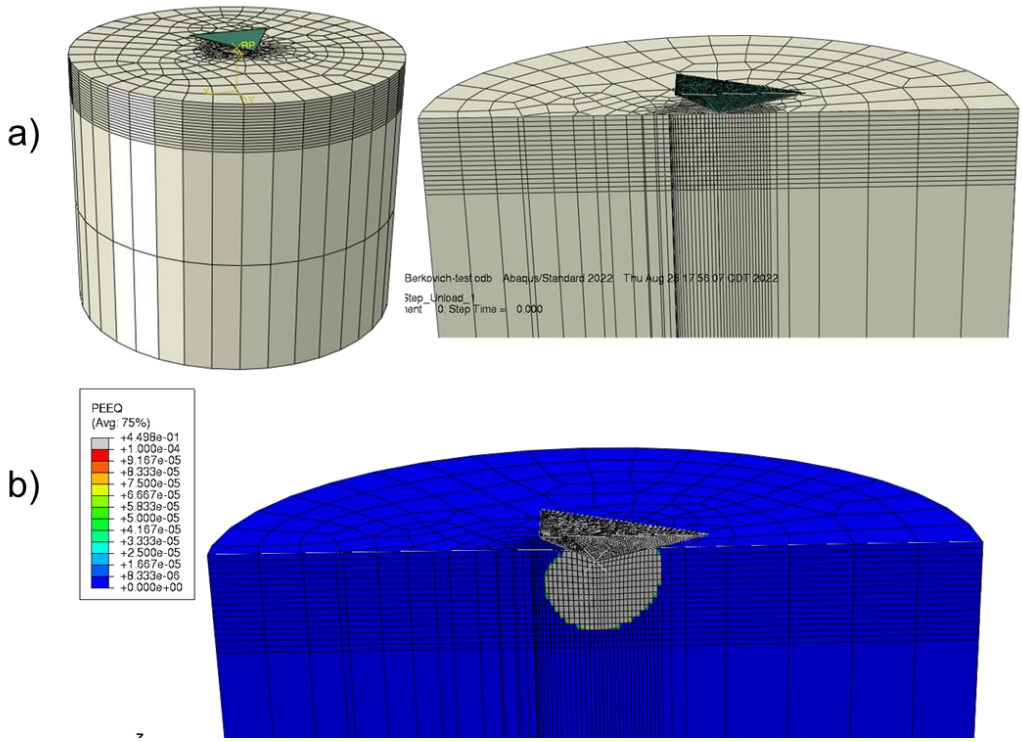

Figure 14. Berkovich test simulation: a) FE model, with high mesh density at the indented matrix area; b) Significant plastic damage area ($PEEQ > 0.01\%$) fully contained within high-density mesh volume.

The simulation utilizes the Static solver. The FEM epoxy sample is fixed at the lower cylinder surface (Figure 14.a, left). During the test, the FEM Berkovich tip is moved down to the same depth (compared to the initial sample surface) as in the

experiment, then the FEM tip is moved back to its initial position. The FEM tip assumes no rotation.

The mesh and size convergence of the model is based on the Peak Load attained. The size of the central, denser mesh area (Figure 14.a, right) is selected such that the plastic damage volume surrounding the indented epoxy area is fully contained within the dense-mesh volume (Figure 14.b).

Following the indentation, an indented mark is left behind (Figure 15.a). This effect is also produced in the FE simulation (Figure 15.b). In the indentation experiments, both the tip load-displacement curve and the indented mark geometry provide data for the determination of sample material properties.

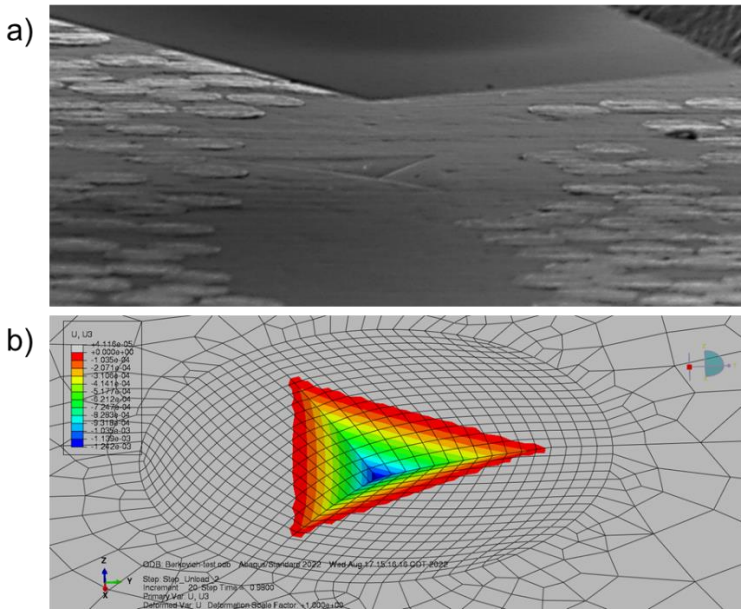

Figure 15. Following nano-indentation experiment: a) SEM image of indentation mark on HM63/8552 specimen; b) FEM result: vertical displacement showing indentation mark on the 8552 epoxy specimen.

Figure 16 presents results of the preliminary sensitivity studies on the effects of different epoxy properties on the indentation Load-Displacement curve. Tension Yield (Figure 16.a) and Fracture Energy (Figure 16.b) have almost negligible effects on the Load-Displacement curve. Meanwhile, Compression Yield (Figure 16.c) and plastic Dilation Angle (Figure 16.d) have very significant influence. This difference can be explained by the fact that the indented matrix is deformed mainly in compression.

These preliminary results suggest that the nano-indentation technique can be utilized to evaluate material compression properties. For the tension properties, however, other methods must be used.

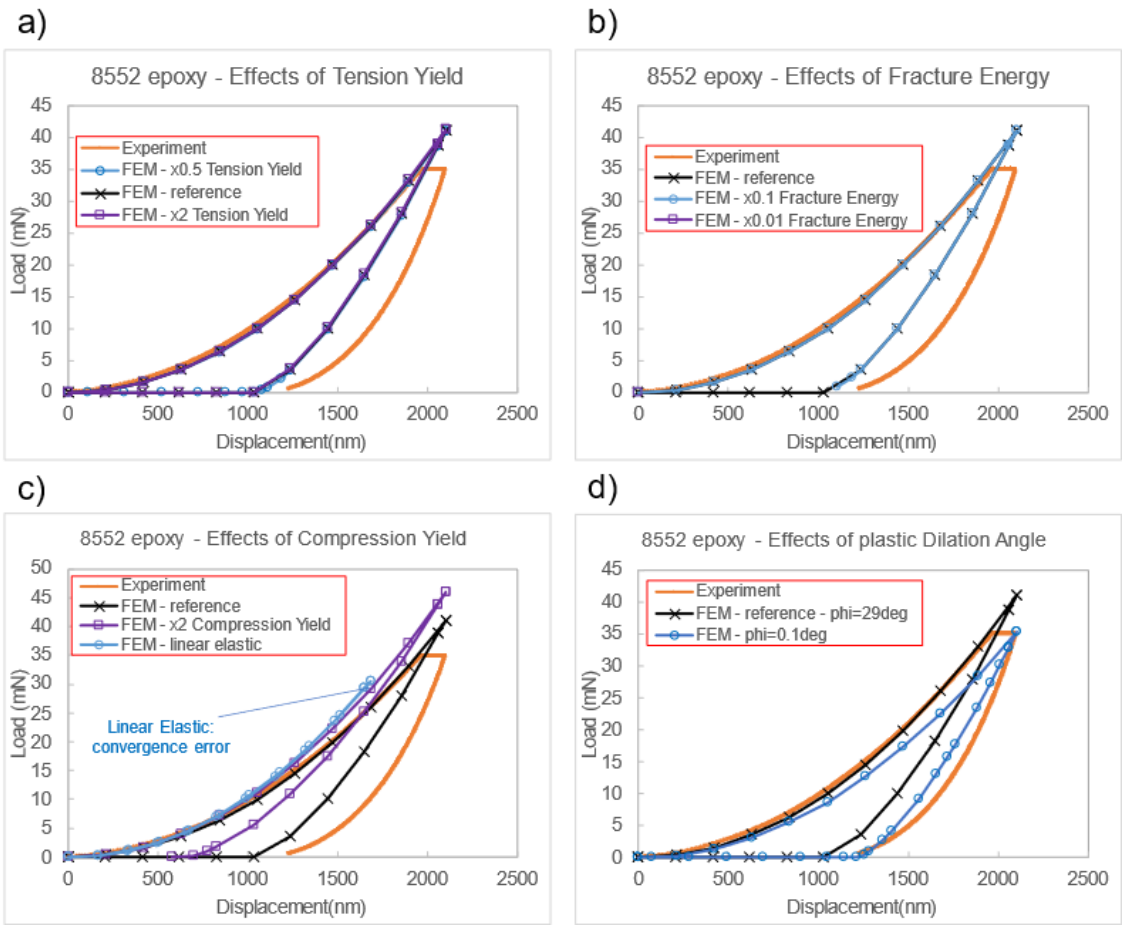

Figure 16. Effects of different epoxy properties on indentation Load-Displacement curve: a) Tension Yield; b) Fracture Energy; c) Compression Yield; d) Plastic Dilation Angle (phi)

3.6. Conclusions

A literature review was performed on microscale material properties of composite components, including fiber, matrix and fiber-matrix interface. Material parameters were classified based on the availability of their values in the literature, the potential impact on composite axial compression strength, and the availability of experimental characterization methods. Combined with results from FEM parametric analyses, in-

house experimental characterization is suggested to be performed on several selected material properties.

Amongst the selected properties, works on the micro-residual stress and the IFSS are presented in their own respective Chapter 4 and Chapter 5. For the characterization of micro-fiber orthotropic elastic properties, an FEMU procedure using macroscale composite properties as input was developed and demonstrated. For the in-situ characterization of matrix compression properties at microscale, a FE model was developed to evaluate results from the Berkovich indentation experiment. The Bending Beam method is recommended for the characterization of axial compressive failure in reinforcing fibers. Analytical evaluations on the feasibility and the results analysis of the Bending Beam method were provided.

CHAPTER 4

Study microscale residual stress in CFRP using Fiber Push-out experiment and FEMU evaluation

4.1. Introduction

Microscale residual stress in CFRP composite develops during the curing process due to the properties mismatch between the stiff fibers and the much softer epoxy matrix. For instance, the chemical shrinkage strain of CFRP epoxies is of the order of several percent [88]–[90], while the chemical strain of carbon fibers is relatively negligible [49]. During the cooldown phase, Coefficient of Thermal Expansion (CTE) mismatch between fibers and matrix generates residual stress. The CTE of common epoxies is around $50 ppm/^{o}C$, while the CTE of common carbon fibers is typically negative and of two orders of magnitude smaller. The manufacturing process of the composite specimens can generate additional residual stress. The presence of microscale residual stress can negatively affect macroscale performance of composites [15], [37], [60], [91], [92]. Therefore, accurate representation of residual stress in numerical micromodels might be critical for reliable computation of CFRPs properties.

Microscale residual stress is commonly introduced into the numerical model by applying the prescribed cure process of the corresponding composite [15], [37], [60], [91], [92]. However, key properties involving the microscale residual stress built-up are difficult to characterize experimentally. In addition, there exists a strong coupling of different effects including cross-linking shrinkage, thermal expansion, temperature and degree of cure affecting epoxy mechanical properties. These coupling effects contribute to the difficulty of a reliable representation of microscale residual stress in a heterogenous composite [93]. The very small scale of the numerical micromodel adds to the complexity of any experimental verification of the computed residual stress.

While there exists many experimental methods for residual stress measurement in polymer matrix composite at ply scale, very few methods are currently available at microscale [94]. Residual stress is commonly characterized indirectly through the residual strain that is deformation from material's relaxed state. Experimentally

observed strains can be compared with strains generated by the numerical models to validate and deduce the residual stress field present in the specimen. At microscale, two main challenges exist: the material removal for destructive methods in which removed materials relaxes some residual stress leading to observable relaxing deformation; and the measurement/observation of strain and displacement with both destructive and non-destructive methods.

Some difficulties related to material removal might be overcome using non-destructive methods. The Raman spectroscopy is a non-destructive method measuring the molecule vibration modes which can be related to residual stress in a crystalline microstructure and allows sub-micrometer resolution [95]–[98]. However, application of this method to amorphous materials leads to poor resolution [99]–[101], making the method unsuitable to characterize residual stress in the thermoset epoxy matrix of the CFRPs. X-ray diffraction allows non-destructive measurement of microscale residual stress, but a crystalline microstructure is also required [102]. Predecki et al. [103], [104] investigated a solution for the application of X-ray diffraction method in which crystalline microparticles are dispersed into the amorphous epoxy resin medium and X-ray diffraction associated with the microparticles is measured. However, interaction between different materials as well as particle geometric effects are complex and incompletely characterized, making it difficult to interpret, quantify and validate microscale residual strain in the epoxy medium.

The Photoelasticity method, a non-destructive method allowing visualization of strain fields at microscale [105], [106], is worth discussing. The method was initially limited to composites with low fiber volume fraction due to the requirement of light transmission through the specimen. This limitation was solved by Andersson et al. [107] by cutting and polishing a thin composite membrane specimen with plane perpendicular to the fiber direction. The authors [107] reported good correlation between FEM-generated strain field and the experimental optical patterns. However, when the authors applied an extra in-plane load on the specimen, FE model predicted very high additional strain due to this extra load, but the experimental optical patterns changed very little and do not verify the FEM prediction. From these results, the nature of the visualized optical

features seems to be unclear, and any interpretation of the residual strain from experimental optical patterns should be performed with care.

The Incremental Micro-Hole-Drilling with DIC (digital image correlation) method [108] is potentially applicable to measure microscale residual stress in composites. The destructive method utilizes ion beam to remove material and create a hole at microscale. Microparticles are randomly dispersed on the specimen surface, allowing DIC observation of relaxed residual strains, providing input for FEM analysis. The method works with both crystalline and amorphous materials, allowing potential application to the epoxy matrix of CFRPs. In the published literature, however, the method has not been applied to composite materials.

This study proposes an approach to characterize residual stress in composite matrix at the scale of reinforcing fibers by evaluating the Fiber Push-Out experiment [109]. In this methodology, fibers surrounding a matrix-rich pocket are pushed out. After the Push-Out of this group of fibers, local in-plane and out-of-plane matrix deformations are visible under SEM. These deformations are attributed to the relaxation of the residual stress stored in nearby matrix due to broken fiber-matrix interfaces. The resulting matrix deformation is measured in the out-of-plane direction using a nanoindenter and compared with results from the corresponding numerical model. A FEMU procedure is proposed to evaluate and characterize the residual stress field present in the specimen [109]. The FE geometry is created based on SEM images of the specimen. In the FEMU algorithm, material properties related to residual stress build-up are optimized such that the difference between FEM-predicted and experimentally measured matrix deformation is minimized. After algorithm convergence, the residual stress can be assessed using the resulting FE model. As some fiber-matrix interfaces are irreversibly broken in the push-out experiment, this technique can be classified as a destructive method.

The proposed method is applied and demonstrated on the HS40/F3G carbon/epoxy composite that represents CFRP composites in aerospace application. This work therefore bridges the gap between microstructure modelling to the prediction

of macroscale properties by providing an experimental validation of the numerically generated residual stress at microscale.

4.2. Methodology

The technique of fiber push-out experiment with in situ SEM was originally developed at AMSL, UTA for the measurement of interfacial shear strength (IFSS) in CFRPs. Live monitoring of the process showed significant matrix deformations in both in-plane and out-of-plane directions. The out-of-plane deformation increases as more fibers are pushed out around a matrix-rich area. This is attributed to the increasing amount of residual stress being relaxed in the matrix as the bonding with the much stiffer fibers are broken. This phenomenon is illustrated schematically in Figure 17. Figures 18.a and 18.b present an example of the observed matrix sink-in after fibers push-out. The vertical position of the central matrix-rich area is measured using the nanoindenter readings by gradual lowering the probe until the non-zero load was picked up. The matrix sink-in was verified and measured by comparing the matrix vertical positions before and after fibers push-out (Figure 18.c).

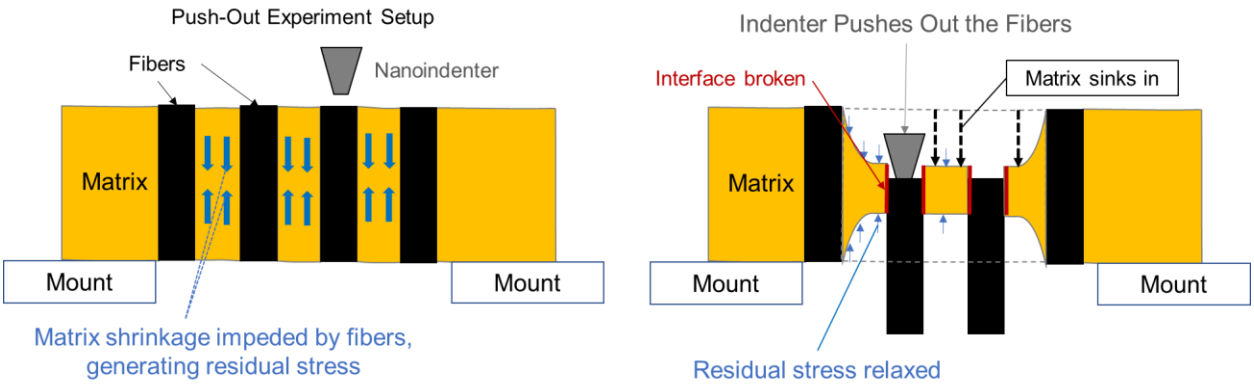

Figure 17. Illustration of the fiber push-out experiment. Residual stress in matrix is partially relaxed due to the broken interface, causing matrix deformation.

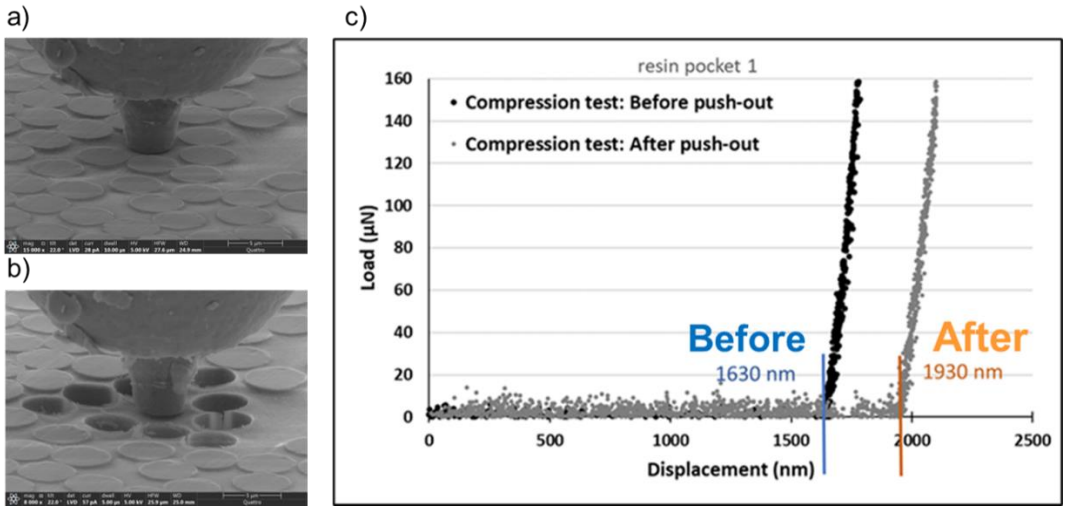

Figure 18. Matrix sink-in measurement using the nanoindenter: a) Before fiber push-out; b) After fiber push-out; c) Matrix sink-in is measured by comparing load-displacement data. [109]

An FEMU procedure is employed to perform an inverse characterization of the material properties inducing the residual stress associated with the matrix sink-in deformation [109]. Figure 19 presents the flowchart of the FEMU process. In this study, the FEMU procedure optimizes the epoxy chemical shrinkage due to curing, to minimize the difference between experimentally measured matrix sink-in and the corresponding FEM-computed matrix sink-in. The choice of epoxy chemical shrinkage as the optimizing variable is driven by several factors: chemical shrinkage is an important contributor to the residual stress formation; experimental measurement of chemical shrinkage is challenging and random variations might occur at microscale due to the heterogenous nature of the composites. The FEMU procedure is written and implemented in Abaqus/CAE using the integrated Python scripting feature.

The FEMU procedure utilizes the Gauss-Newton optimization algorithm. The Jacobian matrix is computed through the finite difference method. By iterating the epoxy chemical shrinkage ε_0^{chem}, the algorithm minimizes the difference between FEM-computed and experimental matrix sink-in:

$$\Delta^s = |Sinkin^{FEM} - Sinkin^{exp}|$$

The iteration procedure is stopped when the difference reaches the convergence threshold of $\Delta^s < 1\,nm$, corresponding to a relative difference of approximately 0.3% of

the experimental sink-in measurement (see Section 4.4). Convergence is typically achieved within three iterations.

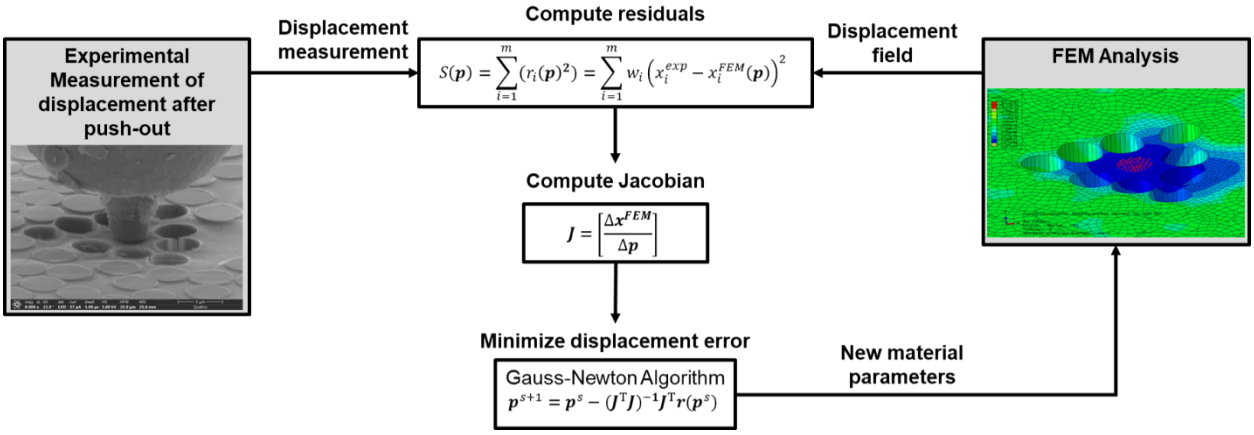

Figure 19. Flowchart depicting the FEMU procedure for the inverse characterization of material properties. [109]

4.3. Finite Element Model

Setup for the Fiber Push-Out experiment

In this study, the HS40/F3G composite specimen is cut and polished into a thin membrane perpendicular to the local fiber direction, with the thickness in range of $20 - 30\,\mu m$. The specimen is placed on a steel mount with an approximately $50\,\mu m$ wide groove, with its outer parts taped down to the fixture. A flat-end diamond indenter with $4\,\mu m$ diameter is used to perform the fiber push-out and the measurement of matrix vertical displacement. Figure 20 presents the experiment setup and the in-situ SEM image of the experiment. FE models in this Chapter are based on fiber push-out experiments under this setup.

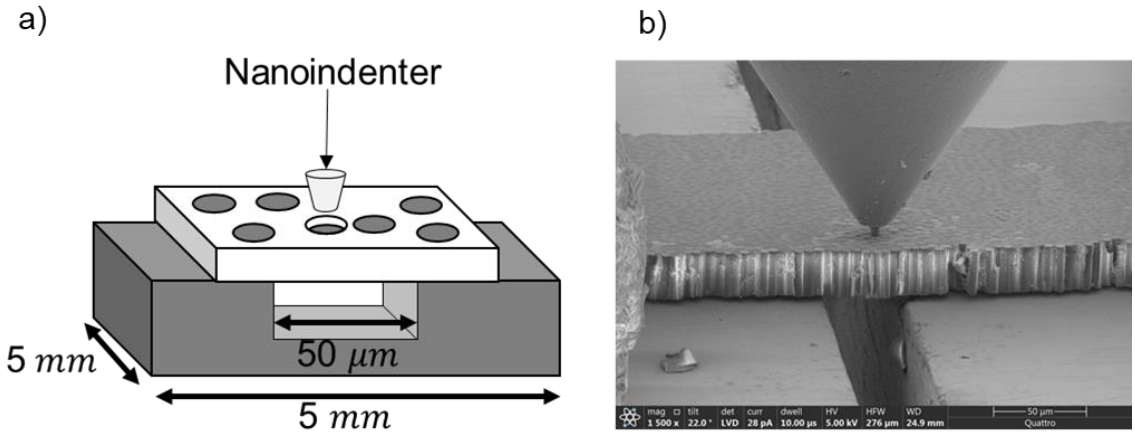

Figure 20. a) Fiber push-out experiment setup; b) SEM image showing the free-standing push-out configuration.

Specimen geometry and mesh generation

Microscopy images provide details on the in-plane fiber geometry and the out-of-plane dimension of Push-Out specimens. The creation of FE geometry from specimen geometry comprises three Steps, as depicted in Figure 22 [109].

In Step 1, the identification of fibers from the in-plane microscopy images is accomplished through the application of the Hough Circle Transform algorithm for the circle detection that is accessible through the OpenCV library of the Python programming language. Fiber cross-sections are assumed to be circular. The algorithm detects the circular fibers on an Inner Zone surrounding the Push-Out Fibers. A few missed detections are corrected manually. To facilitate the meshing of the FE geometry, pairs of circles that are too close or overlapping have their radii proportionally adjusted to achieve a minimum distance equal to 0.08 times the typical HM carbon fiber radius of $R_f = 2.47\ \mu m$. Figure 22.a presents the in-plane fibers geometry obtained from Step 1.

In Step 2, the limit for an Outer Zone is manually defined according to specimen in-plane geometry. The Outer Zone is populated with randomly generated fibers distributed in a random pattern and having the same radius R_f. All fibers, detected and randomly generated, respect the minimum distance of $0.08 \times R_f$. Fiber generation utilizes an Improved Random Search Algorithm (IRSA) which is built upon the classical Random Search Algorithm (RSA). The “jamming” problem of the original RSA limits the

resulting Volume Fraction to less than 50%, significantly lower than the typical fiber Volume Fraction of 60% to 70% in aerospace composites. The IRSA solves the jamming problem by iterating through the generated circle, pulling each circle towards nearby existing circles by random distances, thus freeing spaces to generate new fibers. In this Chapter, the fiber generation algorithm seeks an objective Volume fraction of 54%.

The above-described process assumes several simplifications: specimen surface is perfectly flat and parallel to the image plane and there is no distortion in the SEM images. With SEM-provided scaling ratio, the projection $\boldsymbol{P_I^{-1}}$ transforms the specimen image geometry $(\boldsymbol{x_I}, \boldsymbol{y_I})$ into an in-plane specimen geometry in the real coordinates system $(\boldsymbol{x_A}, \boldsymbol{y_A})$:

$$\begin{pmatrix} \boldsymbol{x_A} \\ \boldsymbol{y_A} \end{pmatrix} = \boldsymbol{P_I^{-1}}(\boldsymbol{x_I}, \boldsymbol{y_I}) = \begin{bmatrix} Mag_I & 0 \\ 0 & -Mag_I \end{bmatrix} \begin{pmatrix} \boldsymbol{x_I} \\ \boldsymbol{y_I} \end{pmatrix} + Mag_I \begin{pmatrix} -C_x \\ C_y \end{pmatrix}$$

With Mag_I being the image scale ratio. (C_x, C_y) is the real coordinate center that can be arbitrarily selected on the image. Figure 21 provides an illustration of the relation between the two coordinate systems.

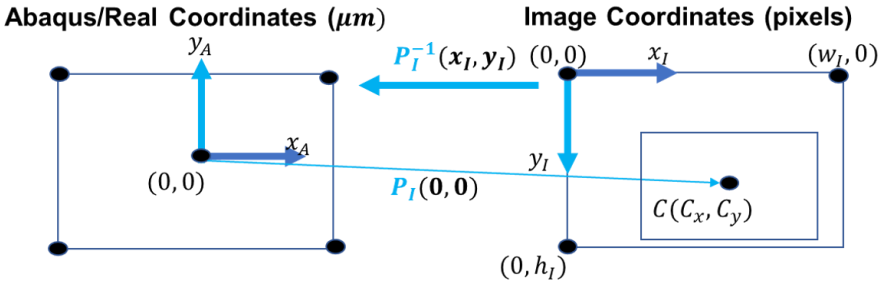

Figure 21. Projection allowing transforming features between Image and Real/Abaqus coordinate systems.

In Step 3, based on the in-plane specimen geometry obtained from previous Steps, a 2D surface geometry is generated in Abaqus and meshed using the integrated meshing tool (Figure 22.c). The 3D FE geometry is created through the extrusion of the 2D meshed geometry by the membrane specimen thickness that is assumed to be uniform (Figure 22.d). The geometry shown in Figure 22 belongs to the Sample 4 Area 1 that is utilized as reference FE model in this Chapter.

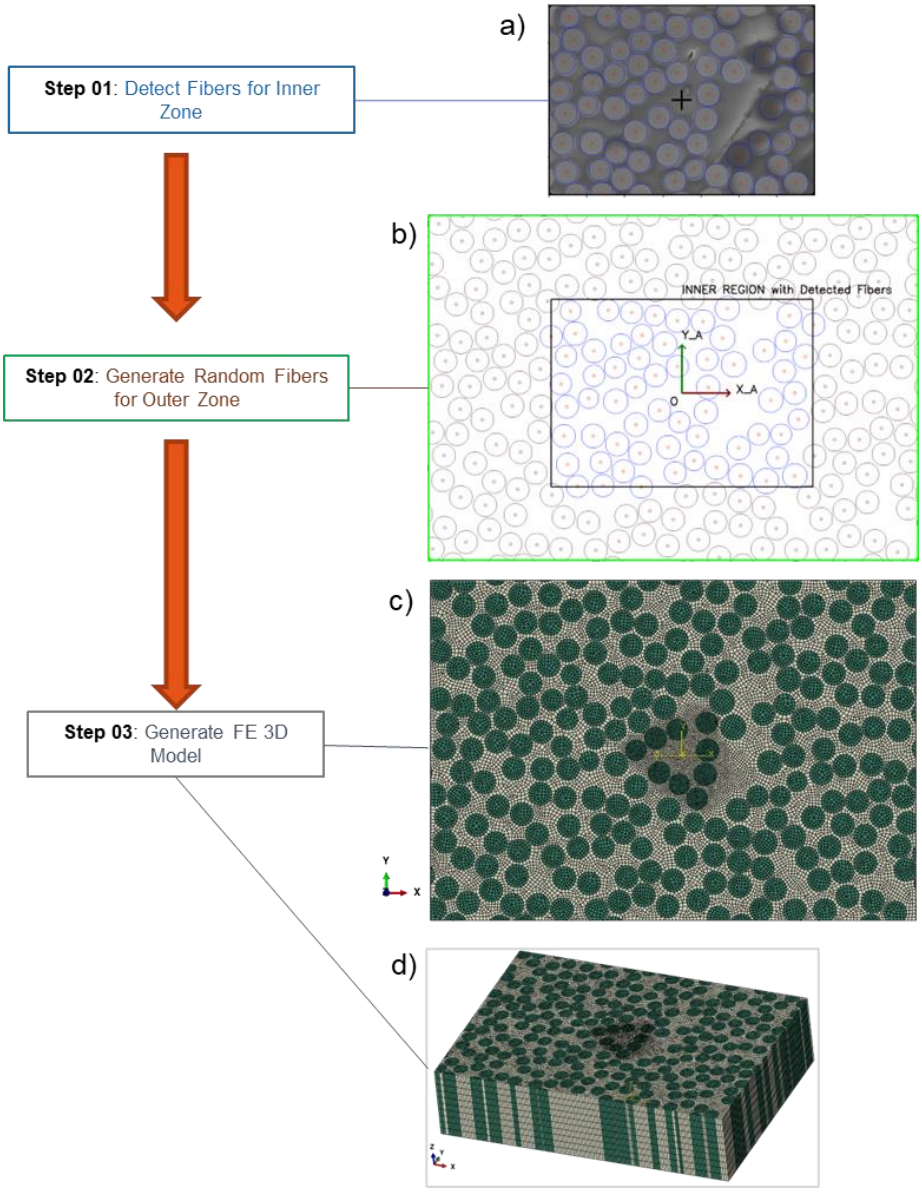

Figure 22. Generating 3D FE geometry based on microscopy data: a) Inner Zone with blue colored detected fibers; b) Brown colored generated fibers for the rest of the model; c) 3D FE model, top view; d) 3D FE model, oblique view. [109]

Mesh and size convergence analyses have been performed. Convergence is assumed when significant changes in mesh or size parameters have insignificant effects on the matrix sink-in deformation. Details on these convergence studies are presented in Appendix D.

FEM Analysis Steps and matrix Sink-in measurement

Figure 23 illustrates the three processes replicated in the FE simulation: curing; specimen grinding and polishing; and the fiber push-out experiment [109]. The numerical study utilizes the Fully Coupled Temperature-Displacement analysis available in Abaqus.

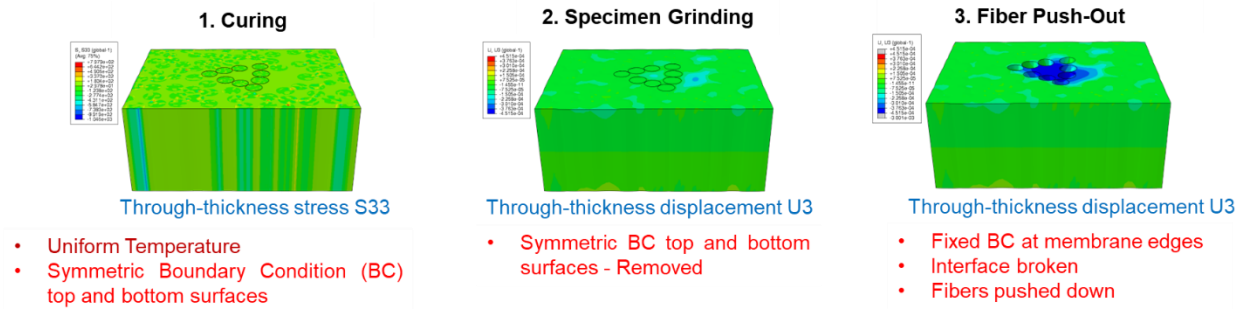

Figure 23. Three processes in the FEM analysis. Fiber and matrix shrinkage mismatches during curing generate through-thickness tension stress in matrix. Significant matrix sink-in deformation on the upper surface due to relaxed residual stress is visible after fiber push-out. [109]

Throughout the simulation, the model assumes a uniform temperature field simplification. The curing temperature profile of the F3G epoxy is applied. To assess the rationality of this simplification, a thermal conduction analysis was performed on a $1\ cm$-thick ply of IM7/8552 using available exothermic curing heat measurements. Over a distance of $40\ \mu m$ characteristic size of FE models in this Chapter, the resulting maximum temperature gradient was significantly lower than $1\ ^{o}C$. Therefore, the uniform temperature field is a reasonable simplification.

During the curing process, the evaluated volume is assumed to be situated deep inside a large composite material volume with negligible through-thickness deformation due to high stiffness and insignificant fiber-direction curing expansion or shrinkage. Accordingly, symmetry boundary condition is applied on model surfaces initially normal to the fiber direction which corresponds to specimen upper and lower surfaces (Z-surfaces). Supposing a lack of external constraint in the UD composite transversal directions, model surfaces corresponding to the membrane edges (X-surfaces, Y-surfaces) are free of constraints. To verify the validity of the application of macroscale boundary conditions on the microscale FE model, a size convergence study of the

generated residual stress with models up to 16 times the reference in-plane area was performed. The residual stress convergence in model size was successfully verified. Through inductive inference, the convergence study demonstrated the validity of the application of macroscale in-plane boundary conditions (BCs) to a micromodel bigger than a certain minimum (convergence) size for the purpose of residual stress analysis. Details on this convergence analysis are presented in Appendix E.

Through the grinding process, symmetry constraints are removed from the Z-surfaces to model the manufacturing processes which expose the upper and lower membrane surfaces of the studied specimen.

During the curing and the grinding processes, the fiber-matrix interface assumes perfect bonding. To achieve this, the applied Penalty Contact and No Separation properties prevent normal penetration and separation, and the applied Rough Friction property prevents tangential sliding.

During the push-out process, the specimen fixture is represented by the fixed boundary conditions on the X-surfaces and Y-surfaces. The model simplifies the push-out process by dividing this into two separate sub-steps. First, the fiber-matrix interface is broken, which is represented by allowing normal separation with frictionless tangential slipping through a model change in contact properties. Subsequently, the fibers push-out movements are represented by applying an out-of-plane displacement on their corresponding upper surfaces.

In the FE model, a group of “probed nodes” represents the area of nanoindenter contact for sink-in measurement, which are colored in red in Figure 24.a,b. The probed nodes are located on a circular area with the same radius as the nanoindenter flat tip ($radius = 2\mu m$). The Z/vertical coordinate measurement takes the node with highest vertical coordinate as representative of the probed area. Figure 24.c presents an example of the Z-coordinate evolution of the probed area during the simulation. The symmetry boundary conditions fix its Z-coordinate during curing. After grinding, the vertical constraints are removed, relaxing some residual stress and leading to some matrix sink-in. Fiber push-out breaks the interfaces and releases more residual strain,

causing more matrix sink-in corresponding to the sink-in that is experimentally measured.

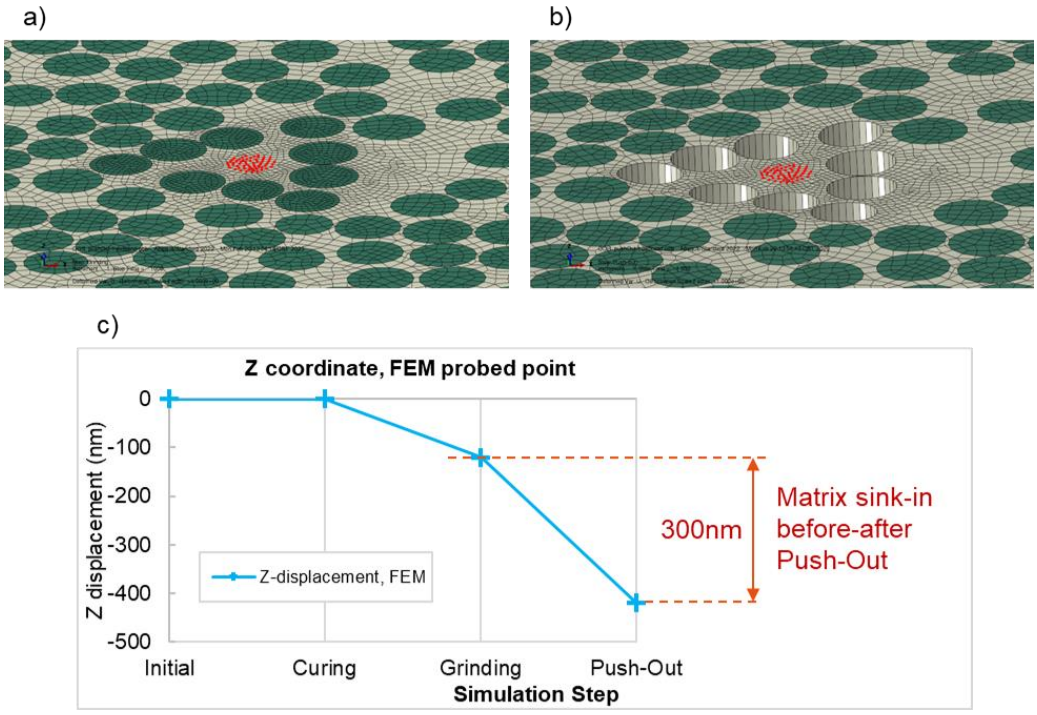

Figure 24. a) Probed nodes (red) before fiber push-out; b) After fiber push-out; c) Z-coordinates of the probed area provides sink-in measurements. [109]

Material models and properties

The material behaviors during the curing of the epoxy matrix are described by the Abaqus built-in material curing model. For the epoxy materials, the ratio: $\alpha = Q/Q_{tot}$ is commonly utilized as the "Degree of Cure", where Q is the accumulated exothermal reaction heat and Q_{tot} is the total exothermal heat from fully cured epoxy. The Kamal curing kinetics is a popular model providing a semi-empirical description of the DOC evolution in thermoset plastics [37], [110], [111]. This study utilizes the following form of the Kamal equation for the epoxy curing kinetics:

$$\dot{\alpha} = A_1 \exp\left(-\frac{\Delta E_1}{RT}\right)(1-\alpha)^n + A_2 \exp\left(-\frac{\Delta E_2}{RT}\right)\alpha^m(1-\alpha)^n \qquad (4)$$

where $\dot{\alpha}$ is the rate of cure; R is the gas constant; T is the absolute temperature and $m, n, A_1, A2, \Delta E_1, \Delta E_2$ are effectively experimental fitting parameters (though several authors assigned specific names to these parameters [37], [111]). The Abaqus built-in curing kinetics model utilizes the Kamal equation with the expression as a sum of N terms:

$$\dot{\alpha} = \sum_{i=1}^{N} Z_i e^{-\frac{E_i}{RT}} (b_i + \alpha^{m_i})(\alpha_{max} - \alpha)^{n_i} \quad (5)$$

where Z_i, E_i, m_i, n_i are material parameters. b_i is the initial rate of cure. Setting $b_i = 0$, we can define a linear transformation of parameters to rewrite Kamal equation form (4) into Kamal equation form (5) with only six independent parameters.

The set of material parameters $(m, n, A_1, A2, \Delta E_1, \Delta E_2)$ can be obtained through the fitting with experimental DOC data. The curve-fitting algorithm seeks to minimize the following sum:

$$\boldsymbol{S} = \sum_{i}^{M} \boldsymbol{\Delta}_i \quad (6)$$

where M is the total number of experimental cases provided to the algorithm. For the experiment number i, $\boldsymbol{\Delta}_i$ measures the difference between experimental DOC history and modeled DOC history:

$$\boldsymbol{\Delta_i} = \sum_{j} \left(DOC^{exp}(t_j) - DOC^{model}(t_j) \right)^2 \quad (7)$$

where $DOC^{exp}(t_j)$ and $DOC^{model}(t_j)$ are respectively experimental DOC and modeled DOC measured at time point t_j. Experimental data are processed such that:

- For each experiment, time points t_j are spaced at roughly equal intervals.
- Each input experiment consists of DOC at about 40 time points. As such, each experiment case carries roughly the same “weight” into the sum presented in equation (6).

The inverse/curve fitting algorithm by minimizing the sum (6) is written in Python and employs the function $least\_squares$ from SciPy library. This optimization algorithm is based on the Trust Region Reflective method. The algorithm stops when the change in optimizing parameters $(m, n, A_1, A2, \Delta E_1, \Delta E_2)$, in gradient, or the optimized cost function becomes smaller than given tolerances, or when the maximum number of iterations has been reached. The algorithm seeks not the best fit to a particular experiment, but a single value for the set of material parameters $(m, n, A_1, A2, \Delta E_1, \Delta E_2)$ which provides the best fit to all provided experimental cases.

Due to the lack of data on this new epoxy, the concerned F3G in this study assumes the same curing kinetics as its base F4A, both having the standard curing temperature of 121^oC. Schechter et al. [112] utilized the following expression for the F4A curing kinetics:

$$\dot{\alpha} = A\, exp\left(-\frac{E_a}{RT}\right) \times \frac{\alpha^m (1-\alpha)^n}{1 + exp(C(\alpha - (\alpha_{C0} + \alpha_{CT} T)))} \tag{8}$$

where $A, E_a, m, n, C, \alpha_{C0}, \alpha_{CT}$ are curing kinetics parameters. Schechter et al. studied curing kinetics of F4A under four temperature configurations: four ramps: $1,2,3,5^oC/min$ and four isothermal dwells between 100^oC and 130^oC. They fitted equation (8) to these results and obtained the curing parameters in Table 11.

Table 11. Cure kinetic constants for F4A epoxy resin by Schechter et al. [112].

Kinetics Parameter	Value	Unit
A	4.86×10^{-7}	s^{-1}
E_a	70338	J/mol
m	1.34	$-$
n	1.88	$-$
C	4.36	$-$
α_{C0}	1.15×10^{-7}	$-$
α_{CT}	1.21×10^{-3}	K^{-1}

To obtain Kamal equation's parameters for F3G/F4A epoxy resin, an analytical transformation from equation (8) to equation (4) might be complex. Instead, an alternate approach is proposed that consists of 2 steps. First, using Schechter's parameters and kinetics equation (8), virtual experimental data is generated for the eight experimental cases according to Schechter et al.'s description that were used for curve fitting to

obtain parameters presented in Table 11. Data for eight virtual experiments with the following temperature profiles are generated: four ramps at $1, 2, 3, 5^{o}C/min$ and four isotherms at $100,110,120,130^{o}C$. Initial DOC is assumed to be 0.005. Next, data of these eight virtual test cases is provided to the inverse algorithm described above to find Kamal equation parameters.

Table 12 presents the Kamal curing kinetics parameters (Equation (4)) that were found to fit the 8 described virtual test cases. Figure 25 shows the DOC data from the virtual curing experiments along with their fits to the Kamal equation.

Table 12. F4A/F3G Kamal curing kinetics constants, obtained through virtual experiment curve fitting. [109]

Kinetics Parameter	Value	Unit
m	1.29	-
n	2.70	-
A_1	2.32×10^{15}	s^{-1}
A_2	3.20×10^{7}	s^{-1}
ΔE_1	1.50×10^{5}	J/mol
ΔE_2	6.99×10^{4}	J/mol

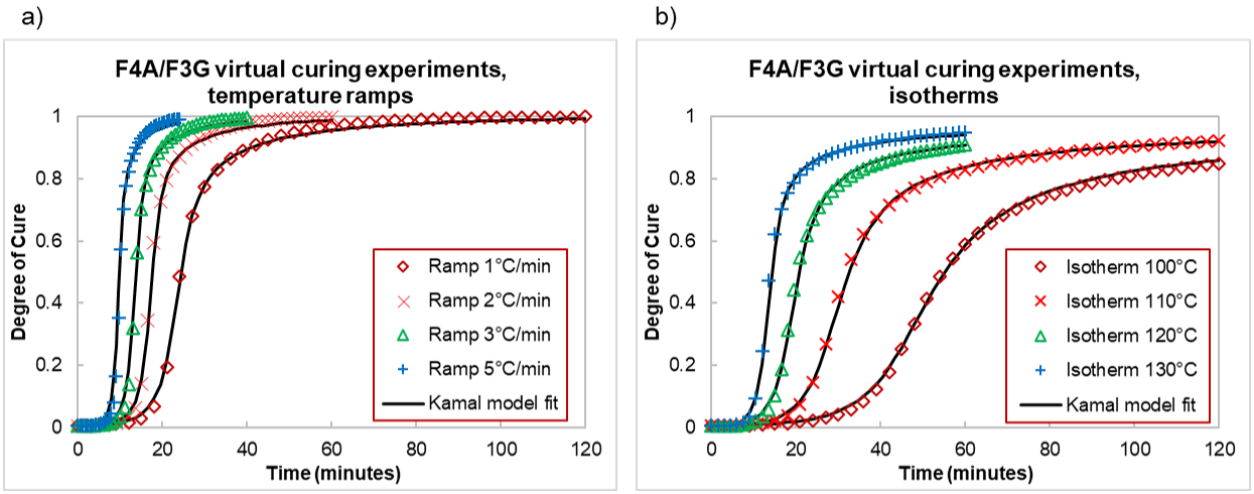

Figure 25. Virtual experiment DOC data and their fits to the Kamal curing kinetics: a) Cases with temperature ramps; b) Cases with isotherms. [109]

This study applies the manufacturer-provided curing temperature profile for F3G on the model. The curing cycle includes a ramp of approximately $1.6\,^{o}C/min$ to $121\,^{o}C$, a two hour-dwell at $121\,^{o}C$, and cooling at approximately $-1.6\,^{o}C/min$ down to ambient temperature. The curing temperature profile and the DOC evolution of F3G matrix in this study are presented in Figure 26.

In the epoxy curing model, the isotropic, linear chemical shrinkage ε_0^{chem} corresponds to the fully cured epoxy ($DOC = 100\%$). Chemical shrinkage is proportional to the epoxy DOC: $\varepsilon^{chem} = \varepsilon_0^{chem} \times DOC$. In the FE model, the final DOC is 96.7%.

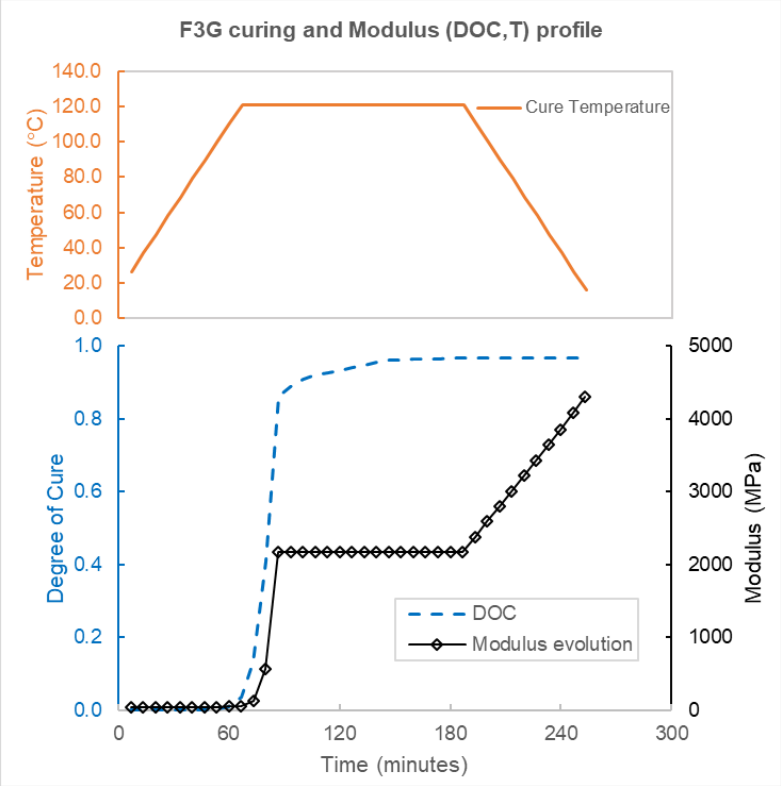

Figure 26. Curing Temperature and Modulus evolution of the F3G epoxy material model. [109]

F3G epoxy material model assumes an isotropic, linear elastic behavior. Table 13 presents final properties of the F3G epoxy following the curing process. The modulus is obtained through tensile tests. The CTE is provided by the manufacturer. The Poisson ratio is estimated as typical for epoxies. Amongst material properties, only the modulus varies during the curing cycle. The epoxy modulus is dependent on both DOC and temperature, and is provided to the Abaqus simulation using a data table. Precise determination of modulus dependence on DOC and temperature during the curing process is difficult due to the strong coupling between the temperature, rate of cure with the resulting exothermal heat and the heat transfer as the specimen is being cured [93]. In this Chapter, the modulus development during the curing cycle is shown in Figure 26. The initial modulus is 1% of the final modulus. The FE model does not describe explicitly the chemical cross-linking and the bonding development at the fiber-matrix

interface. Instead, an equivalent approach is used where the tied contact leads to zero relative displacement at the interface, and the force transmission at the interface and its evolution happens directly through the matrix modulus development as a result.

In this study, the F3G material model assumes no plasticity damage. This simplification is taken due to the lack of data on the new F3G epoxy on top of the lack of an accurate, validated model for the description of the very complex dependence of epoxy damage properties on many parameters including local temperature [15], [62], degree of cure [37], humidity [15], [62], all of which are also difficult to determine experimentally for a curing specimen. Due to this simplification, only the specimens without visible significant matrix damage are considered for the FEMU studies.

Table 13. F3G epoxy final properties after the curing process.

Elasticity	$E(MPa)$	ν
	4300	0.39
Thermal properties	$CTE(ppm/^oC)$	
	42.7	
Curing properties	ε_0^{chem}	
	$variable$	

The HS40 carbon fiber model includes orthotropic, linear elastic properties with isotropic thermal expansion. Its material parameters are presented in Table 14. HS40 axial modulus is provided by the datasheet [113]. Other properties are estimated.

Table 14. HS40 carbon fiber material properties.

Elasticity	$E_{11}(GPa)$	$E_{22}(GPa)$	$E_{33}(GPa)$	ν_{12}	ν_{13}	ν_{23}	$G_{12}(GPa)$	$G_{13}(GPa)$	$G_{23}(GPa)$
	455	13	13	0.3	0.3	0.46	11.3	11.3	44.5
Thermal properties	$CTE(ppm/^oC)$								
	-0.7								

The fully coupled thermal-stress analysis also requires material thermal conductivity, mass density, and specific heat. However, these parameters have no influence on the FEM results due to the application of a uniform predefined temperature.

The fibers and matrix FE volumes comprises C3D6T and C3D8T-type 3D elements.

4.4. Results and discussion

FEMU results and application to predict matrix sink-in [109]

Five different FE geometries corresponding to the five experiments are analyzed using the FEMU algorithm. Only the push-out test areas without significant matrix damage are selected for the FEMU studies to correspond with the simplification of a linear elastic matrix. Figure 27 presents the SEM images and corresponding FE geometries of these five fiber push-out areas. Table 15 presents the parametric chemical shrinkage ε_0^{chem} results from FEMU analyses of these five experiments. The inversely calculated chemical shrinkage values are relatively consistent with a Coefficient of Variation of 17.1%.

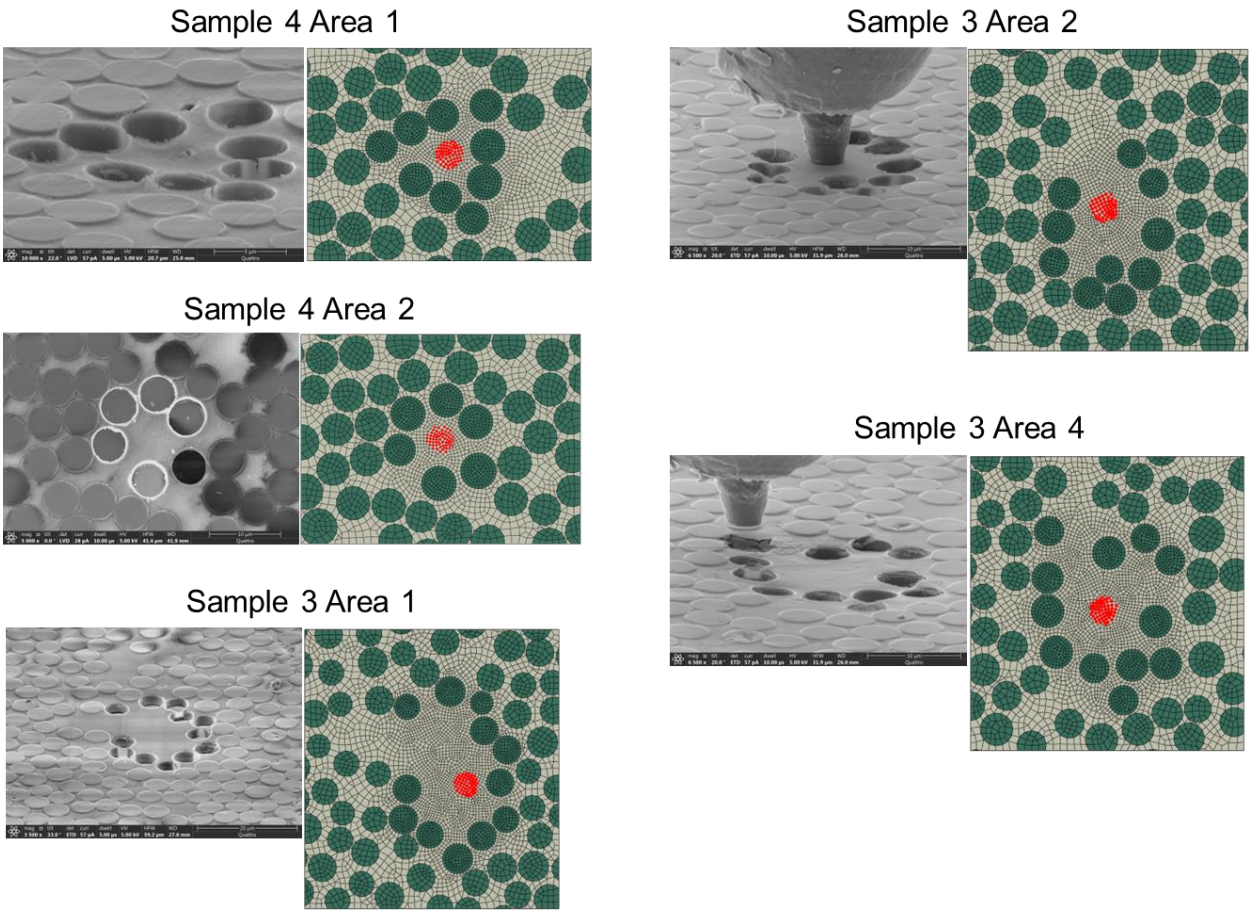

Figure 27. SEM images and corresponding FE geometries of fiber push-out areas in the FEMU analysis.

Table 15. FEMU results of the five analyzed Fiber Push-Out areas. [109]

Test Area	Experimental Sink-in(nm)	Chemical Shrinkage (ε_0^{chem}, 100% DOC)
Sample 3 Area 4	360	4.91%
Sample 3 Area 2	328	4.10%
Sample 3 Area 1	319	3.68%
Sample 4 Area 2	260	3.24%
Sample 4 Area 1	300	3.43%
	Mean	**3.87%**
	Standard Deviation	0.66%
	Coefficient of Variation	**17.1%**

Applying the average chemical shrinkage ε_0^{chem} from the FEMU results, the matrix sink-in is predicted for other fiber push-out areas. Table 16 compares FEM sink-in predictions with experimental measurements. Large discrepancy between numerical predictions and experimental results might be due to the matrix damage which was not considered in the current FE models. For instance, for Sample 5 Area 3 and Sample 2 Area 3 that show little matrix damage, experimental matrix sink-in is close to FEM-predicted matrix sink-in. For experiments with significant visible damage (Sample 5 Area 1, Sample 2 Area 4, Sample 2 Area 5), experimental measurements are much higher than FEM predictions. Figure 28 shows a push-out area with significant visible matrix damage.

Table 16. Matrix sink-in at other fiber push-out areas with application of FEMU result. [109]

Test Area	Visible matrix damage?	FEM-predicted Sink-in(nm)	Experimental Sink-in(nm)	Difference
Sample 5 Area 1	Yes	257	530	106%
Sample 5 Area 2	**No**	**258**	**144**	**-44%**
Sample 5 Area 3	**No**	**178**	**131**	**-26%**
Sample 2 Area 3	**No**	**299**	**351**	**17%**
Sample 2 Area 4 p1	Yes	120	390	225%
Sample 2 Area 4 p2	Yes	152	340	124%
Sample 2 Area 5	Yes	62	345	456%

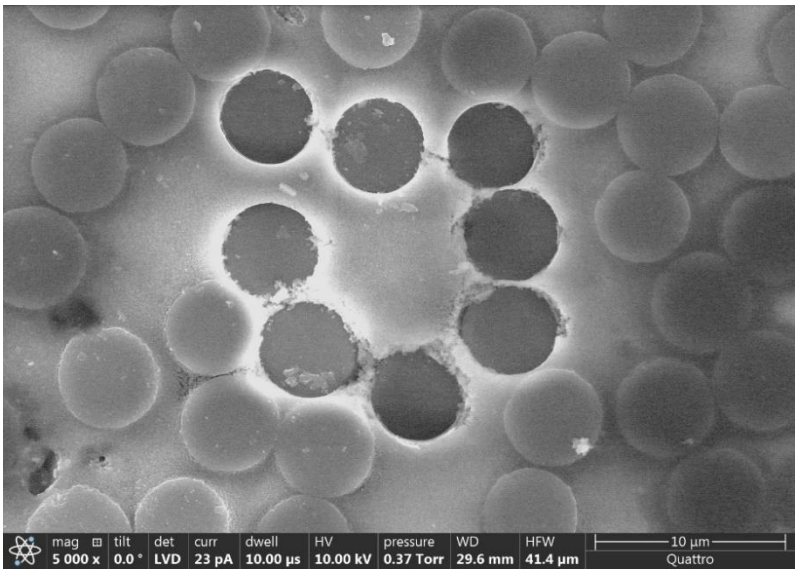

Figure 28. SEM image shows significant matrix damage on the Sample 5 Area 1.

Additional factors were identified as potentially contributing to the significant discrepancy between numerical predictions and experimental measurements. For example, Ghaffari et al. experimentally demonstrated significant friction effects at the fiber-matrix interface, causing interfacial stress in the order of 25% of the interfacial shear strength [114]. High friction stress can introduce significant residual stress to the nearby matrix and modify the stress distribution. This effect was not considered in the above-presented FEM results with a free-sliding interface after fiber push-out. The effects of the surface friction on the matrix sink-in measurement were confirmed in the parametric study presented in Section 4.5, which suggested that higher interface friction led to higher matrix sink-in. Local variance of material characteristics, including those due to voids and defects, is another possible factor causing errors, but it is difficult to verify these factors experimentally. The low matrix deformation sink-in measured on Sample 5 Area 2 might be due to the local material variance.

Studies using improved FE models that include some of these effects are being conducted to investigate these error-inducing factors.

Assessment of residual stress in composite [109]

In the referenced Sample 4 Area 1, after specimen grinding and before the fibers push out, residual stress is assessed and discussed.

Figure 29 presents the through-thickness direction normal stress (S_{zz}) in the matrix. Regions with high S_{zz} values are concentrated near the fibers, highlighting the interaction with stiff fibers that generates residual stress in the matrix. In the areas deep in the matrix-rich pockets and far from the fibers, the reduced blocking effect from the stiff fibers lowers the S_{zz}. In the current model, generated residual normal stress is very high. For a comparison, F3G manufacturer datasheet indicates a tension strength of $74.6\ MPa$.

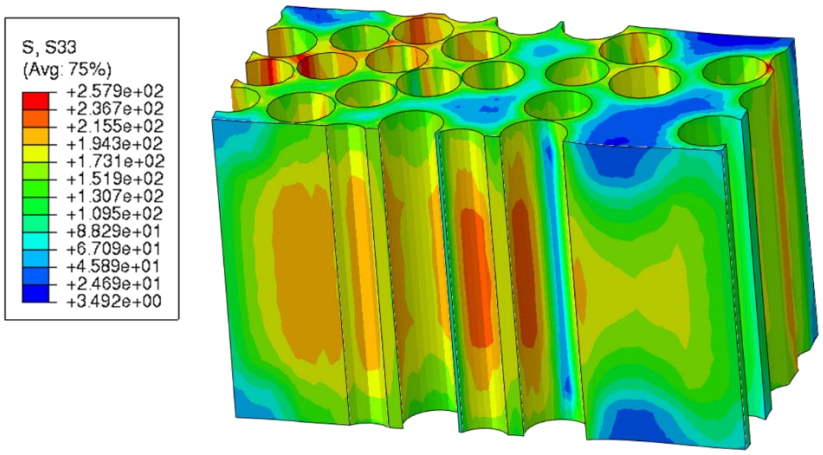

Figure 29. Before fiber push-out: normal stress S_{zz} in the through-thickness direction is shown for the matrix. [109]

Figure 30 presents the fiber-direction interfacial shear stress (S_{rz}) for the push-out fibers. S_{rz} provides an interesting comparison with the IFSS measurements using fiber push-out method due to having the same orientation. Mesh convergence was verified to produce a consistent location of the maximum S_{rz} in the FE model. On the reference model, this point is located at the Fiber ID 11 interface (Figure 30.a), facing towards a matrix-rich pocket (Figure 30.b). In Figure 30.c presents S_{rz} and the relative location along thickness for all interfacial nodes of Fiber 11. The "path of maximum S_{rz}" on the Fiber 11 interface crosses the point of maximum shear S_{rz} and runs along the membrane thickness. These results are plotted alongside the experimental IFSS of the HS40/F3G interface in both directions ($IFSS = 95MPa$, Ghaffari et al. [61]). The through-thickness symmetry of the FE model results in a symmetric through-thickness stress distribution. The zero S_{rz} at the mid-thickness gradually increases its magnitude towards the upper and lower surfaces and surpasses the IFSS at some locations. The high level

of interfacial shear stress developed is further emphasized in Figure 31, showing the S_{rz} higher than the IFSS in gray areas. In this FE model, mesh convergence on the interfacial shear stress distribution was verified. FE models of other push-out areas also produce high levels of interfacial stress.

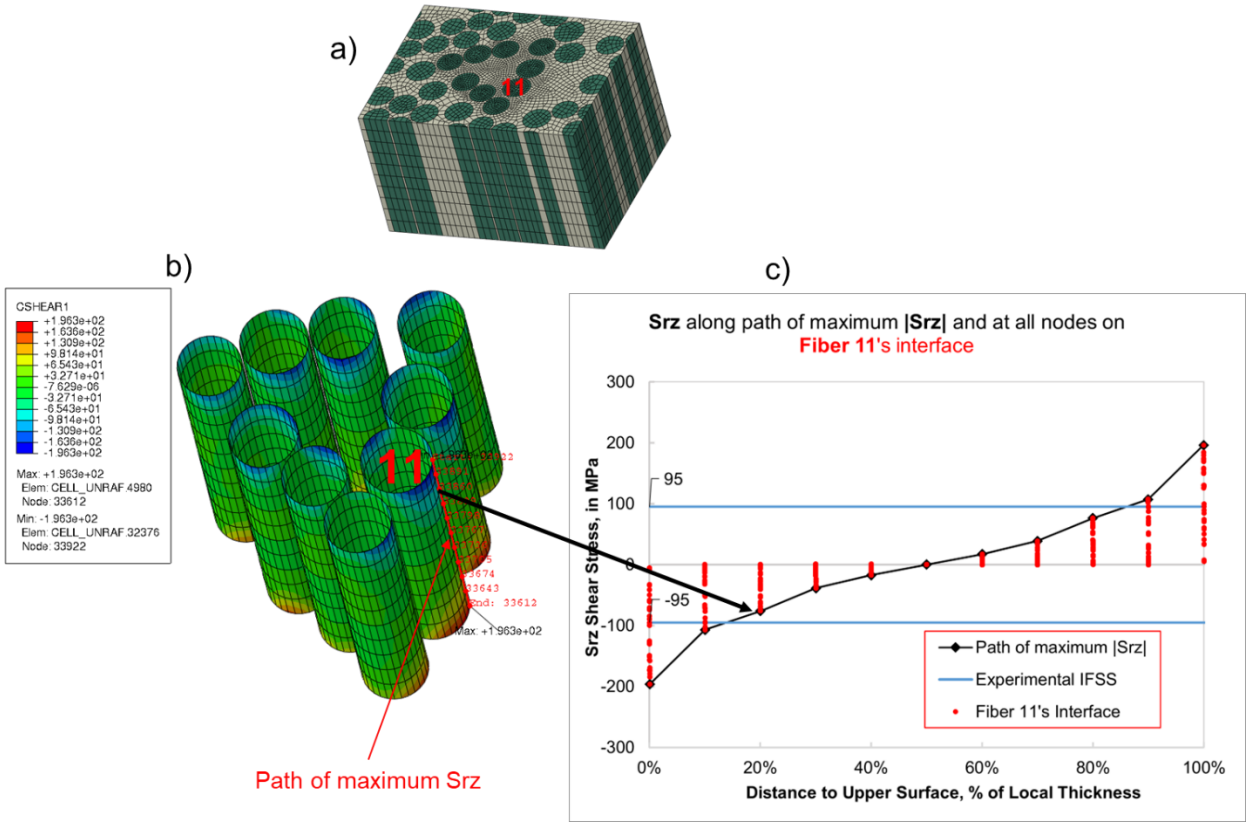

Figure 30. Reference Sample 4 Area 1 before Push-Out: a) Fiber ID 11 where the maximum S_{rz} is located; b) Path of maximum S_{rz} on Fiber 11 interface along thickness; c) Shear stress S_{rz} for all interfacial nodes of Fiber ID 11, plotted against experimental IFSS of HS40/F3G CFRP. [109]

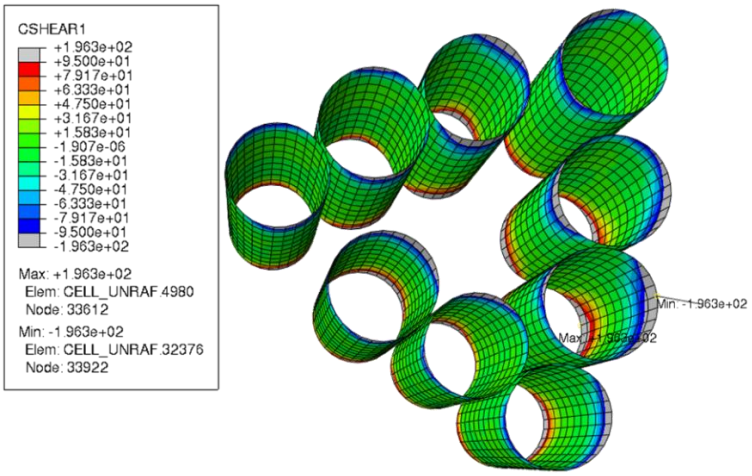

Figure 31. Interfacial shear stress S_{rz} for the push-out fibers. Gray areas indicate $|S_{rz}| > IFSS$. [109]

Figure 32 visualizes the radial axial shear stress S_{rz} in the matrix. The shear stress is presented in a cylindrical coordinate system positioned along the central axis Fiber ID 11. Gray color indicates areas where the matrix shear stress $|S_{rz}| > IFSS$. The residual shear stress is high and concentrates near membrane surfaces, strongly corresponding to the nearby interfacial shear stress distribution. These results illustrate the interfacial shear stress transfer into the matrix. Further from the fiber and into the matrix-rich area, matrix shear stress becomes lower.

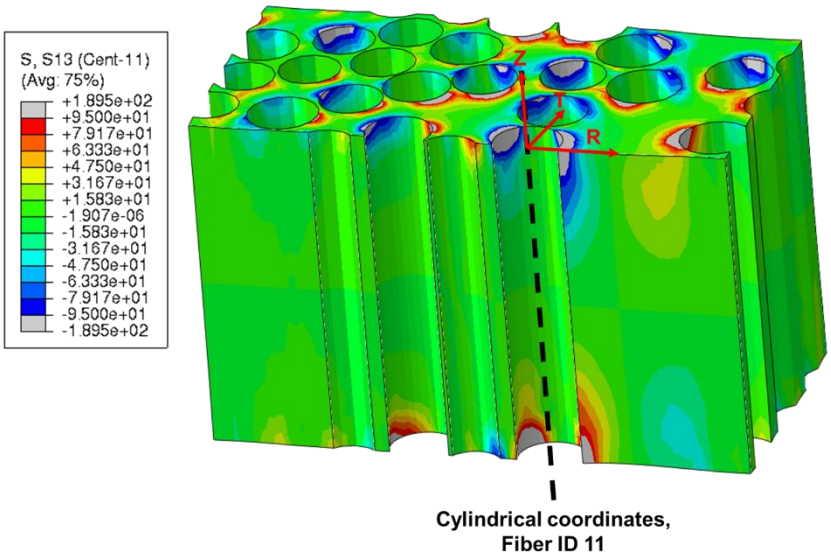

Figure 32. Residual shear stress S_{rz} in matrix before fiber push-out. The cylindrical coordinates system is positioned at Fiber ID 11 axis. Gray areas indicate $|S_{rz}| > IFSS$. [109]

High levels of residual stress in these FEM results suggest possible premature interface failure and matrix damage due to the curing and specimen manufacturing processes. However, no significant matrix or interface damage is visible in SEM images before the fiber push-out. This discrepancy might be due to the simplification of linear matrix material model with no plasticity/damage leading to an overly stiff model and too high residual stress generated. This simplification of linear material model also leads to a different stress distribution and consequently a different interfacial shear stress profile. For instance, matrix material might exhibit plastic yielding that lowers the overall stress level for a given strain.

4.5. Ongoing works and future improvements

Improving FE model for residual stress analysis using fiber push-out experiment

The FE geometry is created based on SEM images of the push-out specimens using the same process as previously described in Section 4.3. The improved FE model now represents the grooved support along with correct relative position of the fiber push-out area relative to the groove (Figure 33.a). The model now generates nine probes corresponding with the nine push-out fibers (Figure 33.a). The probes and supports (representing the grooved support) are modeled by analytical rigids according to experimental geometry descriptions.

Contact between the specimen and the support is modelled using the Hard and Frictionless surface-to-surface contact. This contact implements the General Contact algorithm which greatly helps with convergence, due to how Abaqus contact algorithm works. Each probe interacts only with its corresponding push-out fiber. Probe-fiber contact is similarly modeled with the Hard, Frictionless surface-to-surface contact.

The Embedded Area surrounding the push-out fibers has higher mesh density than the rest of the model (Unrefined Area, low mesh density) to capture properly and efficiently the evolution of interfacial damage during the fiber push-out process (Figure 33.b, c). The Embedded Area is bonded to the Unrefined Area using the Tied Contact formulation (Figure 33.c). Throughout the simulation, relative displacement at the tied contact interface between Embedded Area and Unrefined Area was monitored and verified to be insignificant, confirming the good “bonding” between the high mesh density and low mesh density volumes in the FE model.

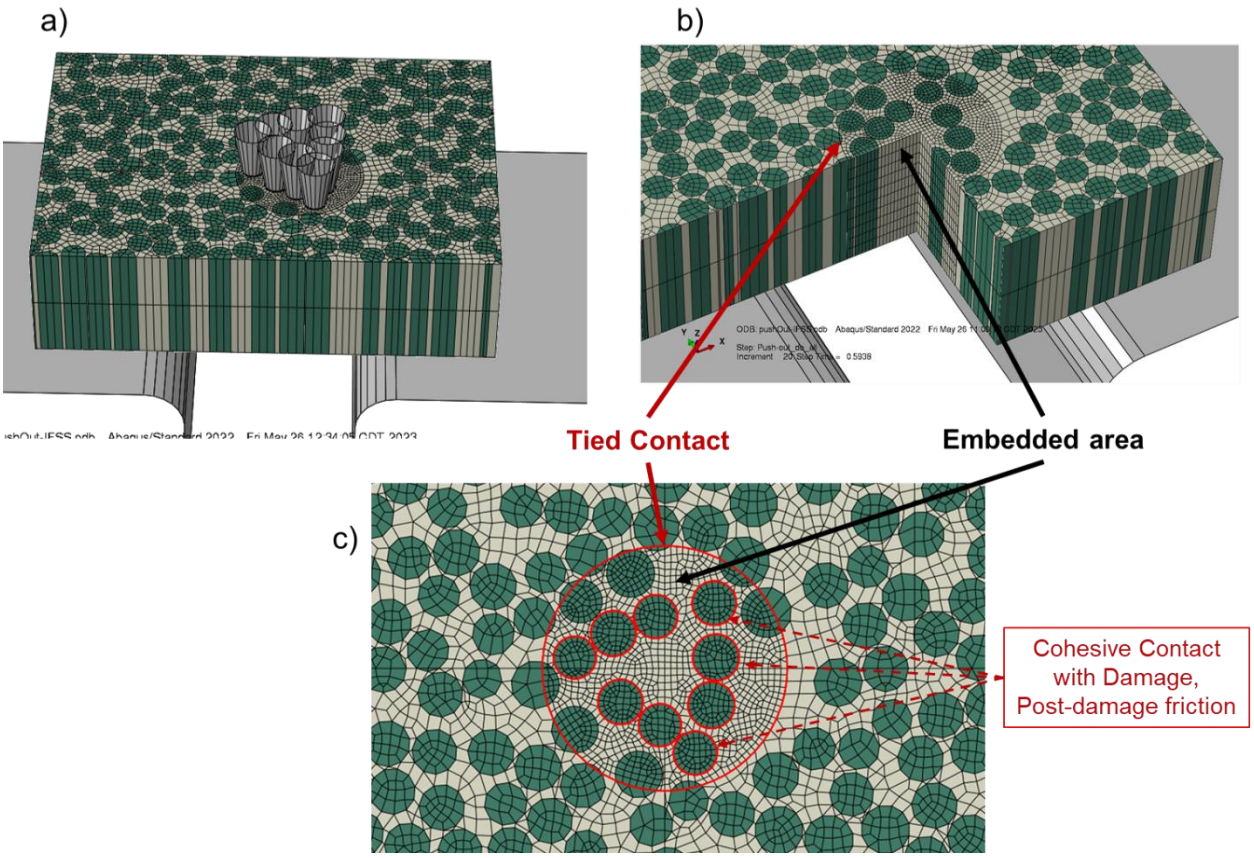

Figure 33. a) Improved FE model of the fiber push-out experiment, including the mount; b) Embedded area surrounding push-out fibers; c) Tied contact connecting embedded area with the rest of the FE model, push-out fiber-matrix interface modeled using Cohesive Contact with Damage.

The model size and mesh convergence analyses were performed, using the convergence of the matrix sink-in and the residual stress generated in probed matrix volume, similar to the convergence analysis of the legacy model (Appendix D,E).

The FEM simulation replicates the three processes: Curing, Grinding and Fiber Push-Out. At Curing, the analysis is performed using Abaqus Fully Coupled Temperature-Displacement solver. At Grinding and Fiber Push-Out, it is assumed that temperature changes and their effects are negligible, so the analysis is performed using Abaqus Static solver to save computational resources. Fiber and matrix are modeled using a mixture of C3D6T and C3D8T-type 3D elements.

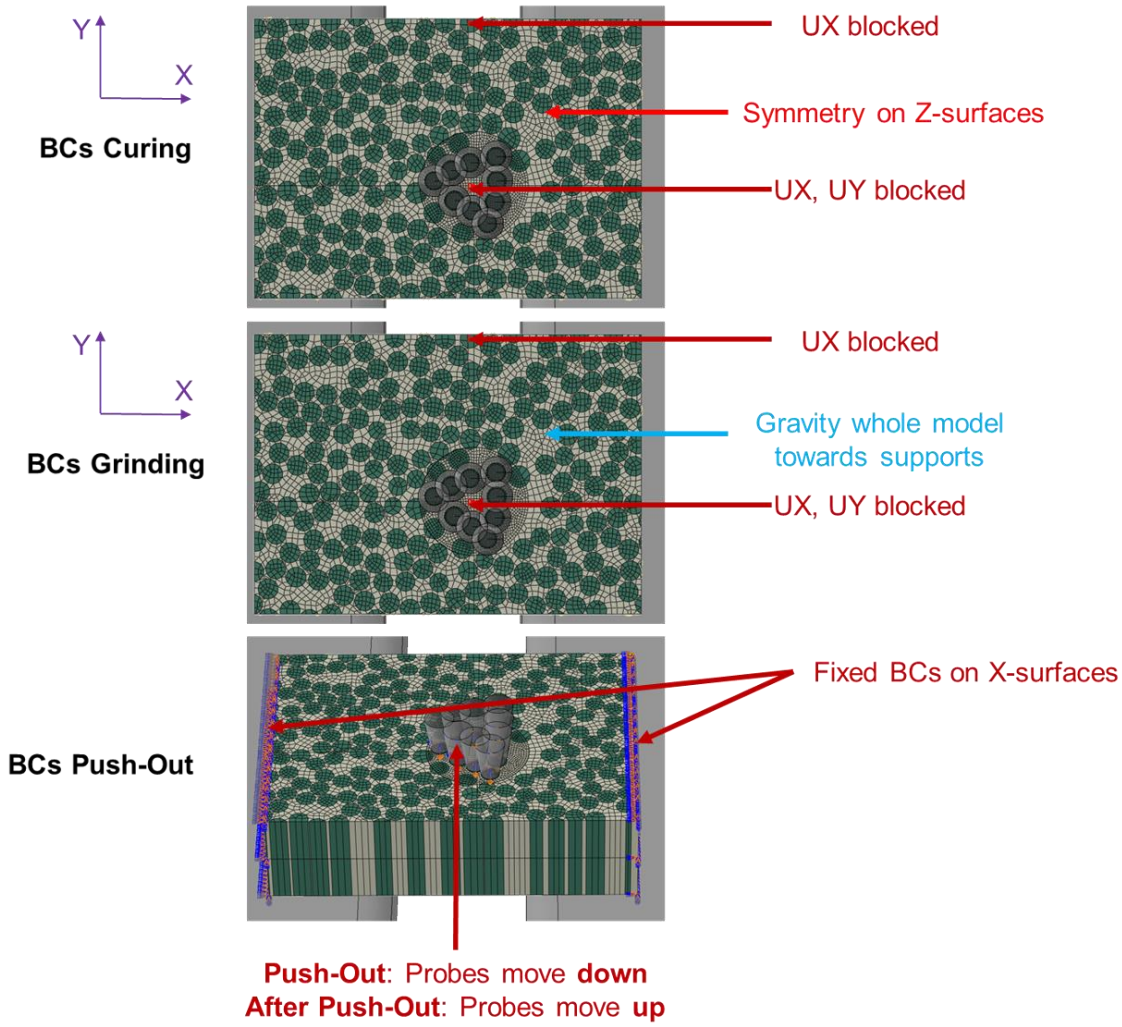

Figure 34. Illustration of Boundary Conditions at different processes of the simulation including Curing, Grinding and Fiber Push-Out.

Figure 34 illustrates the Boundary Conditions (BCs) at different stages of the simulation. At curing, symmetry BCs are applied on upper and lower membrane surfaces (Z-surfaces). F3G epoxy curing temperature profile is applied on the whole model. At Grinding, symmetry BCs are removed from the Z-surfaces.

To block FE model rigid body movements, at Curing and Grinding, a surface node at the center of Push-Out Fiber is blocked in UX and UY (in-plane directions), and a surface node at the upper edge is blocked in UX. During Grinding, a gravity load in direction of the support is applied to “attach” the specimen on the support. These BCs were verified such that no significant unrealistic reaction force is created in the FE model.

At Push-Out, the two sides of the membrane (X-surfaces) are fixed, to simulate the specimen taping and fixture on the support. The analytical rigid probes are moved down and up according to a pre-defined order by applying a vertical displacement.

Fiber and matrix material models of the HS40/F3G composite are similar to the legacy model. Epoxy matrix curing model applies the chemical shrinkage of $\varepsilon_0^{chem} = 3.43\%$ that was found for the reference Sample 4 Area 1 by the FEMU study.

The fiber-matrix interface is now modelled by the surface-to-surface cohesive contact with damage properties and post-damage friction behavior. Table 17 presents the reference fiber-matrix interface parameters of cohesive contact with damage model and post-failure friction. The Longitudinal Shear Strength IFSS was experimentally measured by Ghaffari et al. [61]. Other properties are estimated based on the literature reviews from Section 3. Regarding the practical implementation of the model, it is important to note that after a fiber is pushed out, complete interfacial failure is assumed (as verified by SEM observation) so the cohesive behaviors are removed, and the interface model *changes* into Finite Sliding. Consequently, the removal/moving up of the probes is modeled as a separate Step following the Fiber Push-Out where the probes are moved down. The Finite Sliding formulation allows realistic fiber-matrix contact tracking, but is incompatible with cohesive behaviors which allows only Small Sliding where the contact areas are not updated when relative movement at interface becomes significant. Figure 35 shows the FEM result after total interface failure with the COPEN result showing the contact area was properly updated. Fiber-matrix interface after total failure includes only the Hard Contact property that prevents penetration and the Friction property to model effects of friction stresses.

Table 17. HS40/F3G fiber-matrix interface reference properties.

Interface strength (MPa)	Normal	$Transversal\ Shear$	$Longitudinal\ Shear$
	75	95	95
Interface fracture energy (J/m^2)	Normal	$Transversal\ Shear$	$Longitudinal\ Shear$
	2	50	50
Interface friction	μ		
	0.1		

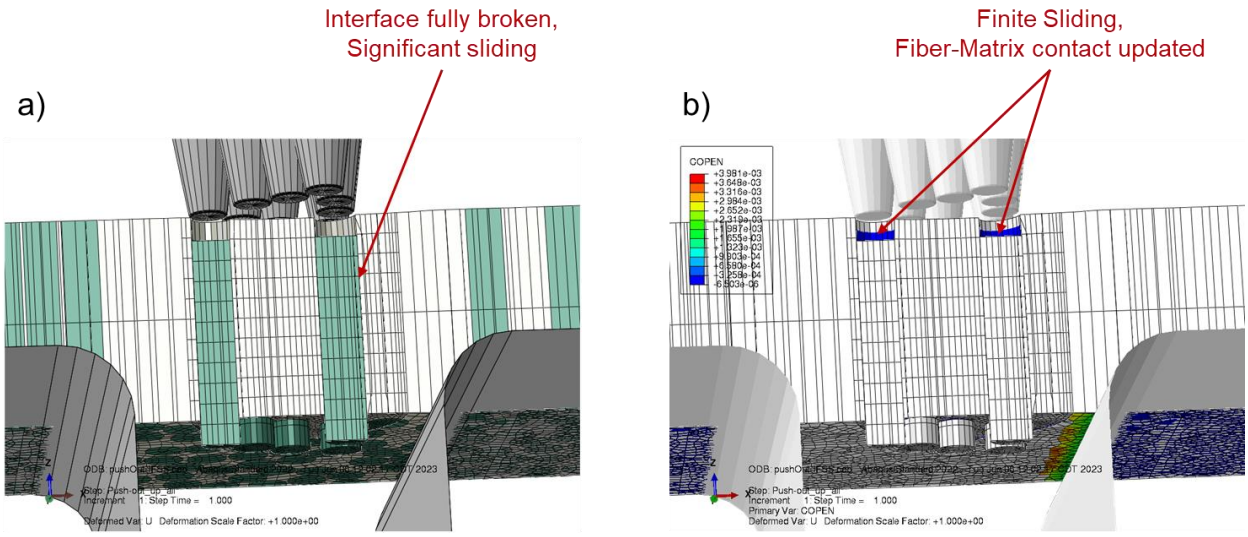

Figure 35. After fiber push-out and total interface failure: a) Visualization of significant relative displacement at interface; b) Finite Sliding formulation allows updating contact areas at interface.

Effects of post-failure friction stress on matrix sink-in deformation

The fiber-matrix friction stress was suspected to have significant effects on the matrix sink-in deformation due to the influences on the local residual stress distribution. To better understand this phenomenon, matrix sink-in on both the upper membrane surface (measured by the probed in the current fiber push-out setup) and the lower membrane surface (currently not measurable) are investigated in the FE model. Similar to the legacy model, upper surface Probed Nodes correspond to the matrix area where the real probe contacts the specimen. Lower surface Probed Nodes correspond to real probe diameter, but on the opposite, lower membrane surface. Figure 36 presents the positions of the Probes Nodes on upper and lower surfaces of the FE membrane model. The vertical coordinate of upper surface Probed Area is considered as that of the node with the *maximum* vertical (Z-) coordinate. Symmetrically, vertical coordinate of lower surface Probed Area is considered as that of the node with the *minimum* vertical (Z-) coordinate.

For the first part, the fiber push-out process utilizes the simplification that all fibers are pushed out at once (Synchronous fiber push-out).

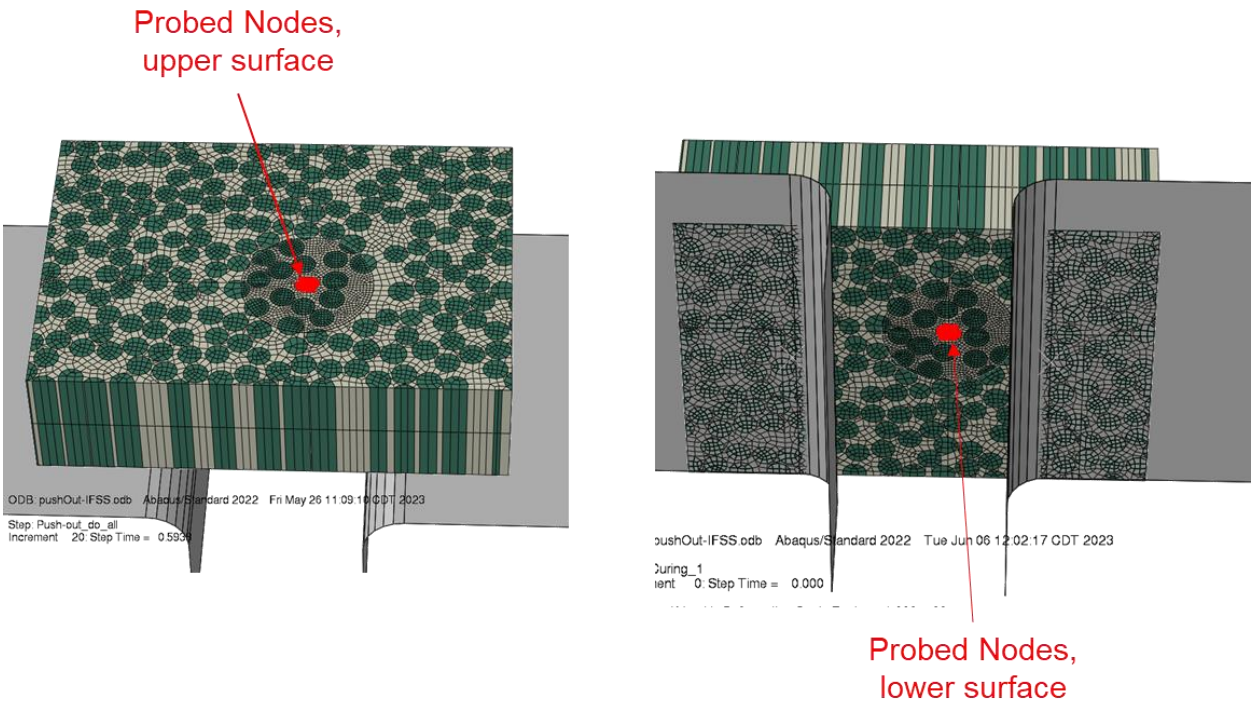

Figure 36. Probed Area with Probed Nodes on the upper and lower surfaces of the FE specimen model.

To evaluate effects of fiber-matrix interface friction on matrix sink-in, three (3) simulations with residual stress are performed with three values of interface friction coefficient:

- $\mu = 0.0001$: The interface is almost frictionless. The small value allows some simulation stability by preventing fiber rigid body movement after interface failure. Tangential interface stress was verified to be insignificant as intended.
- $\mu = 0.1$: The reference, estimated value for HS40/F3G.
- $\mu = 0.4$: The value estimated for IM7/8552 carbon/epoxy interface from Literature [60].

FE simulation results suggest that the sink-in deformation at upper and lower surfaces is asymmetric, which is clearly visible on the result presented in Figure 37.a. Parametric study results presented in Figure 37.b suggest several patterns:

- Higher interface friction leads to *higher* matrix sink-in at the upper surface.
- Higher interface friction leads to *lower* matrix sink-in at the lower surface.

- Consequently, higher interface friction leads to more pronounced upper-lower asymmetry of the sink-in deformation.

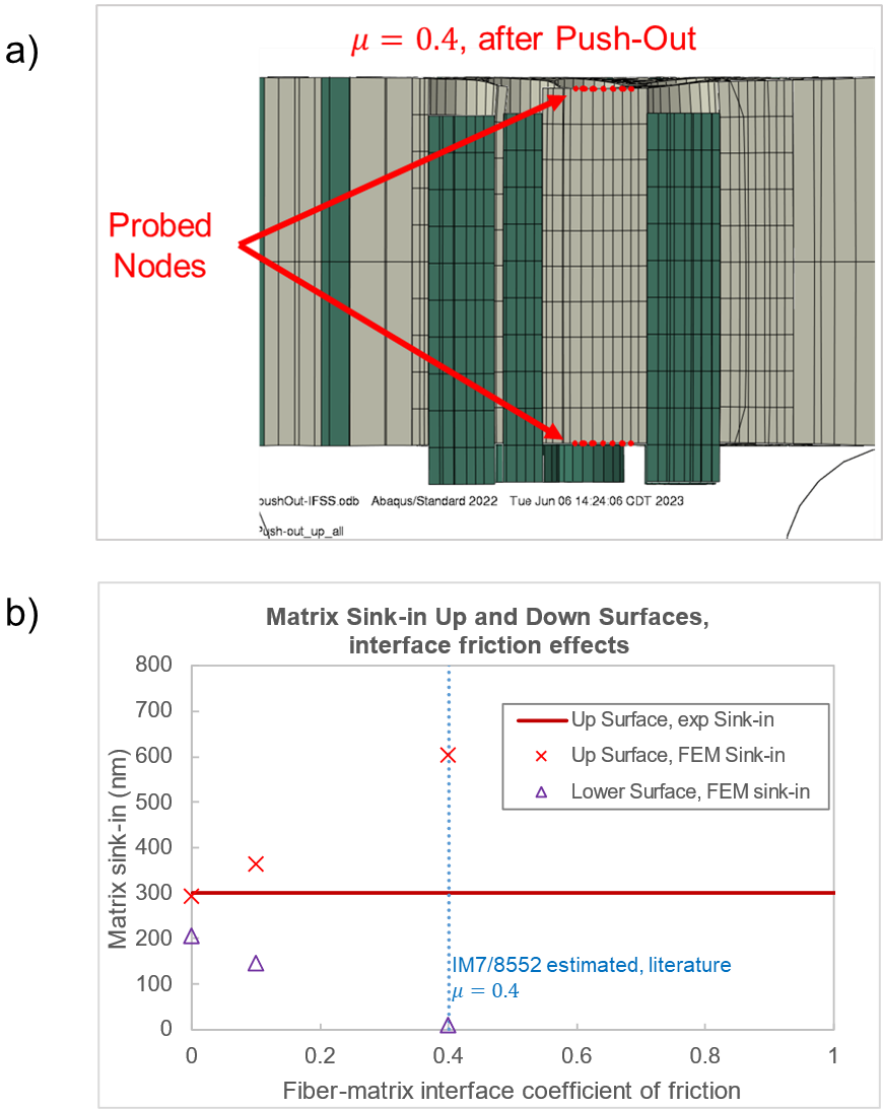

Figure 37. Matrix sink-in deformation after fiber push out experiment: a) Case of $\mu = 0.4$, the asymmetric matrix sink-in is clearly visible; b) Matrix sink-in, upper and lower membrane surfaces for different values of interface coefficient of friction.

Figure 38 presents FE simulation results on the combined effects of the epoxy matrix chemical shrinkage and the interface friction on the matrix sink-in deformation of the upper surface (corresponding to the matrix sink-in measured experimentally by the nanoindenter). A series of simulations with an alternate epoxy chemical shrinkage value of $\varepsilon_0^{chem} = 1.7\%$ were performed. These results suggest several patterns:

- For the same interface friction coefficient μ, higher chemical shrinkage ε_0^{chem} leads to higher matrix sink-in.
- For the same chemical shrinkage ε_0^{chem}, higher friction leads to higher matrix sink-in μ.
- As a result of the combined effects, different values of the couple $(\mu, \varepsilon_0^{chem})$ can produce the same matrix sink-in. For example, in the results presented in Figure 38, both the values $(\mu, \varepsilon_0^{chem}) = (0, 3.4\%)$ and $(\mu, \varepsilon_0^{chem}) = (0.4, 1.7\%)$ produce matrix sink-in similar to the experimental value.

These results suggest that due to the coupling effect, the matrix sink-in measurement alone is not sufficient to determine *both* the residual stress level and interface friction properties.

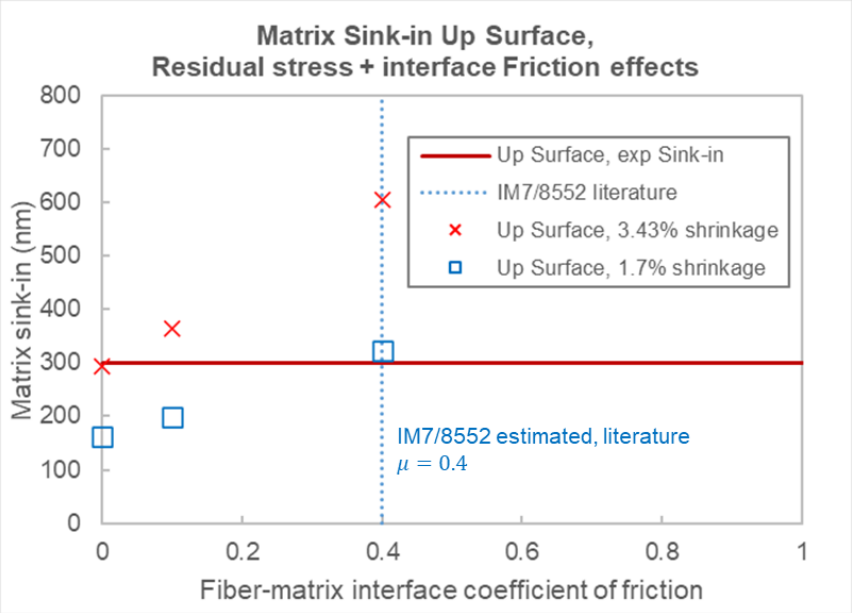

Figure 38. Combined effects of epoxy curing shrinkage and fiber-matrix interface friction on the matrix sink-in deformation.

Since the matrix sink-in deformation is created following the irreversible destruction of the push-out fibers interface, history effects might have strong effects on the precise matrix sink-in value. In this second part, the simplification of Synchronous fiber push-out is removed. Instead, the fibers are pushed out one-by-one, following the same order as in the corresponding experiment (Ordered fiber push-out). Figure 39.a

presents the fiber push-out order that was done experimentally and was replicated in the FE simulation.

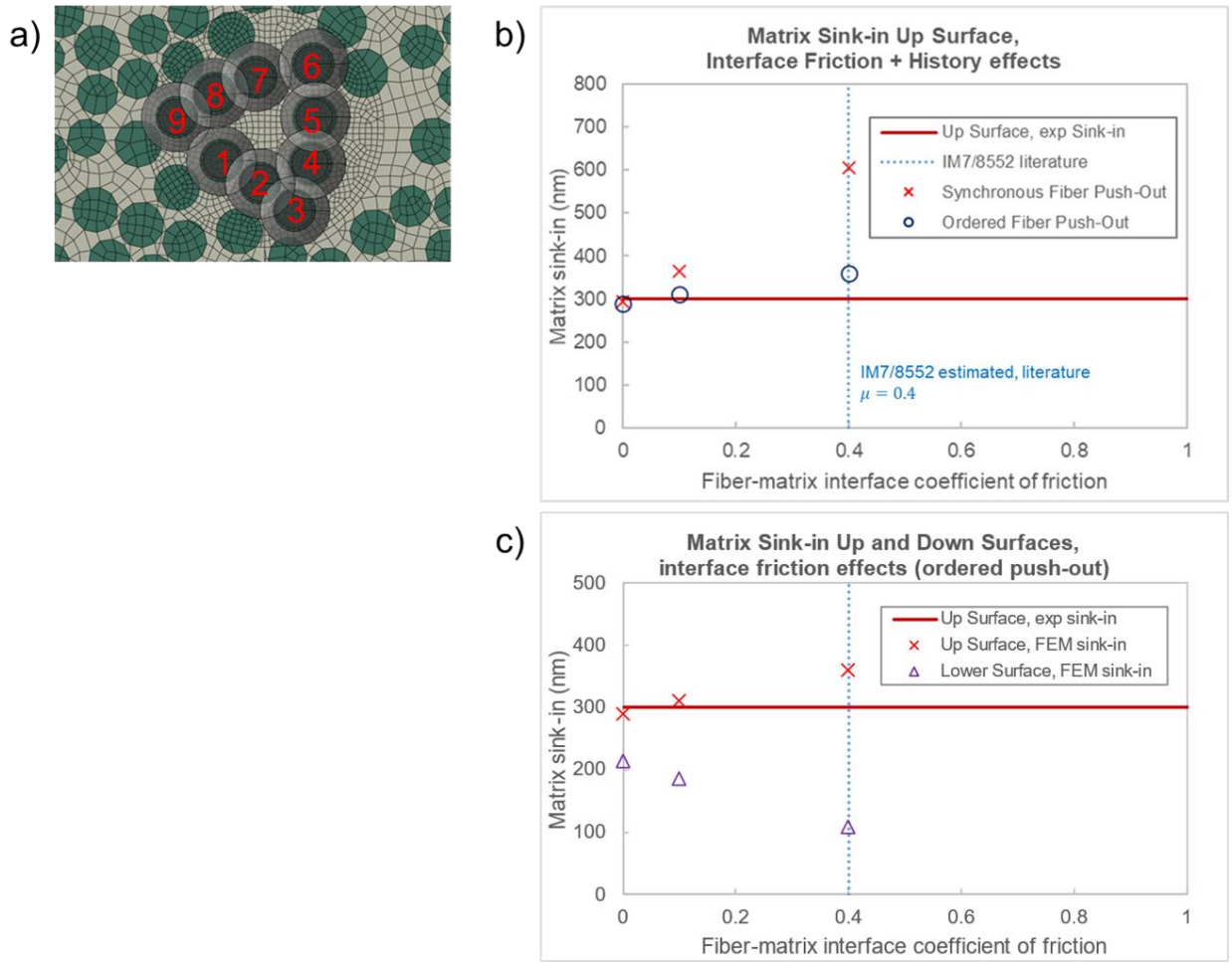

Figure 39. a) Order of the fibers to be pushed out one-by-one in the FE simulation, replicating the corresponding experiment; b) Top surface: sink-in values from simulations with Ordered fiber push-out, compared with the simplified Synchronous fiber push-out; c) Ordered push-out: matrix sink-in, top and bottom membrane surfaces for different values of interface coefficient of friction.

Figure 39.b presents and compares matrix sink-in deformation between Synchronous fiber push-out simulations and Ordered fiber push-out simulations at different interface friction coefficients. Figure 39.c presents matrix sink-in at top and bottom surfaces in the Ordered push-out simulation. Some important remarks from these results are:

- In the Order fiber push-out models, the same tendencies as in the simplified Synchronous fiber push-out models are observed: higher friction leads to higher matrix sink-in. However these effects are significantly weaker. This can be explained

by the fact that interface static friction stress at an already pushed-out fiber interface is modified when nearby fibers are pushed-out which induces local matrix deformation.

- Notably, in the case of frictionless post-failure interface, the two models of fiber push-out order produce the same sink-in result. This might be due to the fully linear material models and zero interface friction leading to zero history effect. Consequently, history effect even without interface friction might still be significant if matrix plasticity properties are included in the model.

- Overall, history effect is very significant in the analysis of fiber push-out experiment. The history effect might be even more pronounced when coupling with other irreversible effects such as matrix damage.

- Effects from friction in the Ordered push-out simulation is lower than in the Synchronous push-out simulation, probably due to the stress relaxation due to membrane being bent and relaxed each time a fiber is pushed out. However, the general tendency, including the asymmetric top-bottom deformation, is still significant (Figure 39.c).

The above remarks imply that proper modeling of history effects is very important for the accurate analysis of the fiber push-out experiment, including the analysis for the residual stress evaluation.

Effects of matrix plasticity and damage on post-push-out matrix deformation

Numerical models without significant interface friction and matrix plasticity effects predict matrix sink-in at both the top and bottom surfaces of the membrane. However, permanent deformation of the matrix that develops during the push-out experiment has potentially significant effects on the matrix deformation in the push-out area. To verify this, the Research Team at AMSL conducted the fiber push-out experiment on the IM7/8552 carbon/epoxy specimen and measured the matrix in-plane deformation at both the top and bottom surfaces of the central matrix pocket. The bottom surface was

found to protrude instead of sink-in (Figure 40). Due to the strong fiber-matrix interface of the IM7/8552 composite, very extensive matrix damage can be observed (Figure 40). These results suggest that effects from matrix plasticity and damage are significant, causing the experimental deformation to deviate significantly from the simplified model prediction.

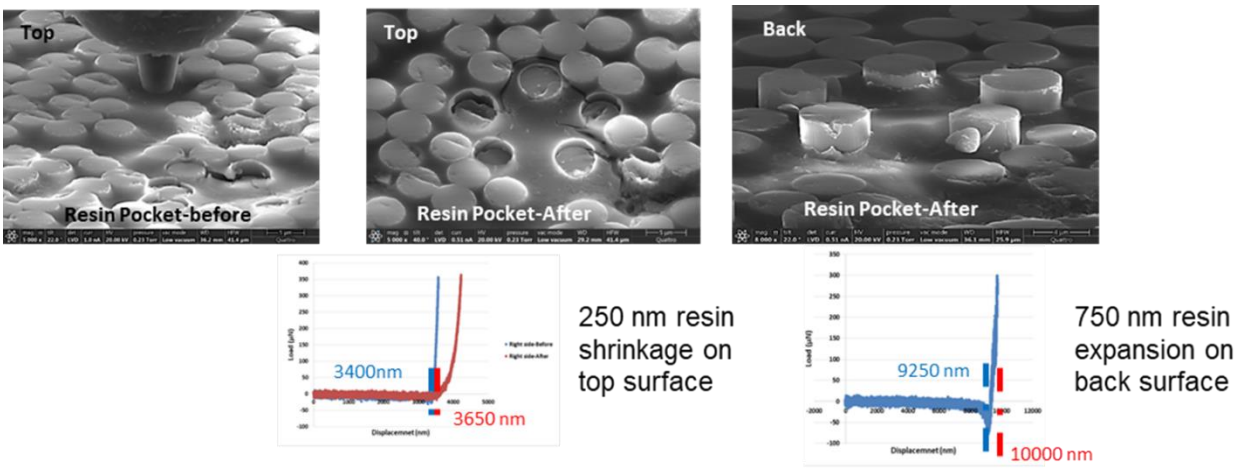

Figure 40. Fiber push-out experiment on IM7/8552 by the Research Team at AMSL/UTA. Out-of-plane deformations are measured on both the top and bottom/back surfaces.

Proposed improvements and future works

New epoxy material model with rate-form constitutive stress-strain relation

The FEM analysis presented in section 4.3 utilizes the Abaqus built-in linear elastic model for the epoxy matrix material. The stress-strain relation depends solely on the instantaneous matrix of stiffness:

$$\bar{\boldsymbol{\sigma}} = \overline{\overline{\boldsymbol{C}(\boldsymbol{\alpha}, \boldsymbol{T})}} : \bar{\boldsymbol{\varepsilon}}$$

Consequently, in the legacy model, precise evolution profile of the epoxy Modulus has insignificant effect on the resulting residual stress due to the absence of history effect. In addition, for a given value of final accumulated strain, stress becomes artificially too high.

For the next stage of model improvement, it is suggested that material constitutive model utilizes a rate-based formulation:

$$d\bar{\boldsymbol{\sigma}} = \overline{\overline{\boldsymbol{C}(\boldsymbol{\alpha}, \boldsymbol{T})}} : d\bar{\boldsymbol{\varepsilon}}$$

$$\bar{\boldsymbol{\sigma}}(\boldsymbol{t}) = \int_{gel\ point}^{t} \overline{\overline{\boldsymbol{C}(\boldsymbol{\alpha}, \boldsymbol{T})}} : d\bar{\boldsymbol{\varepsilon}}$$

The “hypoelastic” formulation should be able to better describe the residual stress accumulation during the epoxy curing process. The same approach was taken by Goncalves et al. [115]. In the Abaqus 2023 version, built-in material models of hypoelasticity and curing are incompatible. The usage of user subroutine for customized material models is therefore necessary.

Cave Configuration for improved Boundary Conditions determination in push-out experiment

The Boundary Conditions representing specimen fixture in the fiber push-out setup are simplified, assuming no extra in-plane stress due to the taping on the two sides of the membrane. This extra in-plane stress, if indeed present, effectively acts as additional residual stress, for which there is currently no method to determine precisely. In addition, the over-compliance of the membrane due to the imperfect and difficult-to-characterize contact between the specimen and the mount might introduce other issues to a model with strong history effects. This over-compliance effect would be presented with more details in Chapter 5.

To improve the Boundary Conditions determination, the “Cave Configuration” that was employed by Ghaffari et al. **[61]** provides a strong improvement. Figure 41 provides an illustration of the specimen in Cave Configuration where the unremoved material above the “cave” becomes the membrane for the fiber push-out experiment. Under this configuration, the above-mentioned problems regarding boundary conditions can be effectively eliminated.

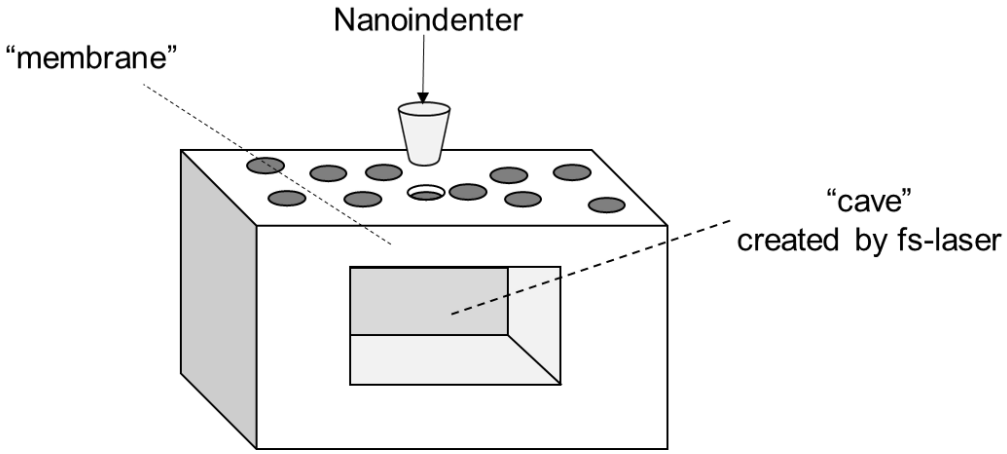

Figure 41. Cave Configuration for Fiber Push-Out Experiment.

Application of DIC for experimental observation of post fiber push-out matrix deformation

The method of Digital Image Correlation (DIC) was applied by Winiarski et al. [108] in conjunction with their Microdrill method to characterize residual stress in homogenous materials. In this method, a microscale hole is “drilled” into the specimen using ion beams, leading to surface deformation around the hole due to relaxed residual stress in its surrounding. Before the material removal, micro particles have been randomly dispersed and coated on the specimen surface, providing features for the DIC processing which shows the local surface strain field due to the relaxed residual stress.

At the current stage of our experimental technique, it is difficult to apply the DIC technique to analyze surface deformation following the fiber push-out due to the lack of surface features. If microscale particles of appropriate size can be dispersed on specimen surface at appropriate density and patterns, the same DIC processing technique and algorithm can be applied to analyze in-plane strains resulting from relaxed residual stress due to fiber push-out. The ability to characterize relaxed stress-induced in-plane strain would provide more data for material characterization in addition to the matrix sink-in measurement. Figure 42 presents the displacement vectors on the matrix upper surface nodes before (Figure 42.b) and after (Figure 42.c) the push-out of one single fiber in the FEM simulation, the difference being the relative surface displacements between the two states. An in-plane strain field can be deduced from

these FEM-computed displacement results and compared with experimental DIC strain measurements for the purpose of inverse characterization of material properties.

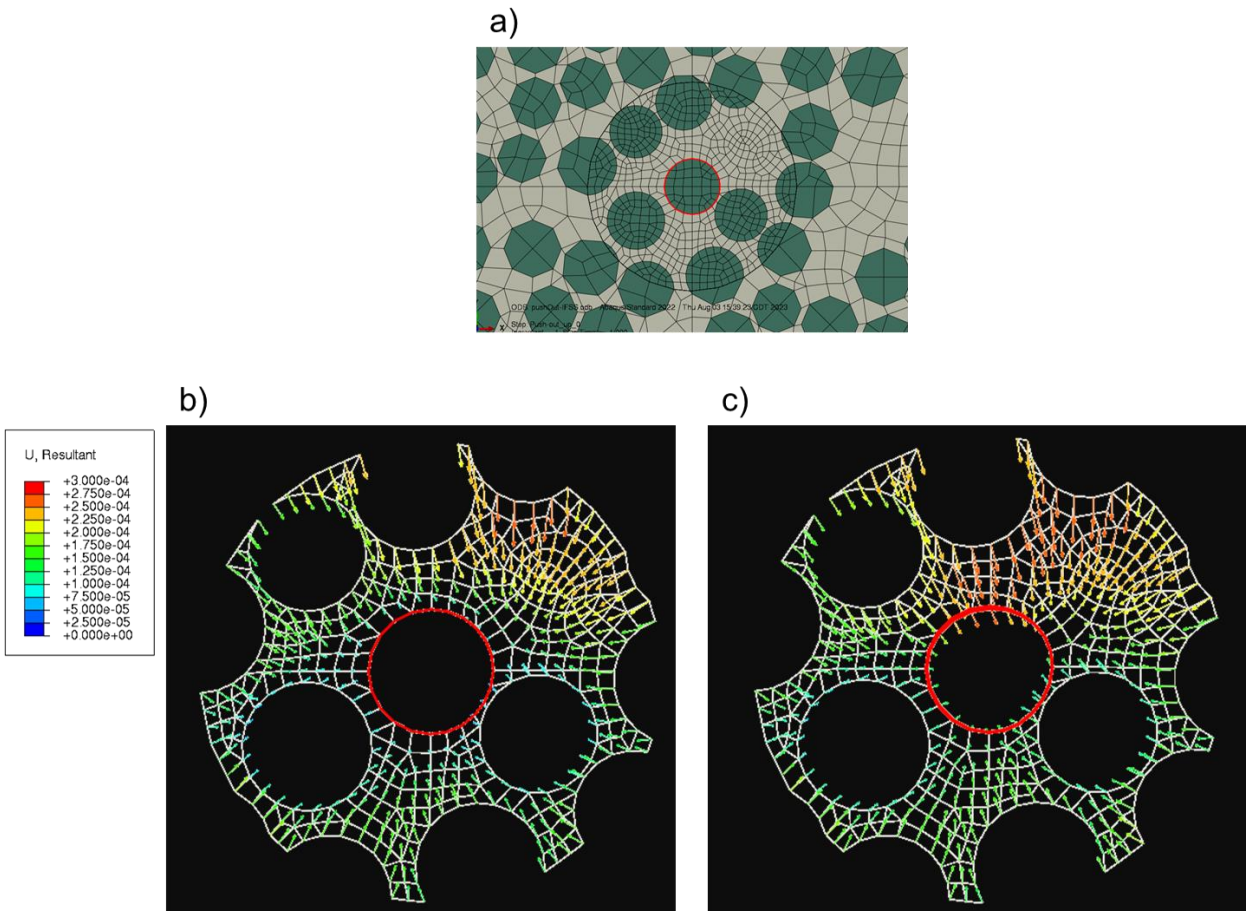

Figure 42. a) The push-out fiber at the center of the embedded mesh area, highlighted in red; displacement vectors at the upper matrix surface: b) Before the fiber pushout; c) After the fiber push-out.

In addition to the obvious benefit of providing more data, the application of DIC for the analysis of in-plane matrix strain in the Push-Out method for residual stress also offers several advantages:

- Strains in a Cartesian coordinates system are displacement-independent. Thus, strains can be analyzed independently from the absolute position of the specimen. As a result, any problem with the fixture becomes much less of an issue. For comparison, in the sink-in measurement, specimen position must be precisely fixed during the test. The DIC method therefore allows a much more robust measurement.
- Just one fiber needs to be pushed out for the relaxed strain to be observed, as shown in Figure 42. As a result, history effect is much less pronounced than the

sink-in measurement. This includes effects from existing damage from nearby, previously pushed out fibers.

- Friction stress development can also be much better described thanks to the lack of multiple deformation cycles from other nearby fiber push-outs which were demonstrated to relax and modify the existing static friction stress.

- This analysis technique potentially allows a much higher number of observations per each membrane specimen thanks to the fact that just one fiber needs to be pushed out. For comparison, the existing sink-in evaluation technique requires that fibers surrounding one resin-rich pocket to be pushed out, and suitable matrix-rich areas can be difficult to find and few in number.

Meanwhile, the proposed technique also possesses several disadvantages:

- Potential difficulty in dispersing micro particles at random patterns and appropriate density (for useful spatial resolution) on the microscale specimen surface [116].

- Potential error and difficulty due to the distortion effects characteristic of SEM systems [117]. The application of any macroscale DIC technique (for example, the successful applications by Seon et al. [118], [119]) to microscale strain measurements must take into account these interfering factors.

4.6. Conclusions

A new method was proposed to evaluate the microscale residual stress in carbon/epoxy composites. The method is based on the fiber push-out experiment and analysis of the post-push-out matrix deformation using Finite Element Modeling. Initial models predict very high levels of residual stress, which are even higher than material strengths, indicating a very significant overestimation. Several potential sources of errors have been identified that significantly affect matrix deformation at the push-out area, including effects from matrix plasticity and damage with experiments by the

AMSL/UTA Research Team, and post-failure friction at the interface by numerical analysis, which had not been considered in the initial numerical models.

From experimental data and numerical analyses, it can be deduced that matrix deformation at the push-out area is likely a combination of many effects that include residual stress relaxation, matrix plasticity and damage, post-failure interface friction. As a result, residual stress in the real specimen should be significantly lower than the initial model prediction.

To improve the reliability of the method, several improvement strategies have been suggested. The use of user subroutine for custom material model is recommended, so that complex material behaviors of the epoxy matrix including the Modulus development during curing, and plasticity and damage behaviors during push-out, can be captured properly. The Cave Configuration proposed by the AMSL/UTA Research Team is suggested as the preferred configuration for the residual stress analysis with fiber push-out method, as it allows much more precise determination of the Boundary Conditions which might have strong effects on the residual stress in the test area. The application of the DIC technique is recommended for observation of post push-out in-plane matrix deformation, as it provides extra data for FE analysis, potentially more robust measurements, and potentially allowing higher number of experimental observations per specimen.

CHAPTER 5

FEM evaluation of the IFSS measurement using Fiber Push-out method and effects from microscale properties including residual stress

5.1. Introduction

Preliminary FEM analysis on the UD composites suggested the strong impact of fiber-matrix interfacial strength on the fiber-direction compression strength (Section 2.3). This relation is also reported by other authors [15], [22], [23]. Therefore, precise measurement of the IFSS is an essential input for composite strength modeling. Fiber Push-Out method is a popular technique for IFSS measurement. In a fiber push-out experiment, a nanoindenter pushes the fiber out of a thin membrane specimen in the through-thickness/fiber direction. Assuming the stress is uniformly distributed over the fiber-matrix interface, the IFSS is commonly calculated using the formula:

$$IFSS_{apparent} = \frac{P_{max}}{2\pi \times r \times t} \tag{9}$$

where P_{max} is the maximum Load registered at the nanoindenter, r is the fiber radius, t is the local membrane thickness. In this Chapter, $IFSS_{apparent}$ refers specifically to the IFSS value obtained through the ideal equation above. Figure 43 provides an illustration of the Fiber Push-Out experiment with important parameters.

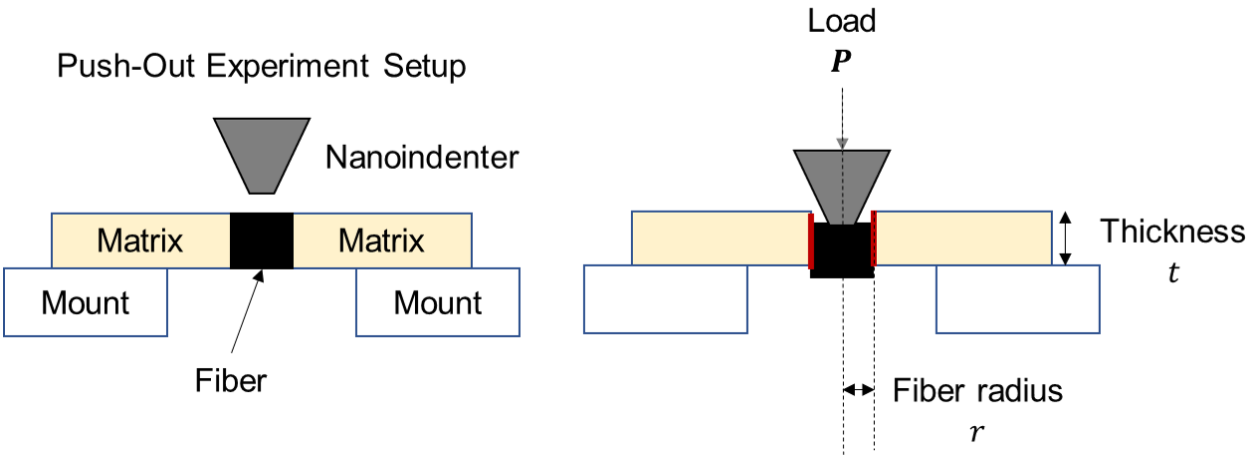

Figure 43. Schematic illustration of Fiber Push-out experiment for IFSS measurement.

Meanwhile, there exist many undesired effects interfering with the IFSS measurement using the ideal formula. Several authors pointed out the existence of non-linear plastic matrix deformation [61], [120], non-uniform interfacial stress distribution [121], elastic membrane bending [61], [83], all of which have the potential to introduce significant deviations to the ideal equation for IFSS calculation (9). In addition, analysis of the microscale residual stress in matrix demonstrated a high level of residual stress of the same order of magnitude as the experimentally measured apparent IFSS.

Due to the importance of IFSS in composite strength, the complexity and multitude of potentially interfering effects, it is concluded that the IFSS measurement using fiber push-out should be investigated and verified using FE modeling.

5.2. Methodology

The present study utilizes the FEM analysis to replicate and study the fiber push-out experiment for IFSS measurement. The FE geometry is reproduced as close as possible to the real corresponding specimen. Sensitivity analyses on different material parameters including interface properties, matrix properties and residual stress are performed to study their influence on the IFSS measurement. FEM-computed Load-Displacement curves at the nanoindenter are compared with corresponding experimental to identify drawbacks of the FE model, and to propose improvements to both the FE modeling and the experimental setup.

5.3. Finite Element Model

The FEM simulation models the push-out of the first fiber at the Sample 4 Area 1. The push-out of only the first fiber is modeled to avoid the complex interferences from history effects including matrix and interface damage due to the previous push-out of nearby fibers. Figure 44 presents the Embedded Area surrounding the push-out fiber and the FE contact surfaces. The features of the FE model for the IFSS study are overall similar to the FE model of the fiber push-out experiment for residual stress

analysis. However, there are several differences to optimize the analysis of a single fiber push-out for IFSS measurement.

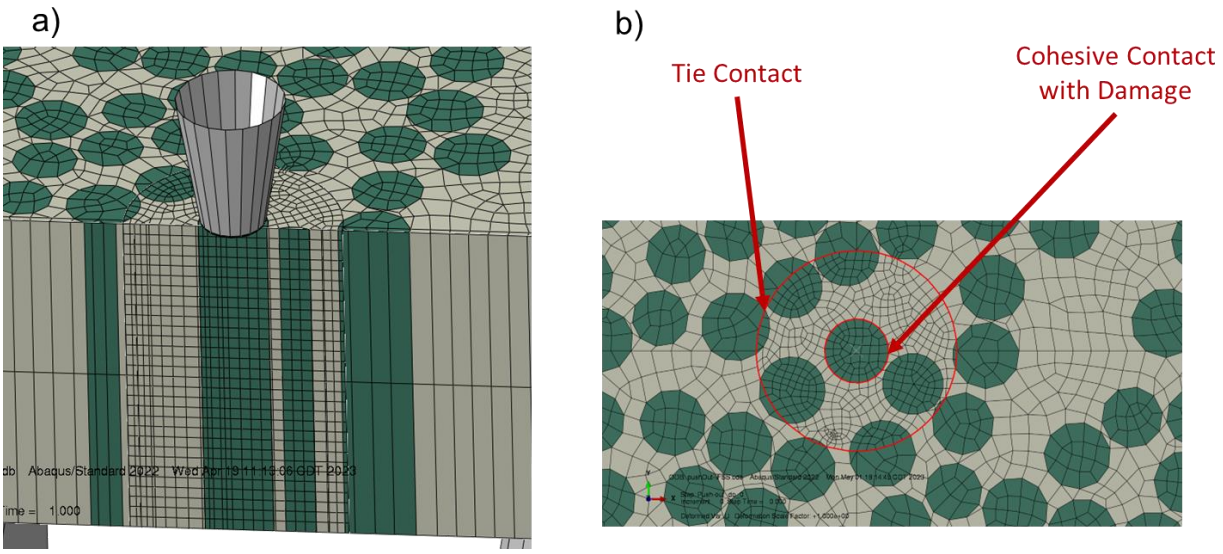

Figure 44. a) Embedded Area surrounding the Push-Out Fiber; b) Tied Contact connecting Embedded Area with the unrefined part.

Mesh density and model size are different from FE model for residual stress analysis due to the emphasis on the IFSS analysis and the importance of modeling the gradual interface failure. In this study, mesh and size convergences were verified such that:

- A significant increase in mesh density leads to insignificant change of the Load-Displacement curve measured at the probe.
- At reference configuration, damage variable CSDMG at fiber-matrix interface is verified such that the transition from 0.01 (almost pristine) to 0.99 (almost fully damaged) occurs over *at least three surface elements along thickness*. In most cases, this transition occurs over much more than three surface elements. In extreme cases of parametric study with low interface fracture energy, this condition was also verified.

The reference material models are the same as the FE model for residual stress analysis. However, this IFSS analysis also study effects from matrix non-linear plastic behavior. The matrix plasticity is modeled using the Abaqus built-in Concrete Damage Plasticity. For these sensitivity studies, the reference matrix plasticity properties are

presented in Table 18. Concrete Damaged Plasticity properties ($\Psi, \epsilon, \sigma_{b0}/\sigma_{c0}, K_c$, μ) are assumed to be the same as the 8552 epoxy. Tensile yield is provided in F3G datasheet. Compression yield is estimated assuming the same ratio tension/compression yield stress as 8552. Fracture Energy is typical for thermoset epoxies.

The fiber-matrix interface is modeled using the Abaqus built-in Surface-to-Surface Contact formulation with Cohesive Contact, Damage Behavior. Reference HS40/F3G interface damage properties implemented in the analyses are presented in Table 19. The longitudinal IFSS is provided by the reference [61]. Other values are estimated.

Table 18. F3G reference plasticity properties

Concrete Damaged Plasticity	Ψ	ϵ	σ_{b0}/σ_{c0}	K_c	μ
	29	0.1	1.29	1	1E-5
Yield Stress	Tensile (MPa)	Compressive (MPa)			
	74.6	108.5			
Fracture Energy	Mode I (J/m^2)				
	100				

Table 19. HS40/F3G interface properties

Damage Initiation	IFNS (MPa)	IFSS, transversal (MPa)	IFSS, longitudinal (MPa)
	75	95	95
Damage Evolution	G_I (N/m)	G_{II} (N/m)	G_{III} (N/m)
	2	50	50
Benzeggagh-Kenane parameter	η^{BK}		
	1.45		

5.4. Results and discussion

The FEM simulations replicate the IFSS measurement using fiber push-out free-standing setup. In the results presented in this Section, “Ideal max Load” refers to the value:

$$F_{max} = IFSS^{exp} \times 2\pi \times r \times t \quad (10)$$

where $IFSS^{exp}$ is the experimental IFSS, and used as the interfacial strength input for the FE model. r is the fiber radius. t is the membrane thickness. Thus, F_{max}

refers to the ideal maximum Load measured by the indenter assuming uniform interfacial shear stress at the moment of failure.

Similarly, “apparent IFSS” refers to:

$$IFSS_{apparent} = \frac{P_{max}}{2\pi \times r \times t} \quad (11)$$

where P_{max} is the maximum Load registered by the FEM nanoindenter. Thus, $IFSS_{apparent}$ refers to the IFSS measured in the virtual fiber push-out experiment.

Strong interaction and coupling between different material properties and effects during the fiber push-out experiment

As many parameters are estimated due to the lack of data (and in some cases, total lack of experimental method for characterizing), a preliminary series of sensitivity study is performed, aiming to give a *qualitative assessment* of the complex interaction between different phenomena (such as matrix yield, interface damage, post-damage friction) and their effects on the Load-Displacement Curve.

There is no Curing simulation in these studies. Thus, there is **no residual stress** before Push-Out. In these studies, reference F3G matrix model includes Concrete Damaged Plasticity behaviors. Reference interface model utilizes the properties presented in table 19, where input IFSS is equal to the experimental IFSS.

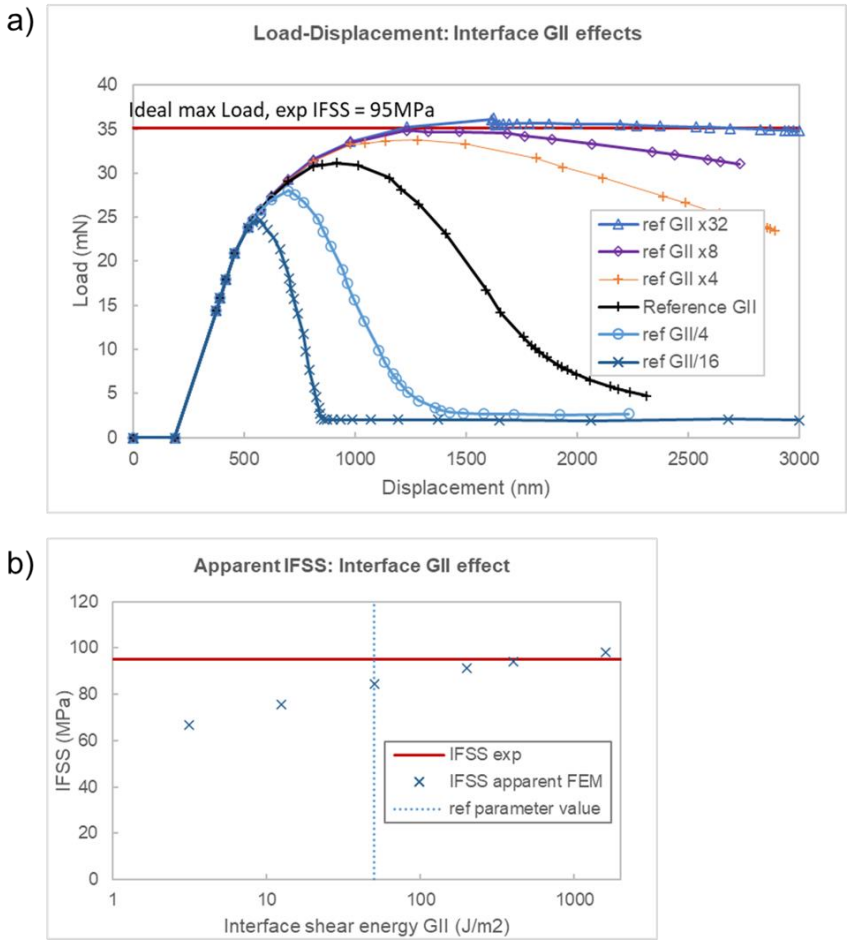

Figure 45. Effects of GII: a) Load-Displacement curve at probe; b) Apparent IFSS.

Figure 45 presents effects of interface Longitudinal Shear Fracture Energy G_{II}. Several important remarks can be made:

- G_{II} has a very strong effect on the Load-Displacement curve.
- G_{II} has significant effects on Peak Load, especially at lower values of G_{II}. At high G_{II}, effects on Peak Load seems to “converge”.
- Literature review found no experimental method measuring longitudinal G_{II} as of 2020.

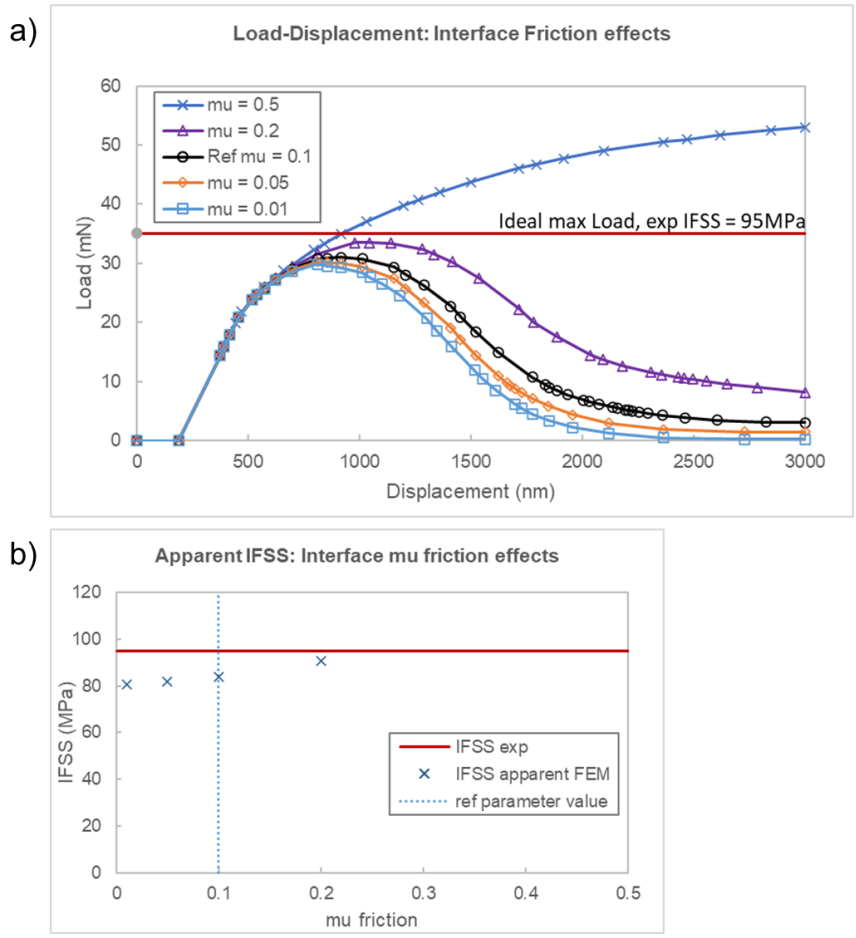

Figure 46. Effects of interface coefficient of friction μ: a) Load-Displacement curve at probe; b) Apparent IFSS.

Figure 46 presents effects of interface Friction Coefficient μ. Some important remarks can be made:

- μ has strong effects on Load-Displacement curve *and* Peak Load.
- Even without residual stress from curing, post-damage Load is non-zero due to the interfacial friction stress. The existence of friction stress is due to the permanent plastic deformation of the surrounding matrix which applies non-zero normal stress at the interface.
- At $\mu = 0.5$, load due to friction stress is unrealistically higher than Ideal max Load. For comparison, friction coefficient at the IM7/8552 carbon/epoxy interface is estimated at 0.4. This demonstrates the limitations of the current FE model.

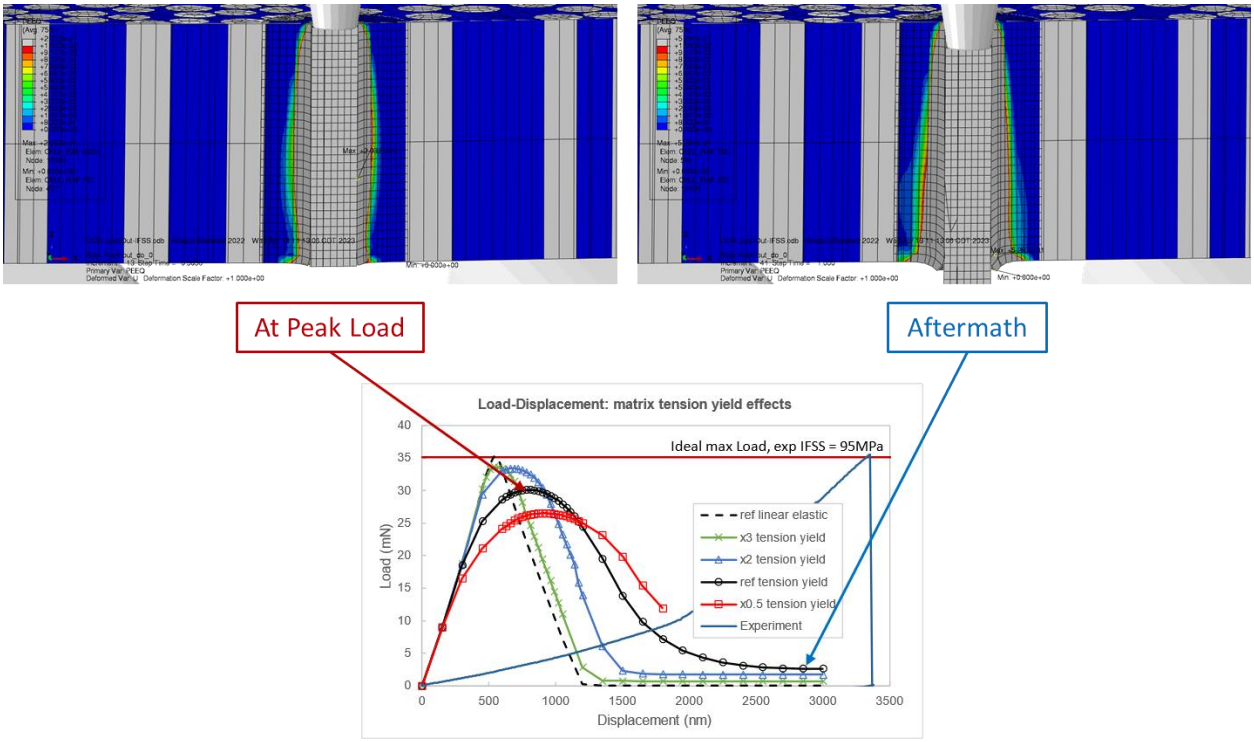

Figure 47. An example showing matrix plasticity damage at Peak Load and after the total interface failure. Matrix areas with $PEEQ > 1\%$ are colored in gray.

FE modeling has the useful advantage of allowing detailed observation of the damage evolution of the matrix throughout the virtual experiment. Figure 47 presents an example with two snapshots of the progress of matrix plastic deformation, at Peak Load and at the Aftermath where fiber-matrix interface has been completely damaged. Areas of significant plasticity strain with output $PEEQ > 1\%$ are colored in gray. It can be observed that at Peak Load, matrix plasticity damage can be extensive. The extent of high-plasticity-strain area throughout the fiber push-out experiment is strongly dependent on many factors including the matrix yield properties, interfacial friction, interfacial strength and fracture energy.

In conclusion, preliminary analyses in this Section demonstrated *qualitatively* the very complex coupling interaction between material parameters and their effects on the IFSS measurement. Below are some of the identified interactions:

- Matrix plasticity damage evolution depends on different parameters in addition to matrix plasticity properties themselves: interface strength IFSS, interface fracture energy G_{II}, interface friction properties μ.

- Strong coupling interaction between different phenomena: matrix plasticity damage evolution, interface damage evolution, interface friction post-failure.
- Permanent plastic matrix deformation induces non-zero interface friction stress even without the curing/manufacturing residual stress due to the creation of non-zero normal stress at the interface.

Sensitivity studies of effects from different parameters on the IFSS measurement using fiber push-out method

Due to the combination of the complex parameter interaction and the lack of precise characterization of microscopic properties, for the main sensitivity studies, reference model utilizes a linear elastic without plasticity material model for the matrix. Residual stress is also not included in the reference FE model – and is only modeled in the specific studies concerning effects of the residual stress. This simplification of the reference allows a better decoupling of effects from different phenomena for easier analysis.

In the results presenting Load-Displacement curves, the corresponding experimental Load-Displacement curve is also plotted for quick reference and comparison. Reference interface model utilizes the properties presented in table 19, where input IFSS is equal to the experimental IFSS. This reference input/experimental IFSS is also plotted next to the charts of apparent IFSS for quick reference and comparison.

Effects from input IFSS

Ideally, the IFSS derived from the Peak Load measurement in a fiber push-out simulation ($apparent\ IFSS$) should be equal to the $input\ IFSS$. In practice, different unwanted phenomena affect this measurement, causing the inequality between these two parameters. Figure 48 presents the effects of the input IFSS. Some important remarks can be made:

- The input IFSS, as expected, has very significant effects on the nanoindenter Load-Displacement curve.

- The apparent IFSS and input IFSS have a roughly linear correlation. However, in some cases, the two values are not precisely equal (i.e., $apparent\ IFSS \neq input\ IFSS$), probably due to other effects including the interface fracture energy.

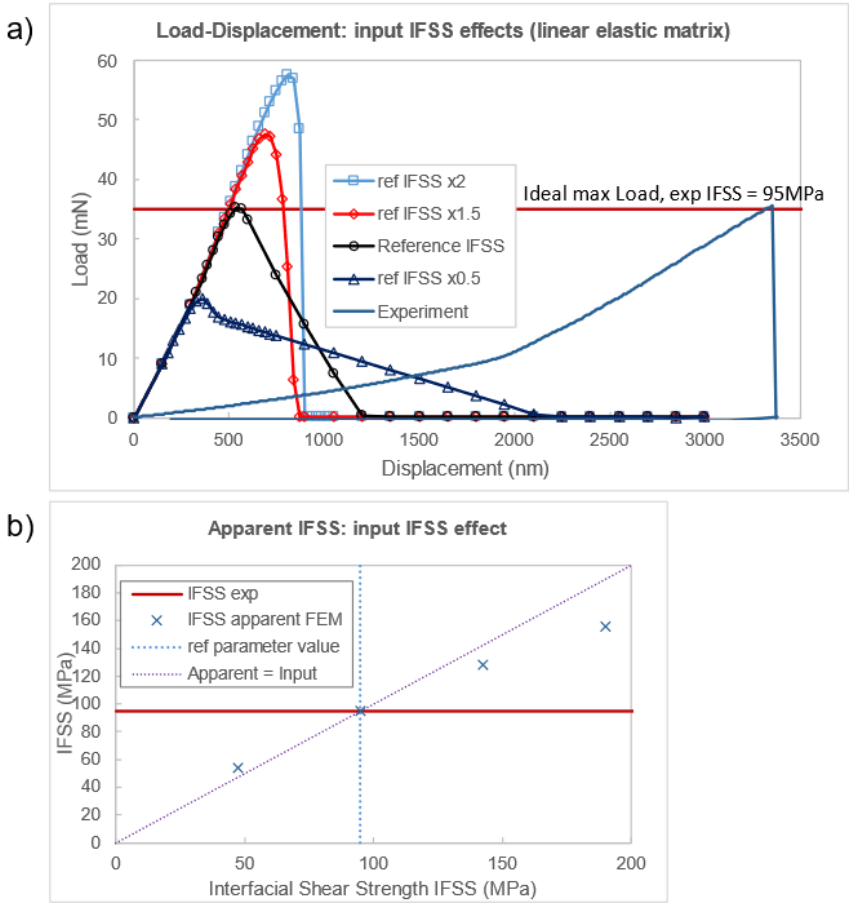

Figure 48. Effects of input IFSS: a) Load-Displacement curve; b) Apparent IFSS.

To further evaluate the interference of interface (shear) fracture energy G_{II} on apparent IFSS, another series of IFSS input sensitivity is performed with fracture energy much lower than the estimated reference value ($100\ J/m^2$): $G_{II} = 3.125\ J/m^2 = G_{II}^{ref}/16$. Figure 49 presents the results of this study. Some important remarks can be made:

- The input IFSS still has significant effects on the apparent IFSS. Higher input IFSS leads to higher apparent IFSS.
- However, at higher input IFSS values, the difference between apparent IFSS and input IFSS becomes much more significant. Effectively, the simple deduction of IFSS

from nanoindenter Peak Load becomes much less accurate. This is due to the effects of fracture energy G_{II} becoming much more dominating in the process of interface failure.

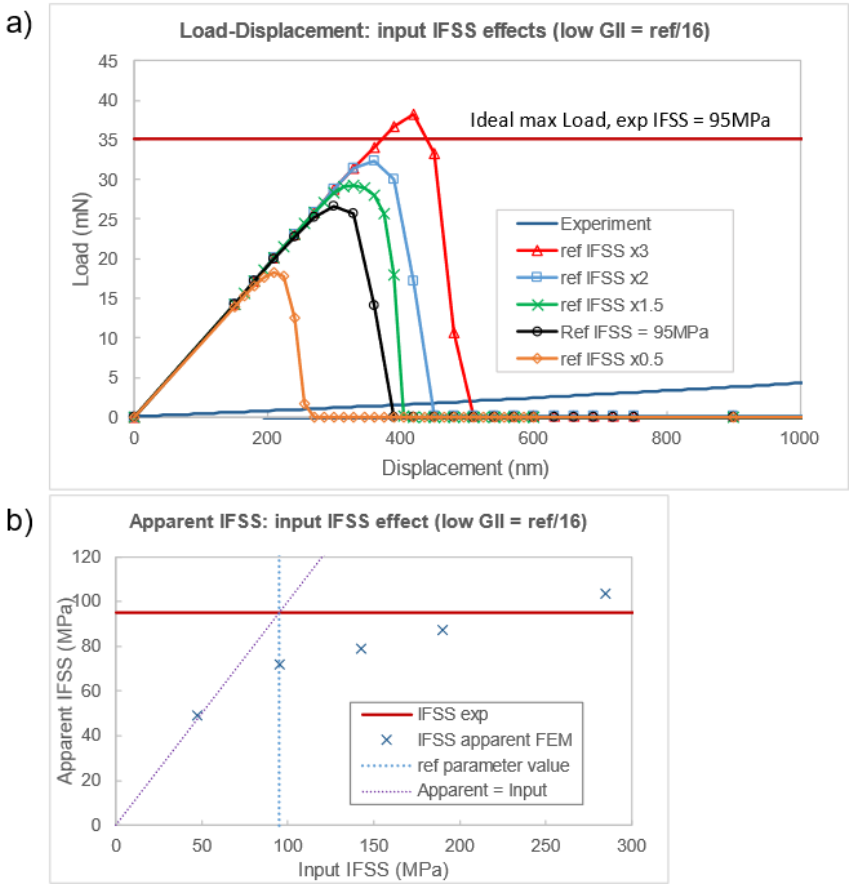

Figure 49. Effects of input IFSS with very low G_{II}. a) Load-Displacement curve; b) Apparent IFSS.

Effects from interface shear fracture energy G_{II}

Figure 50 presents effects of G_{II}. Some important remarks can be made:

- The G_{II} has very significant effects on the nanoindenter Load-Displacement curve. However, the precise effects are different between the (comparatively) low and high regimes of G_{II}. At the low regime, the G_{II} has very significant influence on the Peak Load which is followed by a sudden “drop”, suggesting the fracture energy being the dominant factor in the interface failure progress. At the high regime, the G_{II} has insignificant effect on the Peak Load, but significant influence on the gradual Load decrease after the Peak Load.

- At high G_{II}, apparent IFSS converges towards the input IFSS. The virtual IFSS measurement using fiber push-out is accurate and is independent of the precise value of G_{II}.
- The corresponding experimental curve exhibits a “sudden drop” following Peak Load, suggesting that interface fracture in this case might be energy-dominated.

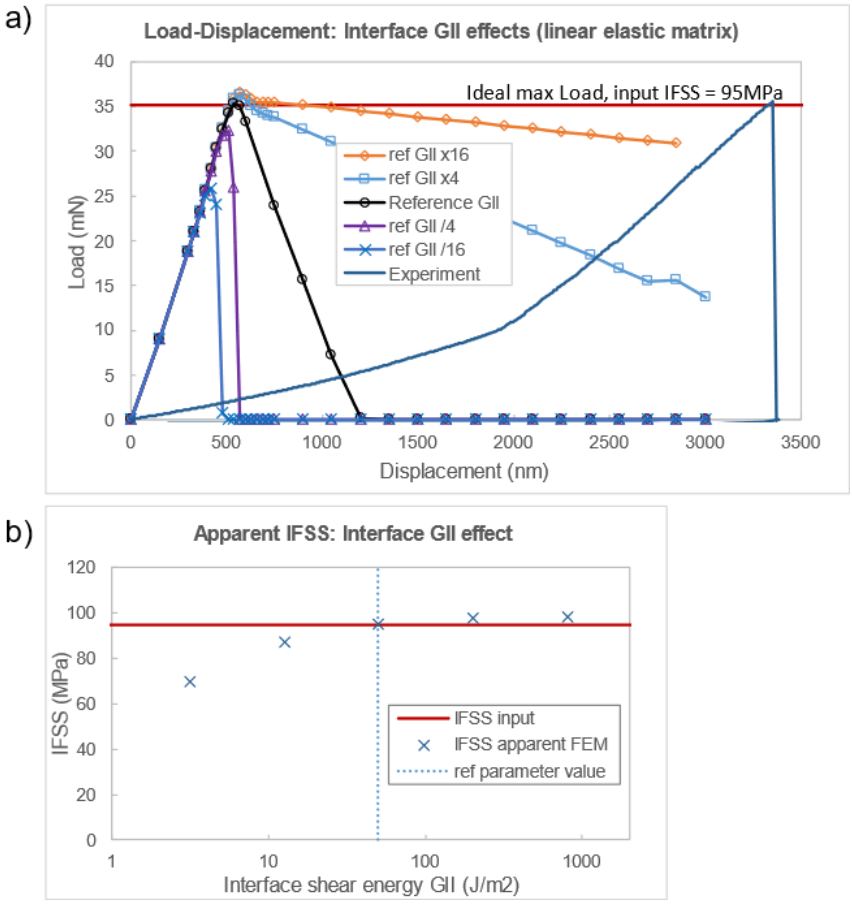

Figure 50. Effects of G_{II}. a) Load-Displacement curve; b) Apparent IFSS.

Effects from interface coefficient of friction μ in absence of residual stress

In the absence of residual stress in the FE model, Figure 51 presents effects of interface friction. Some important remarks can be made:

- The interface friction coefficient μ has some observable, but very small effects on the Load-Displacement curve, including the Peak Load and post-Peak behaviors.

For reference, the coefficient of friction at the IM7/8552 carbon/epoxy interface is estimated at $\mu = 0.4$ [60].

- Following the complete interface failure, interface friction stress is almost zero due to the absence of interface normal stress at this stage in a model with fully elastic materials.

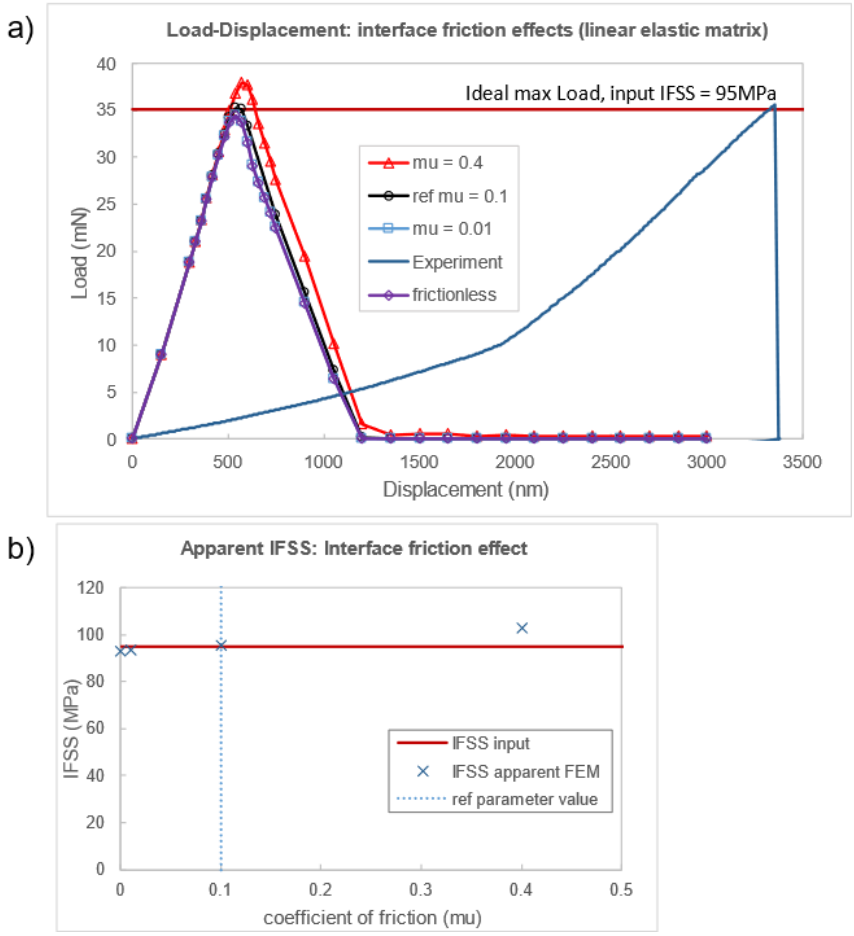

Figure 51. Effects of interface coefficient of friction μ. a) Load-Displacement curve; b) Apparent IFSS.

Effects from matrix Tension Yield σ_t^y and Compression Yield σ_c^y

In this study, the reference yield properties for the F3G epoxy matrix are provided in Table 18.

Figure 52 presents effects of matrix tension yield σ_t^y. Some important remarks can be made:

- σ_t^y has significant effects on the Load-Displacement curve. Higher matrix tension yield leads to higher Peak Load, gradually approaching the Load-Displacement curve of the model with linear elastic matrix where the Peak Load is equal to the Ideal max Load.

- σ_t^y also has significant effects on the post-failure load through at least two effects. First, the gradual yielding of the matrix surrounding the push-out fiber, some of which is still "attached" to the fiber due to incomplete interface failure, leads to a gradual decrease of the indenter Load following the Peak Load. Second, permanent plastic deformation creates some residual interface normal stress following total interface failure, causing friction stress. The friction stress itself is dependent on the plasticity deformation profile and the matrix yield properties.

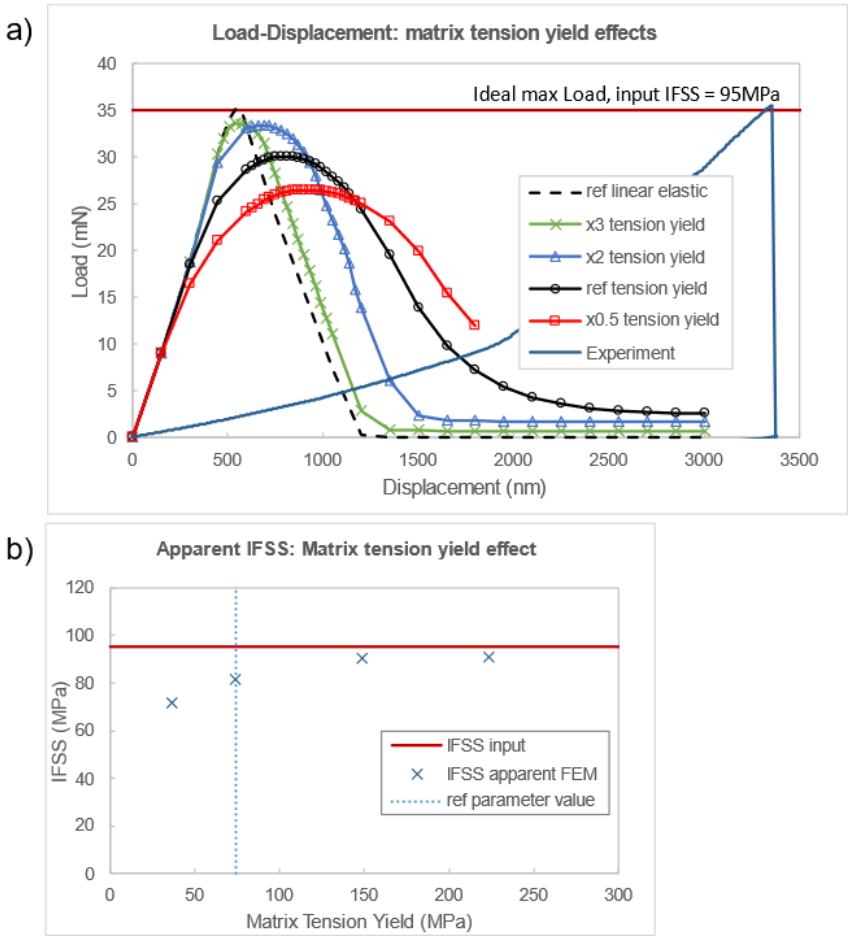

Figure 52. Effects of matrix tension yield σ_t^y. a) Load-Displacement curve; b) Apparent IFSS.

Figure 53 presents effects of matrix compression yield σ_c^y. Overall, parametric effects of the compression yield are similar to those of tension yield, including effects on Peak Load and apparent IFSS, convergence towards the reference input/experimental IFSS, and effects on the Load-Displacement evolution after the Peak Load.

Intuitively, this lowering of Peak Load can be seen as the “apparent effect” of the Load measured by the nanoindenter. Due to the matrix yielding in the volume neighboring the push-out fiber, this creates a “softening effect” on the reaction force acting on the fiber and consequently captured by the FEM nanoindenter.

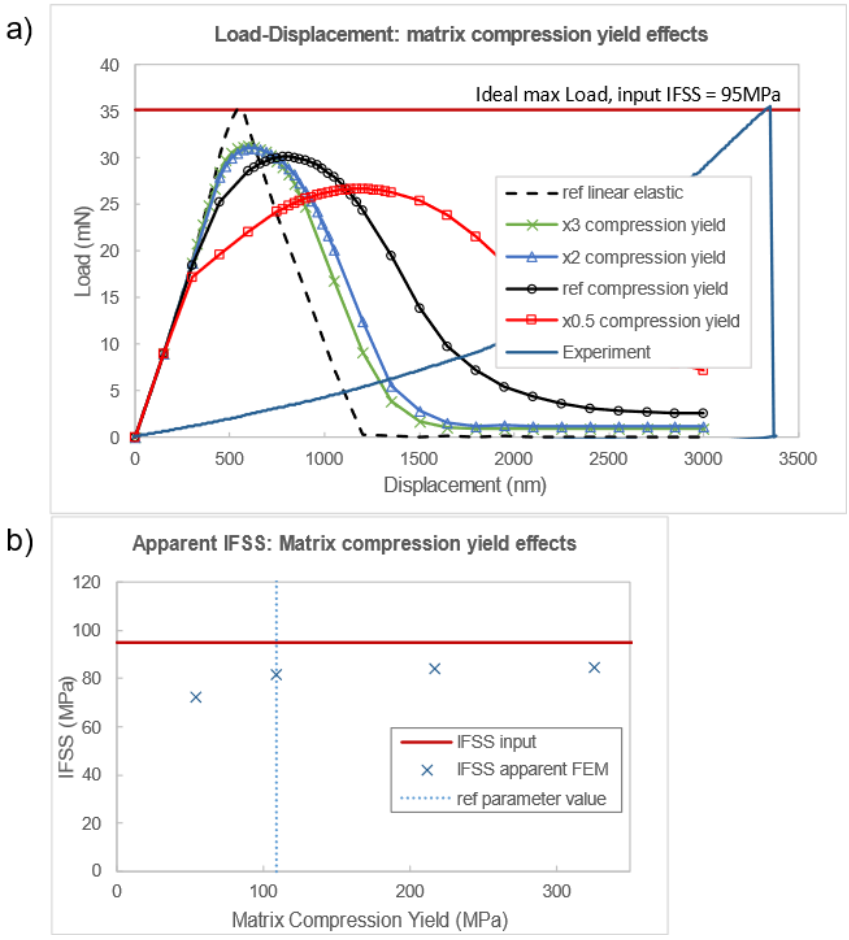

Figure 53. Effects of σ_c^y. a) Load-Displacement curve; b) Apparent IFSS.

Combined effects of membrane thickness and matrix plastic damage

Another effect of the matrix plastic yielding is the occurrence of a “divergence” of Load-Displacement curve from the initial linear slope, where the curve becomes less

steep which eventually leads to a lower Peak Load. In the article of Ghaffari et al. [61], the authors reported this non-linear divergence on the experimental Load-Displacement curves and theorized that the matrix plastic deformation being the cause of this divergence. To verify this hypothesis, FE models with linear and non-linear matrix material models are evaluated and compared. FE models of two different membrane thickness (but otherwise identical geometry) are evaluated to investigate possible coupling effects of the specimen thickness on the matrix plastic deformation.

Figure 54 presents effects of plastic damage on the Load-Displacement curves. The non-linear divergence is observed on both models with the two thickness values. Figure 55 presents the development of matrix plastic damage at several important events during the fiber push-out simulation: at the onset of non-linear divergence; some time after when the divergence becomes more pronounced; and at the Peak Load. It is confirmed that the “divergence” corresponds with the initiation of matrix plastic damage, and the continued softening corresponds with the development of matrix damage along the push-out experiment.

In addition, membrane thickness also has some effects on the Load-Displacement curves in both cases of linear elastic and non-linear matrix materials. In the case of linear elastic matrix, the model of reference thickness provides a very good measurement of apparent IFSS at 101% input IFSS, while the model of 2/3 reference thickness provides a slight underestimation at 97% input IFSS. In the case of non-linear matrix with plasticity damage, the model of reference thickness underestimates the input IFSS by 14%, while the model of 2/3 reference thickness underestimates the input IFSS by 19%. This difference is due to the thinner membrane being more compliant under load, more susceptible to matrix plasticity damage, less uniform interface stress distribution – the final combined effects being a more non-linear Load-Displacement curve and more IFSS underestimation compared to the thicker membrane specimen.

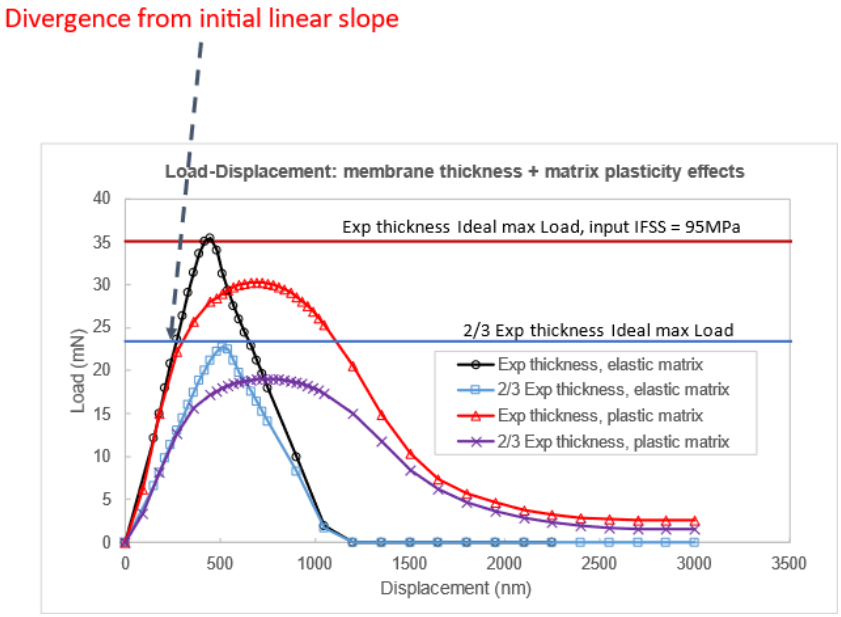

Figure 54. Effects of matrix plasticity damage causing the “divergence” from the initial linear slope.

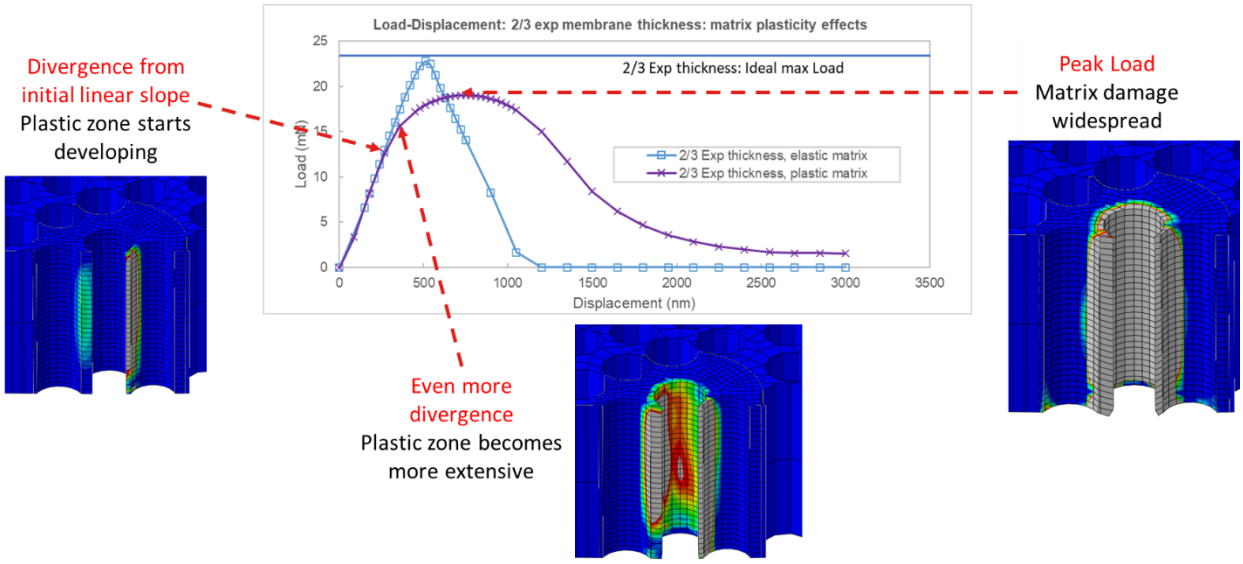

Figure 55. Areas where $PEEQ > 1\%$ are colored in gray. Matrix PEEQ developments at several important time points are presented, corresponding with effects of matrix plastic damage on Load-Displacement curve.

Combined effects of residual stress and interface friction

Since the curing process involves the significant shrinkage of epoxy compared to the reinforcing fiber, it is expected and verified in the FE models that residual stress

from this process would have a “squeezing” effect, or positive normal pressure at the fiber-matrix interface. Figure 56 presents effects of a curing shrinkage of 3.45% (estimated from the FEMU study) on the nanoindenter Load-Displacement curve, compared to the models without residual stress. Two values of interface friction coefficient $\mu = 0.1$ and $\mu = 0.4$ are evaluated.

- With no residual stress, interface friction coefficient μ has a slight effect on the Peak Load. Higher μ leads to slightly higher Peak Load. After interface total failure, negligible interfacial friction stress is observed.

- With residual stress present, interface friction coefficient μ has much more significant effects on the Load-Displacement curves. With low $\mu = 0.1$, a slight decrease of Peak Load is observed, which can be explained by the premature interfacial damage due to the presence of residual stress. In contrast, a high $\mu = 0.4$ leads to a higher Peak Load due to the delaying effects from the high interface friction stress. After interface total failure, significant interface friction stress is observed which is strongly dependent on the coefficient of friction.

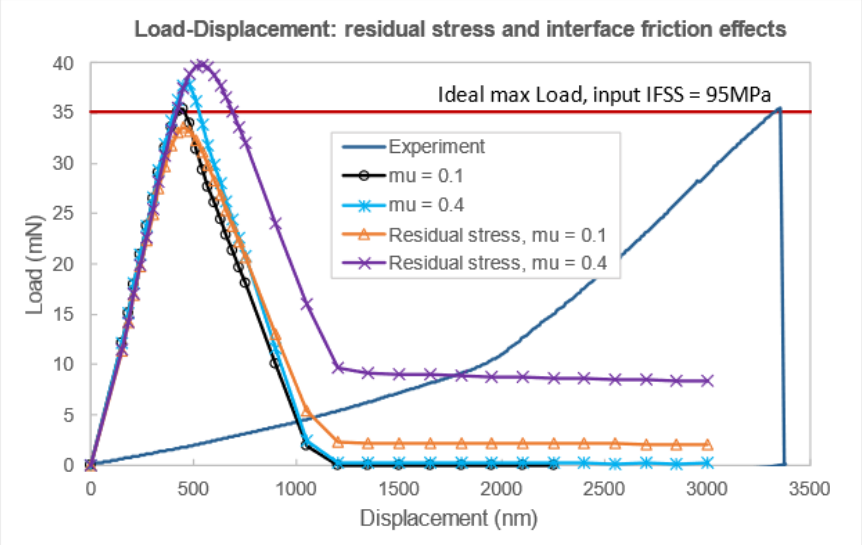

Figure 56. Combined effects of residual stress and interface friction.

Combined effects of residual stress and matrix plasticity damage

In this study, 4 FE model configurations are evaluated:

1- no Residual stress, Elastic matrix

2- Residual stress, Elastic matrix

3- no Residual stress, Plastic matrix

4- Residual stress, Plastic matrix

The study takes the simplification that matrix plasticity properties are unchanged during the curing process. Figure 57 presents the combined effects of residual stress and matrix plasticity. Some important remarks can be made:

- In the model with Plasticity matrix model, the divergence from the initial linear slope happens earlier due to the residual stress-induced damage to the matrix. Figure 58 shows the output variable PEEQ after Grinding, suggesting significant matrix damage due to the curing and manufacturing process.
- Due to plasticity matrix damage, the model with residual stress produces a slightly lower Peak Load. However, the Peak Load reduction due to the residual stress is much smaller than the difference between the models with and without matrix plasticity damage.

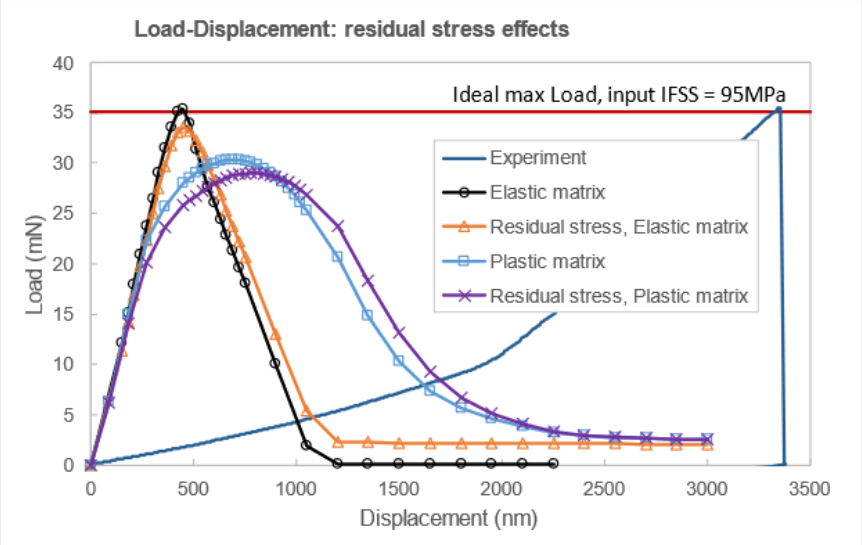

Figure 57. Combined effects of residual stress and matrix plasticity damage.

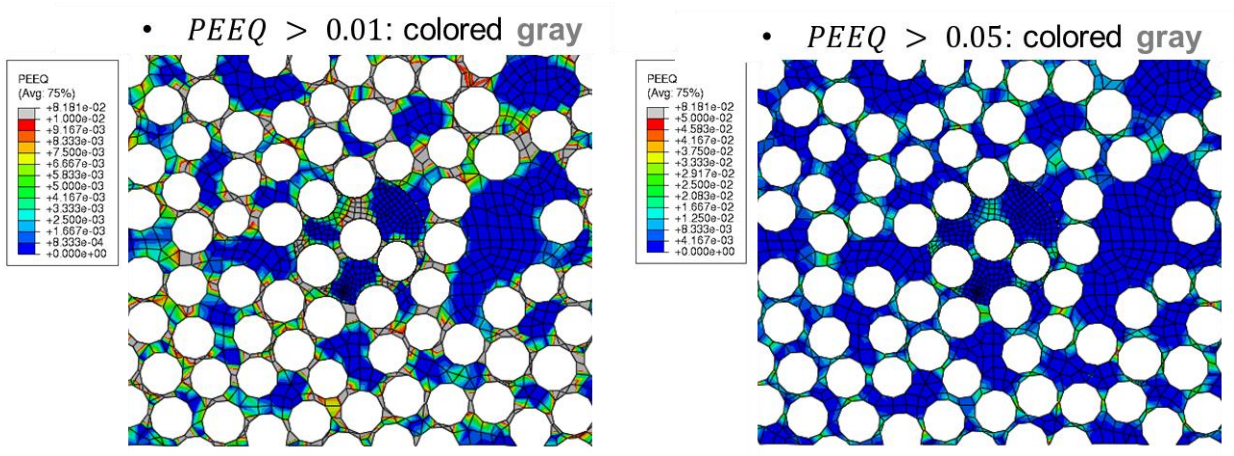

Figure 58. Plasticity damage in matrix after Grinding, shown at two different scales.

The yielding and nonlinear deformation of matrix also leads to modification of the stress field in the model, and consequently the difference of the stress at the interface. Figure 59 presents the interface damage variable CSDMG after Grinding. In the model with Plasticity matrix, interface damage is less extensive due to the yielding and plastic deformation of the surrounding matrix leading to lower stress.

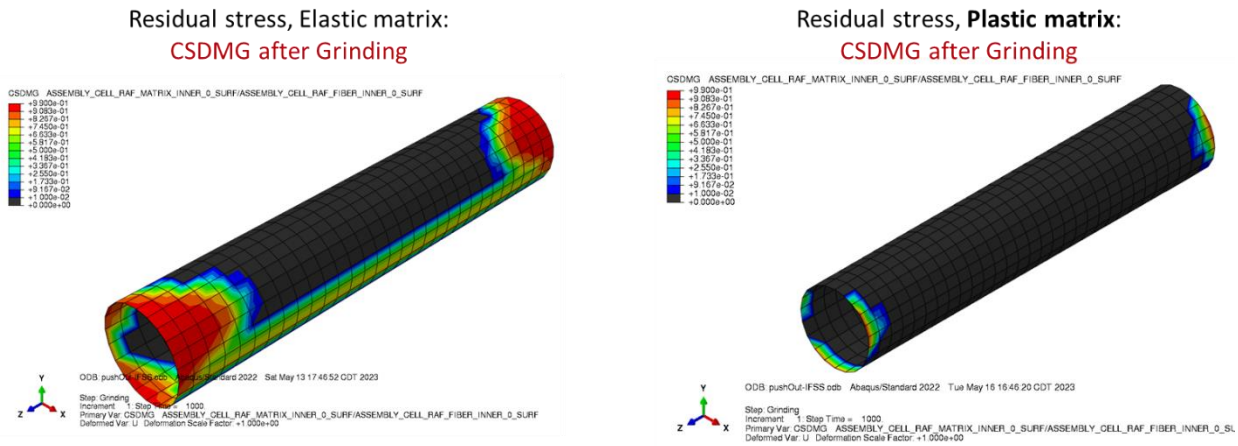

Figure 59. Interface damage after Grinding, models with linear elastic matrix and with plasticity matrix behavior. $CSDMG > 0.99$ (near total failure): colored gray; $CSDMG < 0.01$ (almost intact interface): colored black.

Figure 60 presents the interface damage variable CSDMG at Peak Load for different model configurations. It is shown that both residual stress and plastic matrix damage have very strong effects on the CSDMG distribution at Peak Load. For example, in the case of residual stress with plastic matrix damage, some interface areas

are fully damaged while other areas (at the mid-thickness, facing towards a matrix-rich area) are still intact.

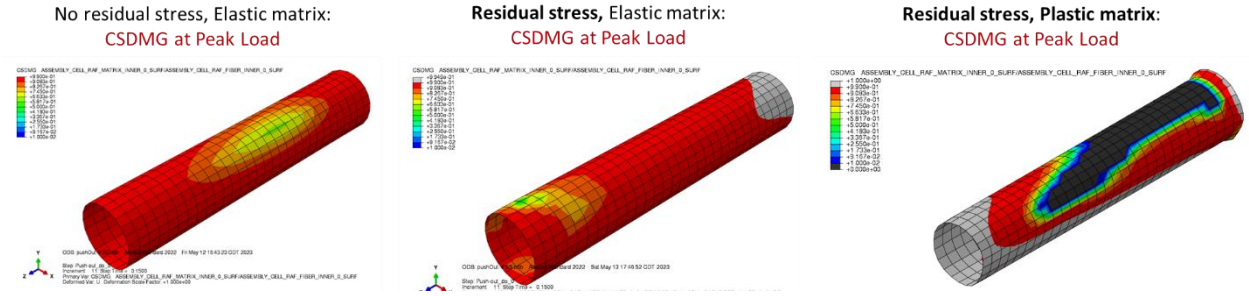

Figure 60. Interface damage at Peak Load. The combined effects of residual stress and plastic matrix damage. $CSDMG > 0.99$ (near total failure): colored gray; $CSDMG < 0.01$ (almost intact interface): colored black.

Effects from model size on the initial slope

As observed in the previous parametric studies, there is always a large discrepancy between the initial slope of the FEM-predicted and the experimental Load-Displacement curves. From the sensitivity analyses, it seems that this significant difference cannot be explained simply through the uncertainties of the material properties.

A study that focuses on the effect of membrane size on the initial slope of Load-Displacement curve is performed. Figure 61 presents the Push-Out specimen under SEM and two of the FE geometries in this study, the images being approximately to scale to allow a quick comparison and reference. Since the experimental initial slope is less steep than the FEM initial slope, the size study focuses on the width dimension of the FE model which has the effect of lowering the apparent stiffness as measured by the indenter at the push-out fiber.

Figure 62.a presents the effects of the FE model width dimension on the Load-Displacement response of the Fiber 1. Effects of a significant width increase above the reference are very insignificant, and cannot reproduce the very gradual initial slope in the experiment. Figure 62.b presents the Load-Displacement data for all push-out fibers in the same experiment, showing a very consistent overcompliance effect over different fibers. Therefore, the gradual initial experimental slope is most likely the result of the

imperfect specimen-support contact before and during the push-out experiment, as was pointed out by Ghaffari et al. [61]. Figure 63 shows the corresponding experimental reference specimen under SEM, where a gap is visible between the specimen and the mount. To solve this problem of overcompliance, the AMSL/UTA Research Team proposed the Cave Configuration for fiber push-out experiment where boundary conditions determination is much more precise as there is no “gap” between the push-out membrane and the mount. With experimental and numerical results, The AMSL/UTA Team demonstrated the elimination of the overcompliance effects using the new Cave Configuration [61].

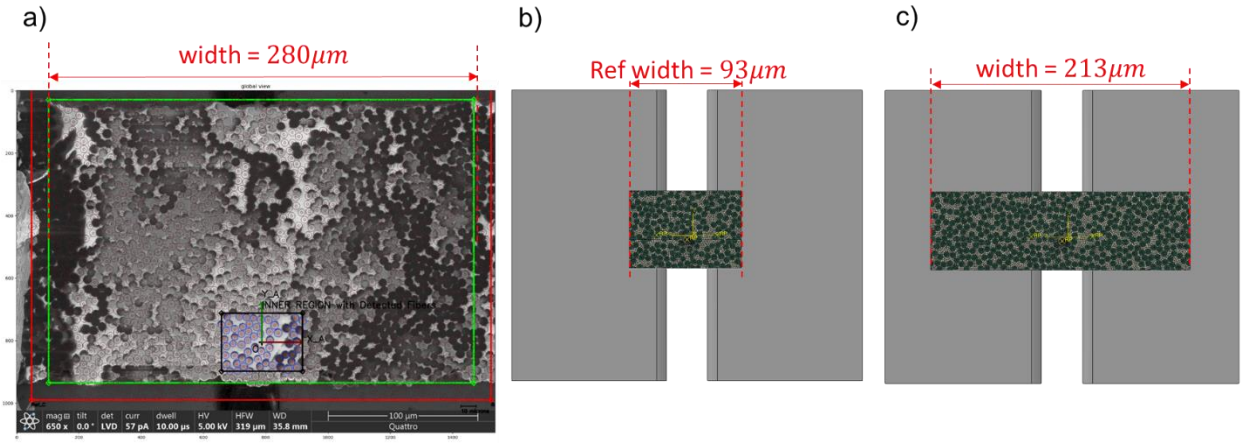

Figure 61. a) Fiber push-out specimen under SEM; b) Reference, size-converged FE geometry; c) A FE geometry with extended width for size effects analysis. Images are approximately to scale.

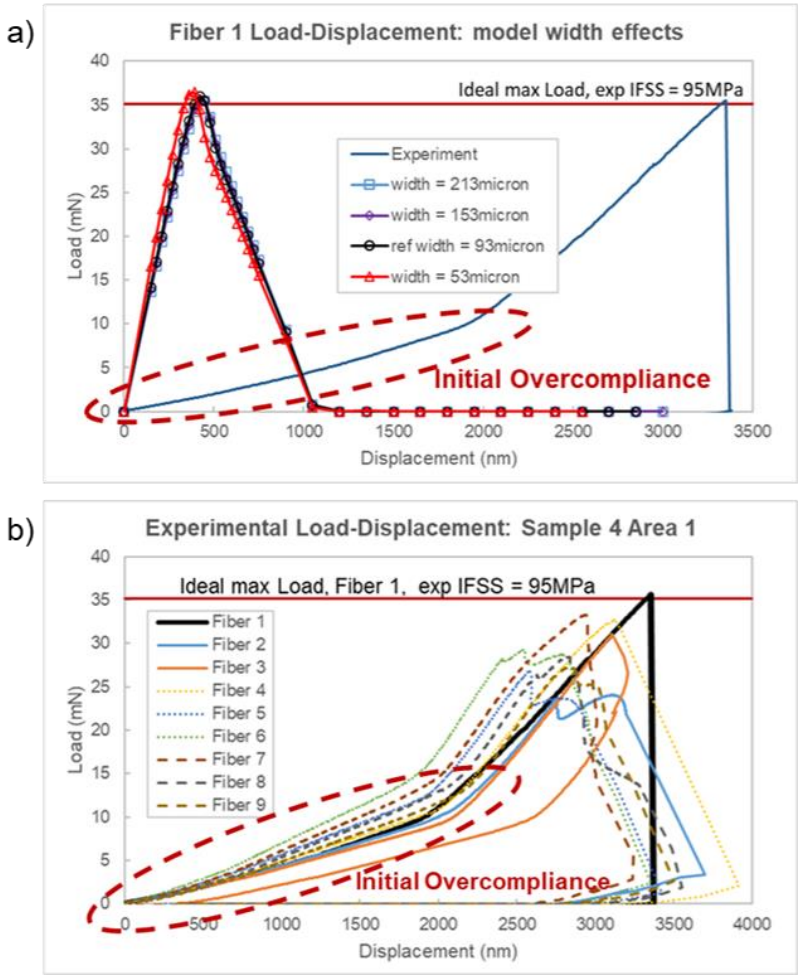

Figure 62. a) Effects of model width on Load-Displacement curve; b) Load-Displacement data plotted for all push-out fibers in the experiment, showing consistent initial overcompliance.

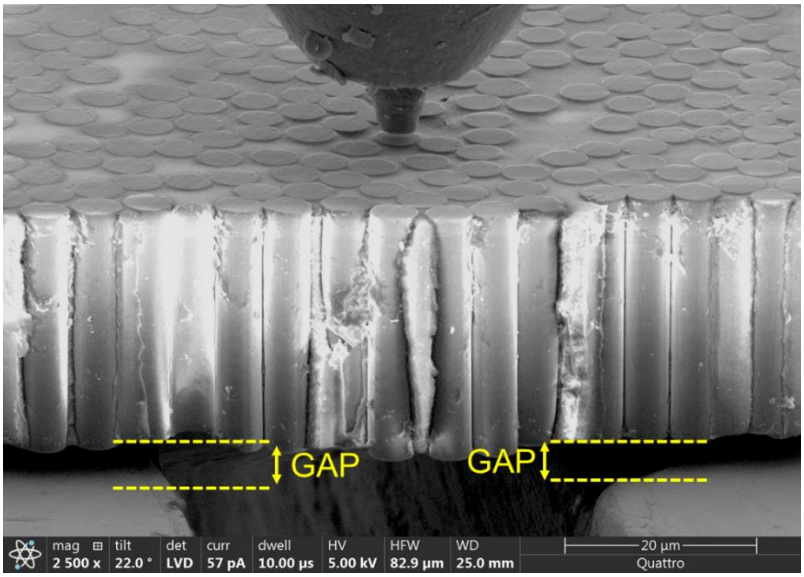

Figure 63. The reference fiber push-out sample under SEM. A gap is visible between the specimen and the support, indicating imperfect contact.

5.5. Conclusions

In the FE models of the fiber push-out experiment, the addition of residual stress into the model has some effect on the Peak Load. However, this effect is small compared to the errors induced by the uncertainties in other material properties such as matrix plasticity and interface fracture energy. In addition, the current residual stress is believed to be overestimated, suggesting that the residual stress and its effects in reality might be even weaker than those presented in this analysis.

As a result, it can be concluded that even though the residual stress has some observable effects on the precise process of matrix and interface failure during the fiber push-out, effects of the residual stress on the IFSS measurement itself is insignificant.

Elsewhere, from the sensitivity analyses, several factors were identified as having significant negative impact on the IFSS measurement accuracy using the fiber push-out method: (comparatively) low interface shear fracture energy; low matrix yield; too small membrane thickness. Conversely, the IFSS measurement accuracy is better when the interface shear fracture is high; matrix has high yield, and the membrane specimen is sufficiently thick.

The free-standing setup for the fiber push-out experiment has the important weakness of the imperfect specimen-mount contact, leading to the overcompliance problem that is observed on the initial slope of the nanoindenter Load-Displacement response. In turn, this overcompliance problem makes it difficult to calibrate the results of the IFSS measurement due to the introduction of another unknown.

Ghaffari et al. demonstrated the absence of the overcompliance problem on the results obtained from the Cave Configuration fiber push-out tests [61]. Therefore, if the equipment for specimen preparation is available, it is suggested that the Cave Configuration should be preferred over the free-standing configuration. The Cave Configuration effectively eliminates one unknown variable (on the boundary conditions at the limits of the membrane), allowing a much better FE modeling of the experiment and much more robust result interpretation.

CHAPTER 6
Conclusions

A FE RVE micromodel simulating the fiber-direction compressive failure of composite has been developed. Literature review on the high-performance CFRP suggested that fiber-direction compressive failure is initiated by the matrix shear yielding/failure precipitated by local fiber misalignment, subsequently causing kink-band formation and possible fiber failure due to extreme rotation at the kink-band boundaries. As a result, it seems that the current FE model not including fiber damage should be sufficient for the prediction of the fiber-direction compression strength. However, since the experimental kink-bands often show fiber fractures, the FE models for the purpose of reproducing realistic kink-bands should include fiber damage/failure model. In addition, as the kink-band boundaries are typically inclined, the Periodic Boundary Condition is unsuitable for the simulation of kink-band formations. The study of the FE RVE identified several parameters with strong effects on composite strength which are confirmed by previous studies in the literature. Parametric analysis and comparison using the RVEs suggest that the low strength of HM composite is due to its low IFSS, increasing its susceptibility to micro-instabilities and buckling under axial compression load. Future works were proposed on the topic. High priority is assigned to the validation of micromodel using the 4-point-bending notched specimen setup, and the improvement of the RVE with realistic random fiber misalignment, which are the essential prerequisites for the design of hybrid composites using numerical tools.

Due to the numerous parameters required for FE modeling input, an extensive literature review on relevant microscale material properties were performed, providing an overview on the availability of relevant parameters and the state of the art in their measurement methods. A complete presentation and application results were provided for the measurement of reinforcing fibers orthotropic elastic properties using the FEMU technique. An FEM analysis was provided to demonstrate the capacities and limitations of the nanoindentation technique for the measurement of microscale properties of epoxy. A feasibility study including analytical analysis was provided for the measurement of reinforcing fibers axial compression failure strain using the Bending

Beam method. It is strongly recommended that experimental work is conducted to characterize reinforcing fiber compression failure due to the necessity of representing fiber damage in the model, the relative simplicity of Bending Beam experimental result analysis, and the availability of equipment required for this experimental method.

As several authors in their numerical and experimental works demonstrated the significant impact of microscale residual stress on the macroscale composite strengths, reliable reproduction of residual stress in micromodels is necessary for the accurate modeling of composite failure. Meanwhile, at the time there was a lack of established experimental method for the characterization of microscale residual stress in composite matrix. This project proposed a new method for the assessment of microscale residual stress in matrix. In fiber push-out experiments with in-situ SEM monitoring, significant matrix sink-in deformation was observed after the fibers surrounding a matrix-rich pocket have been pushed out. This sink-in, confirmed by the nanoindenter position recordings, is associated with the relaxed residual stress in matrix after its interfaces with the surrounding fibers have been broken. The matrix sink-in deformation is evaluated using the FEMU technique for the inverse characterization of residual stress field. Preliminary results suggested a very significant level of residual stress in composite matrix that is of the same order of magnitude as some material strengths. However, the residual stress values were apparently overestimated. Continuing works were performed where several potential error-inducing factors were identified and improvements were proposed, implemented, and analyzed.

The FE model suggested the strong influence of the fiber-matrix Interfacial Shear Strength on the composite fiber-direction compression strength, which is also confirmed by earlier authors in the literature. The IFSS is therefore of high priority in the efforts to improve composite material performance, and the accurate measurement of the IFSS is of critical importance. An FE model was developed based on the corresponding experimental specimen for the analysis of factors interfering with the accuracy of the IFSS measurement using fiber push-out method. Low interface shear fracture energy, low matrix yield and too thin membrane were identified as factors with strong negative impact on the IFSS measurement accuracy. Meanwhile, residual stress, despite its effects of modifying the precise damage process during the fiber push-out, was found to

have a rather insignificant effect on the IFSS measurement. It was also proposed that the Cave Configuration for fiber push-out experiment is preferable as the boundary conditions can be determined and modeled much more accurately.

References

[1] D. J. Farrar, “The Design of Compression Structures for Minimum Weight,” *J. R. Aeronaut. Soc.*, vol. 53, no. 467, pp. 1041–1052, Nov. 1949, doi: 10.1017/S0368393100120747.

[2] B. Smith, R. Grove, and T. Munns, *Failure Analysis of Composite Structure Materials*. Materials Laboratory, Air Force Wright Aeronautical Laboratories, 1986.

[3] C. R. Schultheisz and A. M. Waas, “Compressive failure of composites, part I: Testing and micromechanical theories,” *Progress in Aerospace Sciences*, vol. 32, no. 1, pp. 1–42, Jan. 1996, doi: 10.1016/0376-0421(94)00002-3.

[4] D. R. Tenney, J. G. Davis Jr, N. J. Johnston, R. B. Pipes, and J. F. McGuire, “Structural Framework for flight: NASA’s role in development of advanced composite materials for aircraft and space structures,” 2011.

[5] R. Butler, A. T. Rhead, W. Liu, and N. Kontis, “Compressive strength of delaminated aerospace composites,” *Phil. Trans. R. Soc. A.*, vol. 370, no. 1965, pp. 1759–1779, Apr. 2012, doi: 10.1098/rsta.2011.0339.

[6] R. Sturm, Y. Klett, Ch. Kindervater, and H. Voggenreiter, “Failure of CFRP airframe sandwich panels under crash-relevant loading conditions,” *Composite Structures*, vol. 112, pp. 11–21, Jun. 2014, doi: 10.1016/j.compstruct.2014.02.001.

[7] N. Zimmermann and P. H. Wang, “A review of failure modes and fracture analysis of aircraft composite materials,” *Engineering Failure Analysis*, vol. 115, p. 104692, Sep. 2020, doi: 10.1016/j.engfailanal.2020.104692.

[8] N. F. Dow, B. W. Rosen, L. S. Shu, and C. H. Zweben, “Design criteria and concepts for fibrous composite structures Final report,” 1967. [Online]. Available: https://ntrs.nasa.gov/api/citations/19680004493/downloads/19680004493.pdf

[9] M. R. Piggott and B. Harris, “Compression strength of hybrid fibre-reinforced plastics,” *J Mater Sci*, vol. 16, no. 3, pp. 687–693, Mar. 1981, doi: 10.1007/BF02402786.

[10] H. T. Hahn and J. G. Williams, “Compression Failure Mechanisms in Unidirectional Composites,” Philadelphia, 1986.

[11] P. S. Steif, “A model for kinking in fiber composites—I. Fiber breakage via micro-buckling,” *International Journal of Solids and Structures*, vol. 26, no. 5–6, pp. 549–561, 1990, doi: 10.1016/0020-7683(90)90028-T.

[12] M. Wisnom, “On the high compressive strains achieved in bending tests on unidirectional carbon-fibre/epoxy,” *Composites Science and Technology*, vol. 43, no. 3, pp. 229–235, 1992, doi: 10.1016/0266-3538(92)90093-I.

[13] R. A. Schapery, “Prediction of compressive strength and kink bands in composites using a work potential,” *International Journal of Solids and Structures*, vol. 32, no. 6–7, pp. 739–765, Mar. 1995, doi: 10.1016/0020-7683(94)00158-S.

[14] R. Gutkin, S. T. Pinho, P. Robinson, and P. T. Curtis, “A finite fracture mechanics formulation to predict fibre kinking and splitting in CFRP under combined longitudinal compression and in-plane shear,” *Mechanics of Materials*, vol. 43, no. 11, pp. 730–739, Nov. 2011, doi: 10.1016/j.mechmat.2011.08.002.

[15] F. Naya, M. Herraez, C. S. Lopes, C. Gonzalez, S. Van der Veen, and F. Pons, “Computational micromechanics of fiber kinking in unidirectional FRP under different environmental conditions,” *Composites Science and Technology*, vol. 144, pp. 26–35, 2017, doi: https://doi.org/10.1016/j.compscitech.2017.03.014.

[16] S. M. Koppisetty, S. B. Cheryala, and C. S. Yerramalli, “The effect of fiber distribution on the compressive strength of hybrid polymer composites,” *Journal of Reinforced Plastics and Composites*, vol. 38, no. 2, pp. 74–87, Jan. 2019, doi: 10.1177/0731684418804346.

[17] A. Makeev, S. Ghaffari, and G. Seon, “Improving compressive strength of high modulus carbon-fiber reinforced polymeric composites through fiber hybridization,” *International Journal of Engineering Science*, vol. 142, pp. 145–157, Sep. 2019, doi: 10.1016/j.ijengsci.2019.06.004.

[18] S. Ghaffari, A. Makeev, G. Seon, D. P. Cole, D. J. Magagnosc, and S. Bhowmick, “Understanding compressive strength improvement of high modulus carbon-fiber reinforced polymeric composites through fiber-matrix interface characterization,” *Materials & Design*, vol. 193, p. 108798, Aug. 2020, doi: 10.1016/j.matdes.2020.108798.

[19] HexTow, “HexTow Carbon Fiber Selector Guide.” [Online]. Available: https://www.hexcel.com/user_area/content_media/raw/HexTowSelectorGuide.pdf

[20] E. J. Barbero and J. Tomblin, “A damage mechanics model for compression strength of composites,” *International Journal of Solids and Structures*, vol. 33, no. 29, pp. 4379–4393, Dec. 1996, doi: 10.1016/0020-7683(95)00236-7.

[21] B. Budiansky and N. A. Fleck, “Compressive failure of fibre composites,” *Journal of the Mechanics and Physics of Solids*, vol. 41, no. 1, pp. 183–211, Jan. 1993, doi: 10.1016/0022-5096(93)90068-Q.

[22] M. Herraez, A. C. Bergan, C. Gonzalez, and C. S. Lopes, “Modeling fiber kinking at the microscale and mesoscale,” 2018.

[23] S. Ghaffari, A. Makeev, D. Kuksenko, and G. Seon, “Understanding High-Modulus CFRP Compressive Strength Improvement,” presented at the American Society for Composites, 34th Technical Conference, 2019. doi: 10.12783/asc34/31352.

[24] C. S. Yerramalli and A. M. W. Waas, “Compressive Behavior of Hybrid Composites,” Norfolk, Virginia, 2003.

[25] Sudarisman, I. J. Davies, and H. Hamada, “Compressive failure of unidirectional hybrid fibre-reinforced epoxy composites containing carbon and silicon carbide fibres,” *Composites Part A: Applied Science and Manufacturing*, vol. 38, no. 3, pp. 1070–1074, Mar. 2007, doi: 10.1016/j.compositesa.2006.10.004.

[26] J. Aveston and J. M. Sillwood, “Synergistic fibre strengthening in hybrid composites,” *J Mater Sci*, vol. 11, no. 10, pp. 1877–1883, Oct. 1976, doi: 10.1007/BF00708266.

[27] R. Gutkin, S. T. Pinho, P. Robinson, and P. T. Curtis, “Micro-mechanical modelling of shear-driven fibre compressive failure and of fibre kinking for failure envelope generation in CFRP laminates,” *Composites Science and Technology*, vol. 70, no. 8, pp. 1214–1222, Aug. 2010, doi: 10.1016/j.compscitech.2010.03.009.

[28] J. Patel and P. Peralta, “Mechanisms for Kink Band Evolution in Polymer Matrix Composites: A Digital Image Correlation and Finite Element Study,” in *Volume 9: Mechanics of Solids, Structures and Fluids; NDE, Diagnosis, and Prognosis*, Phoenix, Arizona, USA: American Society of Mechanical Engineers, Nov. 2016, p. V009T12A055. doi: 10.1115/IMECE2016-67482.

[29] I. M. Daniel, H.-M. Hsiao, and S.-C. Wooh, “Failure mechanisms in thick composites under compressive loading,” *Composites Part B: Engineering*, vol. 27, no. 6, pp. 543–552, Jan. 1996, doi: 10.1016/1359-8368(95)00010-0.

[30] Y. Wang, Y. Chai, C. Soutis, and P. J. Withers, “Evolution of kink bands in a notched unidirectional carbon fibre-epoxy composite under four-point bending,” *Composites Science and Technology*, vol. 172, pp. 143–152, Mar. 2019, doi: 10.1016/j.compscitech.2019.01.014.

[31] S. Ghaffari, G. Seon, A. Makeev, E. Iarve, and D. Mollenhauer, “Microstructural Methods for Developing High-Performance Composite Materials,” Orlando, FL, 2020. doi: https://doi.org/10.2514/6.2020-2109.

[32] Y. Wang, C. Soutis, and P. Withers, “X-ray microtomographic imaging of kink bands in carbon fibre-epoxy composites,” Jun. 2014.

[33] C. González and J. LLorca, “Mechanical behavior of unidirectional fiber-reinforced polymers under transverse compression: Microscopic mechanisms and modeling,” *Composites Science and Technology*, vol. 67, no. 13, pp. 2795–2806, Oct. 2007, doi: 10.1016/j.compscitech.2007.02.001.

[34] D. Garoz Gomez, F. Gilabert, R. Sevenois, S. Spronk, A. Rezaei, and W. Van Paepegem, “DEFINITION OF PERIODIC BOUNDARY CONDITIONS IN EXPLICIT DYNAMIC SIMULATIONS OF MICRO-OR MESO-SCALE UNIT CELLS WITH CONFORMAL AND NON-CONFORMAL MESHES,” Jun. 2016.

[35] S. W. Yurgartis, “Measurement of small angle fiber misalignments in continuous fiber composites,” *Composites Science and Technology*, vol. 30, no. 4, pp. 279–293, Jan. 1987, doi: 10.1016/0266-3538(87)90016-9.

[36] M. P. F. Sutcliffe, S. L. Lemanski, and A. E. Scott, “Measurement of fibre waviness in industrial composite components,” *Composites Science and Technology*, vol. 72, no. 16, pp. 2016–2023, Nov. 2012, doi: 10.1016/j.compscitech.2012.09.001.

[37] M. Maiaru, R. J. D’Mello, and A. M. Waas, “Characterization of intralaminar strengths of virtually cured polymer matrix composites,” *Composites Part B*, vol. 149, pp. 285–295, 2018, doi: https://doi.org/10.1016/j.compositesb.2018.02.018.

[38] Z. Shan and A. M. Gokhale, “Representative volume element for non-uniform micro-structure,” *Computational Materials Science*, vol. 24, no. 3, pp. 361–379, Jun. 2002, doi: 10.1016/S0927-0256(01)00257-9.

[39] D. Trias, J. Costa, A. Turon, and J. Hurtado, “Determination of the critical size of a statistical representative volume element (SRVE) for carbon reinforced polymers☆,” *Acta Materialia*, vol. 54, no. 13, pp. 3471–3484, Aug. 2006, doi: 10.1016/j.actamat.2006.03.042.

[40] “IM7 Datasheet.” Accessed: Jun. 28, 2023. [Online]. Available: https://www.hexcel.com/user_area/content_media/raw/IM7_HexTow_DataSheet.pdf

[41] “T300 Datasheet.” Accessed: Jun. 28, 2023. [Online]. Available: https://www.fibermaxcomposites.com/shop/datasheets/T300.pdf

[42] “T800H Datasheet.” Accessed: Jun. 28, 2023. [Online]. Available: https://www.fibermaxcomposites.com/shop/datasheets/CarbonT800MDS.pdf

[43] H. Miyagawa, C. Sato, T. Mase, E. Drown, L. T. Drzal, and K. Ikegami, “Transverse elastic modulus of carbon fibers measured by Raman spectroscopy,” *Materials Science and Engineering: A*, vol. 412, no. 1–2, pp. 88–92, Dec. 2005, doi: 10.1016/j.msea.2005.08.037.

[44] T. S. Gross, N. Timoshchuk, I. I. Tsukrov, R. Piat, and B. Reznik, “On the ability of nanoindentation to measure anisotropic elastic constants of pyrolytic carbon,” *Z. angew. Math. Mech.*, vol. 93, no. 5, pp. 301–312, May 2013, doi: 10.1002/zamm.201100128.

[45] D. Mounier, C. Poilâne, C. Bûcher, and P. Picart, “Evaluation of transverse elastic properties of fibers used in composite materials by laser resonant ultrasound spectroscopy,” 2012. [Online]. Available: https://api.semanticscholar.org/CorpusID:136502997

[46] S. J. Deteresa, S. R. Allen, R. J. Farris, and R. S. Porter, “Compressive and torsional behaviour of Kevlar 49 fibre,” *J Mater Sci*, vol. 19, no. 1, pp. 57–72, Jan. 1984, doi: 10.1007/BF02403111.

[47] C.-L. Tsai and I. M. Daniel, “Determination of shear modulus of single fibers,” *Exp Mech*, vol. 39, no. 4, pp. 284–286, Dec. 1999, doi: 10.1007/BF02329806.

[48] A. A. Gusev, P. J. Hine, and I. M. Ward, “Fiber packing and elastic properties of a transversely random unidirectional glass/epoxy composite,” *Composites Science and Technology*, vol. 60, no. 4, pp. 535–541, Mar. 2000, doi: 10.1016/S0266-3538(99)00152-9.

[49] X. Huang, “Fabrication and Properties of Carbon Fibers,” *Materials*, vol. 2, no. 4, pp. 2369–2403, Dec. 2009, doi: 10.3390/ma2042369.

[50] D. Sinclair, “A Bending Method for Measurement of the Tensile Strength and Young’s Modulus of Glass Fibers,” *Journal of Applied Physics*, vol. 21, no. 5, pp. 380–386, May 1950, doi: 10.1063/1.1699670.

[51] M. Furuyama, M. Higuchi, K. Kubomura, H. Sunago, H. Jiang, and S. Kumar, “Compressive properties of single-filament carbon fibres,” *Journal of Materials Science*, vol. 28, no. 6, pp. 1611–1616, Mar. 1993, doi: 10.1007/BF00363356.

[52] N. Oya and D. J. Johnson, “Longitudinal compressive behaviour and microstructure of PAN-based carbon fibres,” *Carbon*, vol. 39, no. 5, pp. 635–645, Apr. 2001, doi: 10.1016/S0008-6223(00)00147-0.

[53] M. Shioya and M. Nakatani, “Compressive strengths of single carbon fibres and composite strands,” *Composites Science and Technology*, vol. 60, no. 2, pp. 219–229, Feb. 2000, doi: 10.1016/S0266-3538(99)00123-2.

[54] M. Ueda, W. Saito, R. Imahori, D. Kanazawa, and T.-K. Jeong, “Longitudinal direct compression test of a single carbon fiber in a scanning electron microscope,” *Composites Part A: Applied Science and Manufacturing*, vol. 67, pp. 96–101, Dec. 2014, doi: 10.1016/j.compositesa.2014.08.021.

[55] A. Andres Leal, J. M. Deitzel, and J. W. Gillespie, “Assessment of compressive properties of high performance organic fibers,” *Composites Science and Technology*, vol. 67, no. 13, pp. 2786–2794, Oct. 2007, doi: 10.1016/j.compscitech.2007.02.003.

[56] X. Ji *et al.*, “Mechanical and Interfacial Properties Characterisation of Single Carbon Fibres for Composite Applications,” *Exp Mech*, vol. 55, no. 6, pp. 1057–1065, Jul. 2015, doi: 10.1007/s11340-015-0007-3.

[57] J. A. Newell and J. M. Gustafson, “An Improved Interpretation of Recoil Compressive Failure Data for High-Performance Polymers,” *High Performance Polymers*, vol. 13, no. 4, pp. 251–257, Dec. 2001, doi: 10.1088/0954-0083/13/4/303.

[58] H. M. Hawthorne and E. Teghtsoonian, “Axial compression fracture in carbon fibres,” *J Mater Sci*, vol. 10, no. 1, pp. 41–51, Jan. 1975, doi: 10.1007/BF00541030.

[59] S. Fidan, “Experimentation and Analysis of Compression Test methods for Single Filament High Performance Fibres,” Air Force Institute of Technology, Ohio, 1989.

[60] F. Naya, C. González, C. S. Lopes, S. Van Der Veen, and F. Pons, “Computational micromechanics of the transverse and shear behavior of unidirectional fiber reinforced polymers including environmental effects,” *Composites Part A: Applied Science and Manufacturing*, vol. 92, pp. 146–157, Jan. 2017, doi: 10.1016/j.compositesa.2016.06.018.

[61] S. Ghaffari, G. Seon, and A. Makeev, “In-situ SEM based method for assessing fiber-matrix interface shear strength in CFRPs,” *Materials and Design*, vol. 197, 2021, doi: https://doi.org/10.1016/j.matdes.2020.109242.

[62] HEXCEL, “HexPly 8552 datasheet.” Accessed: Mar. 03, 2023. [Online]. Available: https://www.hexcel.com/user_area/content_media/raw/HexPly_8552_us_DataSheet.pdf

[63] I. Oral, H. Guzel, and G. Ahmetli, “Determining the mechanical properties of epoxy resin (DGEBA) composites by ultrasonic velocity measurement,” *J. Appl. Polym. Sci.*, vol. 127, no. 3, pp. 1667–1675, Feb. 2013, doi: 10.1002/app.37534.

[64] A. Smith, S. J. Wilkinson, and W. N. Reynolds, “The elastic constants of some epoxy resins,” *J Mater Sci*, vol. 9, no. 4, pp. 547–550, Apr. 1974, doi: 10.1007/BF02387527.

[65] F. Naya, “Prediction of mechanical properties of unidirectional FRP plies at different environmental conditions by means of computational micromechanics,” Universidad Politénica de Madrid, Madrid, 2017.

[66] O. Verschatse, L. Daelemans, W. Van Paepegem, and K. De Clerck, “In-Situ Observations of Microscale Ductility in a Quasi-Brittle Bulk Scale Epoxy,” *Polymers*, vol. 12, no. 11, p. 2581, Nov. 2020, doi: 10.3390/polym12112581.

[67] T. Jankowiak and T. Lodygowski, “Identification of Parameters of Concrete Damage Plasticity Constitutive Model,” *Foundations of Civil and Environmental Engineering*, 2005.

[68] M. Labibzadeh, M. Zakeri, and A. Adel Shoaib, “A new method for CDP input parameter identification of the ABAQUS software guaranteeing uniqueness and precision,” *IJSI*, vol. 8, no. 2, pp. 264–284, Apr. 2017, doi: 10.1108/IJSI-03-2016-0010.

[69] “Abaqus Documentation, Concrete Damaged Plasticity.” [Online]. Available: https://classes.engineering.wustl.edu/2009/spring/mase5513/abaqus/docs/v6.6/books/usb/default.htm?startat=pt05ch18s05abm36.html

[70] M. Szczecina and A. Winnicki, “Calibration of the CDP model parameters in Abaqus,” 2015. [Online]. Available: https://api.semanticscholar.org/CorpusID:138627326

[71] T. Hobbiebrunken, B. Fiedler, M. Hojo, and M. Tanaka, “Experimental determination of the true epoxy resin strength using micro-scaled specimens,” *Composites Part A: Applied Science and Manufacturing*, vol. 38, no. 3, pp. 814–818, Mar. 2007, doi: 10.1016/j.compositesa.2006.08.006.

[72] E. M. Odom and D. F. Adams, “Specimen size effect during tensile testing of an unreinforced polymer,” *J Mater Sci*, vol. 27, no. 7, pp. 1767–1771, 1992, doi: 10.1007/BF01107202.

[73] J. Misumi, R. Ganesh, S. Sockalingam, and J. W. Gillespie, “Experimental characterization of tensile properties of epoxy resin by using micro-fiber specimens,” *Journal of Reinforced Plastics and Composites*, vol. 35, no. 24, pp. 1792–1801, Dec. 2016, doi: 10.1177/0731684416669248.

[74] C.-M. Sanchez-Camargo, A. Hor, and C. Mabru, “A robust inverse analysis method for elastoplastic behavior identification using the true geometry modeling of Berkovich indenter,” *International Journal of Mechanical Sciences*, vol. 171, p. 105370, Apr. 2020, doi: 10.1016/j.ijmecsci.2019.105370.

[75] M. Herraez, “Computational Micromechanics Models for Damage and Fracture of Fiber-Reinforced Polymers - Tesis Doctoral,” UNIVERSIDAD POLITECNICA DE MADRID, 2018.

[76] G. P. Tandon, R. Y. Kim, and V. T. Bechel, “Interfacial Strength and Toughness Characterization Using a Novel Test Specimen,” in *Recent Advances in Experimental Mechanics*, E. E. Gdoutos, Ed., Dordrecht: Kluwer Academic Publishers, 2004, pp. 163–174. doi: 10.1007/0-306-48410-2_16.

[77] S. Ogihara and J. Koyanagi, “Investigation of combined stress state failure criterion for glass fiber/epoxy interface by the cruciform specimen method,” *Composites Science and Technology*, vol. 70, no. 1, pp. 143–150, Jan. 2010, doi: 10.1016/j.compscitech.2009.10.002.

[78] J. Koyanagi, P. D. Shah, S. Kimura, S. K. Ha, and H. Kawada, “Mixed-Mode Interfacial Debonding Simulation in Single-Fiber Composite under a Transverse Load,” *JMMP*, vol. 3, no. 5, pp. 796–806, 2009, doi: 10.1299/jmmp.3.796.

[79] T. J. Vaughan, “Micromechanical modelling of damage and failure in fibre reinforced composites under loading in the transverse plane,” 2011. [Online]. Available: https://api.semanticscholar.org/CorpusID:138225952

[80] J. Varna, L. A. Berglund, and M. L. Ericson, “Transverse single-fibre test for interfacial debonding in composites: 2. Modelling,” *Composites Part A: Applied Science and Manufacturing*, vol. 28, no. 4, pp. 317–326, Jan. 1997, doi: 10.1016/S1359-835X(96)00125-X.

[81] C. S. Lopes, P. P. Camanho, Z. Gürdal, P. Maimí, and E. V. González, “Low-velocity impact damage on dispersed stacking sequence laminates. Part II: Numerical simulations,” *Composites Science and Technology*, vol. 69, no. 7–8, pp. 937–947, Jun. 2009, doi: 10.1016/j.compscitech.2009.02.015.

[82] V. Cech, E. Palesch, and J. Lukes, “The glass fiber–polymer matrix interface/interphase characterized by nanoscale imaging techniques,” *Composites Science and Technology*, vol. 83, pp. 22–26, Jun. 2013, doi: 10.1016/j.compscitech.2013.04.014.

[83] C. Medina M, J. M. Molina-Aldareguía, C. González, M. F. Melendrez, P. Flores, and J. LLorca, “Comparison of push-in and push-out tests for measuring interfacial shear strength in nano-reinforced composite materials,” *Journal of Composite Materials*, vol. 50, no. 12, pp. 1651–1659, May 2016, doi: 10.1177/0021998315595115.

[84] A. Arteiro, G. Catalanotti, A. R. Melro, P. Linde, and P. P. Camanho, “Micro-mechanical analysis of the in situ effect in polymer composite laminates,” *Composite Structures*, vol. 116, pp. 827–840, Sep. 2014, doi: 10.1016/j.compstruct.2014.06.014.

[85] S. P. Shah and M. Maiarù, “Effect of Manufacturing on the Transverse Response of Polymer Matrix Composites,” *Polymers*, vol. 13, no. 15, p. 2491, Jul. 2021, doi: 10.3390/polym13152491.

[86] N. J. Pagano, G. A. Schoeppner, R. Kim, and F. L. Abrams, “Steady-state cracking and edge effects in thermo-mechanical transverse cracking of cross-ply laminates,” *Composites Science and Technology*, vol. 58, no. 11, pp. 1811–1825, Nov. 1998, doi: 10.1016/S0266-3538(98)00047-5.

[87] M. K. Ballard, W. R. McLendon, and J. D. Whitcomb, “The influence of microstructure randomness on prediction of fiber properties in composites,” *Journal of Composite Materials*, vol. 48, no. 29, pp. 3605–3620, Dec. 2014, doi: 10.1177/0021998313511654.

[88] D. U. Shah and P. J. Schubel, “Evaluation of cure shrinkage measurement techniques for thermosetting resins,” *Polymer Testing*, vol. 29, pp. 629–639, 2010, doi: https://doi.org/10.1016/j.polymertesting.2010.05.001.

[89] L. Khoun and P. Hubert, “Cure Shrinkage Characterization of an Epoxy Resin System by Two in Situ Measurement Methods,” *Polymer Composites*, vol. 31, pp. 1603–1610, 2010, doi: https://doi.org/10.1002/pc.20949.

[90] Y. Nawab, S. Shahid, N. Boyard, and F. Jacquemin, “Review: chemical shrinkage characterization techniques for thermoset resins and associated composites,” *Journal of Materials Science*, vol. 48, pp. 5387–5409, 2013, doi: https://doi.org/10.1007/s10853-013-7333-6.

[91] L. G. Zhao, N. A. Warrior, and A. C. Long, “A micromechanical study of residual stress and its effect on transverse failure in polymer–matrix composites,” *International Journal of Solids and Structures*, vol. 43, pp. 5449–5467, 2006, doi: https://doi.org/10.1016/j.ijsolstr.2005.08.012.

[92] S. L. Agius, M. Joosten, B. Trippit, C. H. Wang, and T. Hilditch, “Rapidly cured epoxy/anhydride composites: Effect of residual stress on laminate shear strength,” *Composites: Part A*, vol. 90, pp. 125–136, 2016, doi: https://doi.org/10.1016/j.compositesa.2016.06.013.

[93] N. Rabearison, Ch. Jochum, and J. C. Grandidier, “A FEM coupling model for properties prediction during the curing of an epoxy matrix,” *Computational Materials Science*, vol. 45, no. 3, pp. 715–724, 2009, doi: https://doi.org/10.1016/j.commatsci.2008.11.007.

[94] B. Seers, R. Tomlinson, and P. Fairclough, “Residual stress in fiber reinforced thermosetting composites: A review of measurement techniques,” *Polymer Composites*, vol. 42, pp. 1631–1647, 2021, doi: https://doi.org/10.1002/pc.25934.

[95] C. Kao and R. J. Young, “Assessment of interface damage during the deformation of carbon nanotube composites,” *J Mater Sci*, vol. 45, no. 6, pp. 1425–1431, Mar. 2010, doi: 10.1007/s10853-009-3947-0.

[96] P. Jannotti, G. Subhash, J. Zheng, and V. Halls, “Measurement of microscale residual stresses in multi-phase ceramic composites using Raman spectroscopy,” *Acta Materialia*, vol. 129, pp. 482–491, May 2017, doi: 10.1016/j.actamat.2017.03.015.

[97] K. Kollins, C. Przybyla, and M. S. Amer, “Residual stress measurements in melt infiltrated SiC/SiC ceramic matrix composites using Raman spectroscopy,” *Journal of the European Ceramic Society*, vol. 38, no. 7, pp. 2784–2791, Jul. 2018, doi: 10.1016/j.jeurceramsoc.2018.02.013.

[98] J. Nance *et al.*, “Measurement of Residual Stress in Silicon Carbide Fibers of Tubular Composites Using Raman Spectroscopy,” *Acta Materialia*, vol. 217, p. 117164, Sep. 2021, doi: 10.1016/j.actamat.2021.117164.

[99] D. R. Tallant, T. A. Friedmann, N. A. Missert, M. P. Siegal, and J. P. Sullivan, “Raman Spectroscopy of Amorphous Carbon,” 1997, pp. 37–48.

[100] A. Boukenter, E. Duval, and H. M. Rosenberg, “Raman scattering in amorphous and crystalline materials: a study of epoxy resin and DGEBA,” *Journal of Physics C: Solid State Physics*, vol. 21, pp. 541–547, 1998, doi: 10.1088/0022-3719/21/15/011.

[101] D. Tuschel, “Why are the Raman spectra of crystalline and amorphous solids different?,” *Spectroscopy*, vol. 32, pp. 26–33, 2017.

[102] M. Pick, R. Lovell, and A. H. Windle, “Detection of elastic strain in an amorphous polymer by X-ray scattering,” *Nature*, vol. 281, pp. 658–659, 1979, doi: https://doi.org/10.1038/281658a0.

[103] P. Predecki and CS. Barrett, “Stress Measurement in Graphite/Epoxy Composites By X-Ray Diffraction from Fillers,” *Journal of Composite Materials*, vol. 13(1), pp. 61–71, 1979, doi: https://doi.org/10.1177/002199837901300105.

[104] P. Predecki and CS. Barrett, “Detection of Moisture in Graphite/Epoxy Laminates by X-Ray Diffraction,” *Journal of Composite Materials*, vol. 16(4), pp. 260–267, 1982, doi: https://doi.org/10.1177/002199838201600401.

[105] J. A. Nairn and P. Zoller, “Matrix solidification and the resulting residual thermal stresses in composites,” *Journal of Materials Science*, vol. 20, pp. 355–367, 1985, doi: https://doi.org/10.1007/BF00555929.

[106] P. P. Parlevliet, H. E. N. Bersee, and A. Beukers, “Residual stresses in thermoplastic composites—A study of the literature—Part II: Experimental techniques,” *Composites Part A: Applied Science and Manufacturing*, vol. 38, pp. 651–665, 2007, doi: https://doi.org/10.1016/j.compositesa.2006.07.002.

[107] B. Andersson, A. Sjogren, and L. Berglund, “Micro- and meso-level residual stresses in glass-fiber/vinyl-ester composites,” *Composites Science and Technology*, vol. 60, pp. 2011–2028, 2000, doi: https://doi.org/10.1016/S0266-3538(00)00099-3.

[108] B. Winiarski and P. J. Withers, “Micron-Scale Residual Stress Measurement by Micro-Hole Drilling and Digital Image Correlation,” *Exp Mech*, vol. 52, no. 4, pp. 417–428, Apr. 2012, doi: 10.1007/s11340-011-9502-3.

[109] Q. T. L. Vu *et al.*, “Evaluating Residual Stress in Carbon Fiber-Reinforced Polymer (CFRP) at Microscale Using Fiber Push-Out Experiment and Finite Element Modeling,” *Polymers*, vol. 15, no. 12, p. 2596, Jun. 2023, doi: 10.3390/polym15122596.

[110] M. R. Kamal and S. Sourour, “Kinetics and Thermal Characterization of Thermoset Cure,” *Polymer Engineering and Science*, vol. 13, pp. 59–64, 1973, doi: https://doi.org/10.1002/pen.760130110.

[111] Q. Li, X. Li, and Y. Meng, “Curing of DGEBA epoxy using a phenol-terminated hyperbranched curing agent: Cure kinetics, gelation, and the TTT cure diagram,” *Thermochimica Acta*, vol. 549, pp. 69–80, 2012, doi: https://doi.org/10.1016/j.tca.2012.09.012.

[112] S. G. K. Schechter, L. K. Grunenfelder, and S. R. Nutt, “Air evacuation and resin impregnation in semipregs: effects of feature dimensions,” *Advanced Manufacturing: Polymer & Composites Science*, pp. 101–114, 2020, doi: https://doi.org/10.1080/20550340.2020.1768348.

[113] Grafil Inc., “PYROFIL ™ HS40 12K.” Accessed: Mar. 03, 2023. [Online]. Available: https://www.rockwestcomposites.com/downloads/HS40-12K_(07-2008).pdf

[114] S. Ghaffari, G. Seon, and A. Makeev, “Effect of Fiber–Matrix Interface Friction on Compressive Strength of High-Modulus Carbon Composites,” *Molecules*, vol. 28,2049, 2023, doi: https://doi.org/10.3390/molecules28052049.

[115] P. T. Goncalves, A. Arteiro, and N. Rocha, “Micro-mechanical analysis of the effect of ply thickness on curing micro-residual stresses in a carbon/epoxy composite laminate,” *Composite Structures*, vol. 319, p. 117158, Sep. 2023, doi: 10.1016/j.compstruct.2023.117158.

[116] L. P. Canal, C. González, J. M. Molina-Aldareguía, J. Segurado, and J. LLorca, “Application of digital image correlation at the microscale in fiber-reinforced composites,” *Composites Part A: Applied Science and Manufacturing*, vol. 43, no. 10, pp. 1630–1638, Oct. 2012, doi: 10.1016/j.compositesa.2011.07.014.

[117] A. D. Kammers and S. Daly, “Digital Image Correlation under Scanning Electron Microscopy: Methodology and Validation,” *Exp Mech*, vol. 53, no. 9, pp. 1743–1761, Nov. 2013, doi: 10.1007/s11340-013-9782-x.

[118] G. Seon, A. Makeev, J. Cline, and B. Shonkwiler, “Assessing 3D shear stress–strain properties of composites using Digital Image Correlation and finite element analysis based optimization,” *Composites Science and Technology*, vol. 117, pp. 371–378, Sep. 2015, doi: 10.1016/j.compscitech.2015.07.011.

[119] G. Seon, A. Makeev, J. D. Schaefer, and B. Justusson, “Measurement of Interlaminar Tensile Strength and Elastic Properties of Composites Using Open-Hole Compression Testing and Digital Image Correlation,” *Applied Sciences*, vol. 9, no. 13, p. 2647, Jun. 2019, doi: 10.3390/app9132647.

[120] J. Jäger, M. G. R. Sause, F. Burkert, J. Moosburger-Will, M. Greisel, and S. Horn, “Influence of plastic deformation on single-fiber push-out tests of carbon fiber reinforced epoxy resin,” *Composites: Part A*, vol. 71, pp. 157–167, 2015, doi: https://doi.org/10.1016/j.compositesa.2015.01.011.

[121] B. Rohrmüller, P. Gumbsch, and J. Hohe, “Calibrating a fiber–matrix interface failure model to single fiber push-out tests and numerical simulations,” *Composites Part A*, vol. 150, 2021, doi: https://doi.org/10.1016/j.compositesa.2021.106607.

[122] Instron, “2810 Series Mini Flexture Fixture”, [Online]. Available: https://www.instron.com/-/media/literature-library/products/2018/12/2810-series-mini-flexure-fixtures.pdf

[123] MatWeb, “Steels.” [Online]. Available: https://www.matweb.com/search/datasheet.aspx?bassnum=MS0001&ckck=1

[124] Engineering Toolbox, “Young Modulus.” [Online]. Available: https://www.engineeringtoolbox.com/young-modulus-d_417.html

[125] MatWeb, “Copper.” [Online]. Available: https://www.matweb.com/search/datasheet_print.aspx?matguid=9aebe83845c04c1db5126fada6f76f7e

[126] MatWeb, “PolyCarbonate.” [Online]. Available: https://www.matweb.com/search/DataSheet.aspx?MatGUID=501acbb63cbc4f748faa7490884cdbca

[127] MatWeb, “Polyethylene Terephthalate (PET).” [Online]. Available: http://www.matweb.com/search/datasheet.aspx?matguid=a696bdcdff6f41dd98f8eec3599eaa 20

[128] MatWeb, “Polystyrene, Extrusion Grade.” [Online]. Available: https://www.matweb.com/search/DataSheet.aspx?MatGUID=1c41e50c2e324e00b0c4e419ca780304&ckck=1

[129] MatWeb, “Acrylic, Cast.” [Online]. Available: http://www.matweb.com/search/datasheet.aspx?bassnum=O1303&ckck=1

[130] J. Heilman, “TBP Converting, Inc. 3M Acrylic Adhesives PDS.” [Online]. Available: https://tbpconverting.com/wp-content/uploads/2022/08/3M-Acrylic-Adhesives-DP8405NS-8410NS-DP8425NS.pdf

[131] A. M. G. Pinto, A. G. Magalhães, R. D. S. G. Campilho, L. F. M. Silva, J. A. G. Chousal, and A. P. M. Baptista, “Shear Modulus and Strength of an Acrylic Adhesive by the Notched Plate Shear

Method (Arcan) and the Thick Adherend Shear Test (TAST)," *MSF*, vol. 636–637, pp. 787–792, Jan. 2010, doi: 10.4028/www.scientific.net/MSF.636-637.787.

[132] B. Nečasová, P. Liška, J. Kelar, and J. Šlanhof, "Comparison of Adhesive Properties of Polyurethane Adhesive System and Wood-plastic Composites with Different Polymers after Mechanical, Chemical and Physical Surface Treatment," *Polymers*, vol. 11, no. 3, p. 397, Mar. 2019, doi: 10.3390/polym11030397.

[133] Songhan, "Cytec Thornel T-50 6K datasheet." [Online]. Available: http://www.lookpolymers.com/pdf/Cytec-Thornel-T-50-6K-Carbon-Fiber-Polyacrylonitrile-PAN-Precursor.pdf

[134] Toray, "T700S Datasheet." [Online]. Available: https://www.rockwestcomposites.com/media/wysiwyg/T700SDataSheet.pdf

[135] Toray, "T1000G data sheet." [Online]. Available: https://fileserver.mates.it/Prodotti/1_Rinforzi/TDS/Carbonio/Fibre/T1000G_DS.pdf

[136] Toray, "M40J datasheet." [Online]. Available: https://www.toraycma.com/wp-content/uploads/M40J-Technical-Data-Sheet-1.pdf.pdf

[137] Toray, "M50J datasheet." [Online]. Available: https://toray-cfe.com/wp-content/uploads/2020/12/toray-torayca-m50j-haut-module.pdf

[138] Toray, "M60J datasheet." [Online]. Available: https://www.toraycma.com/wp-content/uploads/m60j-datasheet-3b0af0e171322e8c.pdf

[139] HEXCEL, "HM63 datasheet." [Online]. Available: https://www.hexcel.com/user_area/content_media/raw/HM63_Aerospace_HexTow_DataSheet.pdf

[140] Mitsubishi Rayon Co., "Pyrofil MR 70 12P datasheet." [Online]. Available: https://northerncomposites.com/wp-content/uploads/2020/07/MR-70-12P20140204.pdf

Appendices

Appendix A: RVE implementation in Abaqus FEM simulation

The RVE can be used to determine homogenized composite properties from its components. In this appendix, the RVE is utilized to study elastic properties.

Inputs for the RVE include:

- Composite's Fiber Volume Fraction
- Fiber and Matrix elastic properties

Expected output:

- Composite system's Elastic properties

The procedure of FEM RVE analysis includes important steps:

1- Fiber positions are randomly generated on a surface, which is then projected into a 3D model of UD composite.

2- Input elastic properties of Fiber and Matrix. Interface between Fiber and Matrix is considered "perfect" and undamaged throughout the elastic simulation.

Table A1 presents the input elastic properties of IM7 carbon fiber and 8552 epoxy matrix considered in this study.

Table A 1. Elastic properties of IM7 carbon fiber and 8552 epoxy matrix.

	E_{11} (GPa)	E_{22} (GPa)	E_{33} (GPa)	ν_{12}	ν_{13}	ν_{23}	G_{12} (GPa)	G_{13} (GPa)	G_{23} (GPa)
IM7 carbon fiber	276	15.0	15.0	0.20	0.20	0.07	15.0	15.0	7.03
	E_m (GPa)	ν_m							
8552 epoxy matrix	4.67	0.39							

3- Periodic Boundary Conditions is applied on the RVE, using "dummy nodes" technique presented by Gomez [34]. On the original, undeformed model, mesh and nodes on opposite faces of the RVE are identical (i.e., "conformal meshes").

In Abaqus, keyword *EQUATION is applied to constrain movements of opposite nodes according to dummy nodes displacements. Thus, the homogenized strain is

applied over the opposite faces of the RVE and over the RVE itself (Figure A1). For a 2D RVE, movement equations are:

$$u_j^{BC} - u_j^{AD} = \bar{\varepsilon}_{xj}\Delta x = u_j^{RPX}$$
$$u_j^{DC} - u_j^{AB} = \bar{\varepsilon}_{yj}\Delta y = u_j^{RPY}$$

As a result, the strains ε_{ij} are correctly imposed on the RVE by definition. Application of the technique to a 3D RVE is similar.

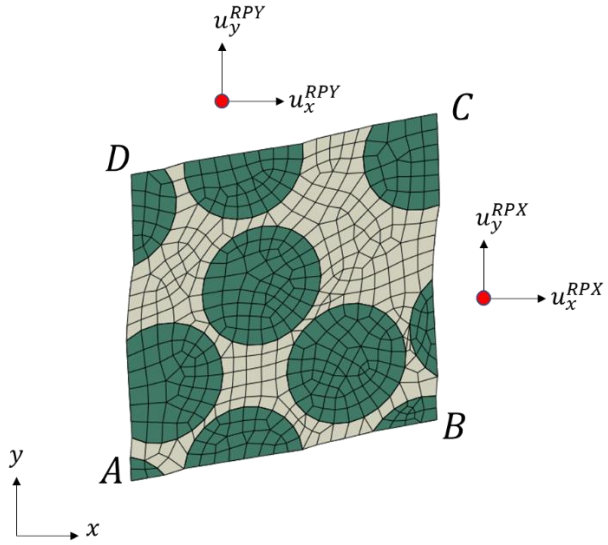

Figure A 1. Concept of “Dummy Nodes” to apply PBC on the RVE.

4- Strains of $\varepsilon_{11}, \varepsilon_{22}, \varepsilon_{33}, \varepsilon_{21}, \varepsilon_{31}, \varepsilon_{23}$ are imposed on the RVE. Stresses σ_{ij} are obtained via. Reaction Force on the dummy nodes divided by corresponding surface areas of the RVE. Strain values are very small ($\ll 1\%$) so there is little difference between Engineering Stress and True Stress.

A system of equations is then created thanks to various Strain and reaction Stress values, which permits determining the Stiffness Matrix $\overline{\overline{\boldsymbol{C}}}$:

$$\bar{\boldsymbol{\sigma}} = \overline{\overline{\boldsymbol{C}}}.\bar{\boldsymbol{\varepsilon}}$$

Inverting Stiffness Matrix $\overline{\overline{\boldsymbol{C}}}$, we obtain the Compliance Matrix $\overline{\overline{\boldsymbol{S}}}$:

$$\bar{\boldsymbol{\varepsilon}} = \overline{\overline{\boldsymbol{S}}}.\bar{\boldsymbol{\sigma}}$$

which can be written in terms of Global/Equivalent Elastic parameters:

$$\begin{Bmatrix} \varepsilon_{11} \\ \varepsilon_{22} \\ \varepsilon_{33} \\ \gamma_{23} \\ \gamma_{13} \\ \gamma_{12} \end{Bmatrix} = \left[\begin{array}{ccc|ccc} \frac{1}{E_{11}} & \frac{-\nu_{21}}{E_{22}} & \frac{-\nu_{31}}{E_{33}} & 0 & 0 & 0 \\ \frac{-\nu_{12}}{E_{11}} & \frac{1}{E_{22}} & \frac{-\nu_{32}}{E_{33}} & 0 & 0 & 0 \\ \frac{-\nu_{13}}{E_{11}} & \frac{-\nu_{23}}{E_{22}} & \frac{1}{E_{33}} & 0 & 0 & 0 \\ \hline 0 & 0 & 0 & \frac{1}{G_{23}} & 0 & 0 \\ 0 & 0 & 0 & 0 & \frac{1}{G_{13}} & 0 \\ 0 & 0 & 0 & 0 & 0 & \frac{1}{G_{12}} \end{array}\right] \times \begin{Bmatrix} \sigma_{11} \\ \sigma_{22} \\ \sigma_{33} \\ \sigma_{23} \\ \sigma_{13} \\ \sigma_{12} \end{Bmatrix}$$

Then we can calculate directly Global elastic properties $E_{11}, E_{22}, E_{33}, G_{23}, G_{13}, G_{12}, \nu_{12}, \nu_{13}, \nu_{23}$.

5- RVE size and mesh convergence study on Elastic Properties. For each RVE size, ten different random fiber distributions are generated and studied. Fiber volume fraction is 60%. For the IM7/8552 CFRP, results in Table A2 show that Convergence of Elastic Properties is obtained with a relatively small RVE of 5-fiber-radius cross-section, containing 5 fibers. For Damage assessment however, a RVE with size of ~ 50 times Fiber Radius should be used [38], [39].

Table A 2. RVE size convergence study. COV: Coefficient of variation over 10 random fiber distributions.

Fibers in RVE	RVE cross section (in R_f)		E_{11} (GPa)	E_{22} (GPa)	E_{33} (GPa)	ν_{12}	ν_{13}	ν_{23}	G_{12} (GPa)	G_{13} (GPa)	G_{23} (ksi)
5	5	mean	167	9.72	9.72	0.276	0.276	0.377	5.05	5.03	3.67
		COV	0.036%	0.33%	0.34%	0.66%	0.65%	0.53%	2.5%	2.6%	0.4%
43	15	mean	167	9.86	9.86	0.276	0.276	0.370	5.03	5.02	3.62
		COV	0.003%	0.57%	0.56%	0.40%	0.40%	0.96%	1.2%	1.1%	0.8%
150	28	mean	165	9.86	9.86	0.277	0.277	0.368	5.02	4.98	3.59
		COV	0.001%	0.44%	0.44%	0.28%	0.28%	0.77%	0.9%	0.9%	0.6%

Appendix B: Bending Beam method for fiber longitudinal compression strength measurement, design and evaluations

The Bending Beam is proposed as the preferred experimental method for measurement of carbon fiber longitudinal compressive critical strain ε_{c11}^{o} and strength σ_{c11}^{o} due to its relative simplicity and robustness. This Appendix presents a detailed analytical analysis which demonstrates the method feasibility and provides recommendations for the realization of the Bending Beam method.

Analytical analysis for Experiment Design Requirements

In this analysis, beam's deformation is supposed small, elastic and linear. Figure A2 provides an illustration of the analyzed variables.

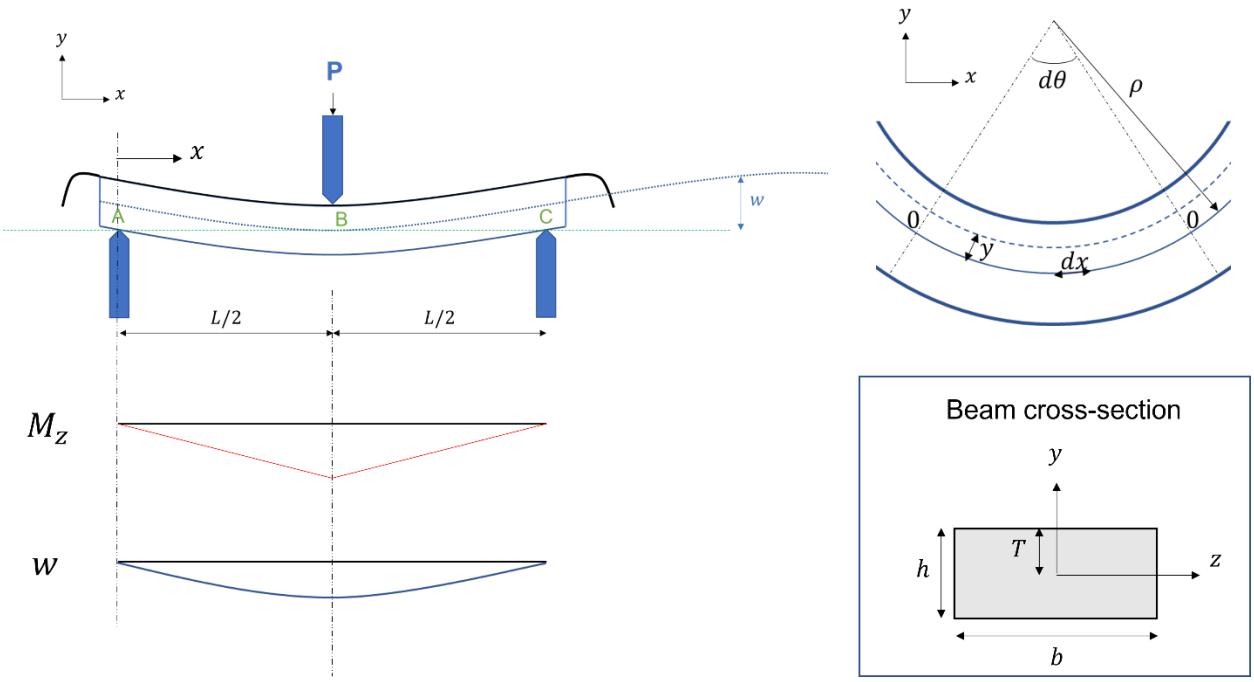

Figure A 2. Illustration of terms in the Bending Beam analysis.

Given the beam deflection $w = f(x)$, radius of curvature ρ at a section of the beam:

$$\frac{1}{\rho} = \frac{w''}{[1 + (w')^2]^{\frac{3}{2}}}$$

If y' and y is small, then: $\frac{1}{\rho} \approx w''$

Given the beam's initial, undeformed length L_0 between the fixtures A and C (Figure A2). We consider a short beam section of initial, undeformed beam length dL_0. Suppose that the beam is under pure bending which can be achieved by using low-friction fixtures, we have the constant relation at the neutral axis: $\rho \times d\theta = dL_0$. For an axis at distance y from the neutral axis, then radius of curvature at y is $(\rho - y)$ i.e., corresponding axis length at y is given by:

$$dL = (\rho - y)d\theta$$

So, the local longitudinal strain is:

$$\varepsilon_x = \frac{dL - dL_0}{dL_0} = \frac{(\rho - y)d\theta - \rho d\theta}{\rho d\theta} = -\frac{y}{\rho} \quad (12)$$

If there is no lateral stress/load acting on the elastic beam, then local **longitudinal stress** is simply:

$$\sigma_x = E\varepsilon_x = -\frac{Ey}{\rho} \quad (13)$$

Bending Moment equation:

$$M_z = \frac{EI_{zz}}{\rho} \quad (14)$$

If Bending is small and curvature $w' \ll 1$ then:

$$M_z = EI_{zz}w''$$

Combining (13) and (14), then we have:

$$\sigma_x = -\frac{M_z y}{I_{zz}}$$

$$\varepsilon_x = \frac{\sigma_x}{E} = -\frac{M_z y}{EI_{zz}}$$

We apply these equations on a 3-point bending schema, we consider only half of the beam thanks to the symmetry, where the deflection moment is:

$$M_z(x) = \frac{Px}{2} \; for \; 0 \leq x \leq \frac{L_0}{2}$$

The maximum Moment exerted on the beam is therefore:

$$M_z\left(\frac{L}{2}\right) = \frac{PL_0}{4}$$

At distance y from neutral axis, **longitudinal strain** is:

$$\varepsilon_x(x,y) = -\frac{M_z y}{EI_{zz}} = -\frac{Px}{2} \times \frac{y}{EI_{zz}}$$

We deduce strain at the surface, where $y = T = h/2$:

$$\varepsilon_x(x,T) = -\frac{Px}{2} \times \frac{T}{EI_{zz}}$$

For a beam with rectangular cross-section of "width" b and "height/thickness" h:

$$I_x = \frac{bh^3}{12}$$

Numerical application: $T = h/2$ then strain at the upper beam surface is:

$$\varepsilon_x(x, T = h/2) = -\frac{Px}{2} \times \frac{\frac{h}{2}}{\frac{Ebh^3}{12}} = -\frac{3Px}{Ebh^2} \qquad (15)$$

With equation (15), compressive strain of the upper beam surface, and of the bonded carbon fiber, can be directly deduced from easily obtainable measurements: Load, position of the fiber damage limit, beam material Modulus, beam cross-section dimensions.

We can deduce maximum compressive strain which occurs at beam length center B where the load P is applied:

$$\varepsilon_{max} = \varepsilon_x(x = L_0/2, T = h/2) = -\frac{3}{2} \times \frac{PL}{Ebh^2} \qquad (16)$$

i.e.

$$P = -\frac{2}{3}\,\varepsilon_{max}\frac{Ebh^2}{L} \tag{17}$$

$$\varepsilon_x = \varepsilon_{max} \times \frac{2x}{L} \tag{18}$$

Equation (16) provides an engineering requirement for the Beam material, since the material has to accommodate at least the critical compressive strain of the fiber. Equation (17) provides the requirement for the Load capacity of the 3-point testing machine. Equation (18) provides a quick relation for the calculation of bonded fiber critical compressive strain based on the position of its damage limit.

Finally, we want to verify maximum beam deflection, so that the condition of "small beam deflection" is satisfied. Maximum deflection happens at the middle of beam length (Load point B, Figure A2):

$$w_{\frac{L}{2}} = \frac{PL^3}{48EI} = \frac{PL^3}{\frac{48Ebh^3}{12}} = \frac{PL^3}{4Ebh^3} = -\frac{1}{6}\varepsilon_{max}\frac{\mathrm{L}^2}{\mathrm{h}}$$

Therefore, we have maximum compressive strain: $\varepsilon_{max} = 6\,w_{max}\frac{h}{L^2}$

For small beam deflection, the ratio of deflection over corresponding length should be less than 10%:

$$C_{small} = \left|\frac{W_{\frac{L}{2}}}{L/2}\right| = \frac{1}{3}\varepsilon_{max}\frac{L}{h} < 0.1 \tag{19}$$

The inequation (19) provides criteria to select Bending Beam dimensions of length L and thickness h.

Now we study the forces acting on the bonded fiber. Local beam strain is transmitted into the fiber through shear force at the interface. The analysis provides estimation of the maximum shear stress acting on the fiber, so a proper bonding

adhesive can be selected. Figure A3 shows forces acting on a short section dl of bonded fiber.

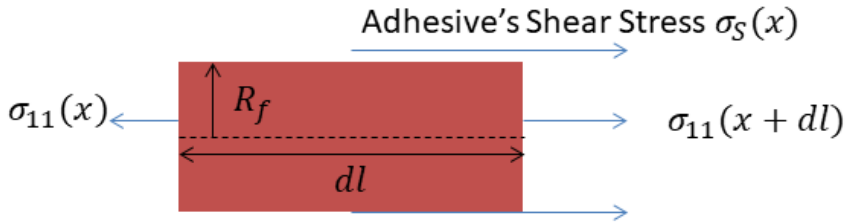

Figure A 3. Forces acting on a short section dl of bonded fiber in Bending Beam test.

Main forces are the longitudinal normal stress $\sigma_{11}(x)$ and adhesive shear stress $\sigma_S(x)$. The section is static so the total longitudinal force is zero:

$$\Sigma F = \pi R_f^2\big(\sigma_{11}(x+dl) - \sigma_{11}(x)\big) + 2\pi R_f dl.\sigma_S(x) = 0$$

We deduce the local shear stress:

$$\sigma_S(x) = -\frac{R_f}{2}\frac{\partial\sigma_{11}(x)}{\partial x} \qquad (20)$$

From equation (15): $\varepsilon_{11}(x) = -\frac{3Px}{Ebh^2}$

and we assume the fiber to be perfectly elastic, with longitudinal modulus E_{11}:

$$\sigma_{11}(x) = E_{11}\varepsilon_{11}(x) = -\frac{3Px}{bh^2}\frac{\mathrm{E}_{11}}{\mathrm{E}}$$

$$\rightarrow \frac{\partial\sigma_{11}(x)}{\partial x} = -\frac{3P}{bh^2}\frac{E_{11}}{E} \qquad (21)$$

From equations (20) and (21), we can calculate adhesive shear force acting on the fiber:

$$\sigma_S(x) = \frac{3}{2}R_f\frac{P}{bh^2}\frac{E_{11}}{E} = -R_f\frac{E_{11}}{L}\,\varepsilon_{max} \qquad (22)$$

It is interesting to note that under given simplifications, shear force is uniform along bonded fiber length.

Example of numerical application for engineering requirements

Assuming an example configuration for the Bending Beam of:

- Dimensions: $(length, thickness, width) = (100\ mm, 10\ mm, 20\ mm)$. The ratio $\frac{length}{thickness}$ should be higher than ten (10) for a valid slender beam assumption.
- Objective maximum fiber compressive strain $\varepsilon_{11}\left(\frac{L}{2}\right) = 2\%$.

The Bending Beam is proposed to be made of PolyCarbonate, which allows high elastic strains and is ductile (details presented in Table A3).

The maximum shear stress at fiber-adhesive interface is calculated to be $0.141\ MPa$, well below shear strength of the Acrylic and Urethane adhesives (Table A4).

The maximum Load required by the 3-point bending heads is 629 Newtons, well within the capacity of the popular 2kN bending beam machine [122].

Other considerations

To avoid interference with fiber damage development, the head of the 3-point bending should avoid touching/pushing on the bonded fiber area. This can be achieved using a head with a middle groove allowing the fiber area “passing through”.

The method can be combined with DIC and FEM analysis to confirm strains developed and compare with analytical predictions.

During the specimen preparation, the fiber is typically straightened using a small weight, creating a pre-tension. The pre-tension as well as the weight should not be too high to significantly interfere with experimental results. Regarding the reference IM7 carbon fiber, one individual fiber can withstand approximately $10\ gram$ tension load. A hanging mass of $0.1\ gram$ would lead to a pre-tension of $\varepsilon_{pre} = 0.017\%$ on the fiber. For comparison, the critical tension strain of the IM7 fiber is $\varepsilon_{t11}^{o} = 2\%$.

Bending Beam Material

The table A3 below presents some potential materials for Bending Beam's material, along with their important properties: Young Modulus E, Yield Stress σ_y and estimated Yield Strain $\varepsilon_y = \sigma_y/E$. For critical yield strain estimation, Compressive Modulus is used when available. Otherwise, the more frequently provided Tensile Modulus is used for estimation.

Amongst the listed materials, only PolyCarbonate (PC) possesses Yield Strains in both tension and compression that respond to our criterion ($\varepsilon_y > 2\%$), and is ductile. Finally, the PolyCarbonate material is inexpensive and widely available.

Table A 3. Potential materials for the Bending Beam.

Beam Material	E_t (GPa)	E_c (GPa)	σ_{yt} (MPa)	σ_{yc} (MPa)	ε_{yt}	ε_{yc}	Ductile/ Brittle?	Ref
Steel, general	200		350		0.18%		Ductile	[123]
Aluminum	69		95		0.14%		Ductile	[124]
Copper	110		33		0.03%		Ductile	[125]
PolyCarbonate	2.36		63.3	65.7	**2.68%**	**2.78%**	Ductile	[126]
PETE	3.10		63.6	45.2	2.05%	1.46%	Ductile	[127]
Polystyrene	2.98		36.1		1.21%		Ductile	[128]
Acrylic	3.10	2.96	65	120	2.10%	4.05%	Brittle	[129]

Adhesive for Fiber-Beam bonding

Deteresa et al. [46] bonded fibers to the PC beam using a clear Acrylic spray coating. Fidan [59] utilized Urethane spray coating (MS470). Table A4 presents some strength properties of the Acrylic and Urethane adhesives.

Using the analytical formula for shear stress at bonded fiber interface (Equation 22), adhesive shear stress in the experiment by Deteresa et al. [46] is estimated at $0.126\,MPa$, well below the shear strength of the adhesive that was used in their experiment.

Table A 4. Shear strength of suggested adhesive for fiber bonding on Bending Beam.

Adhesive	Shear Strength at room temperature, film (MPa)
Acrylic	6.9 [130] , 8.0 [131] - depending on specific type
Urethane	5.5 [132]

Conclusions on the Bending Beam method

The Bending Beam method is proposed to measure carbon fiber critical compression strain. An analytical analysis was performed to demonstrate the feasibility and provide some preliminary engineering requirements of the experiment. An example of the Bending Beam features was proposed and demonstrated to satisfy all requirements of the experiment.

Appendix C: Review: longitudinal properties of some carbon fibers

Table A5 presents single-fiber compressive properties of several notable Carbon Fibers frequently mentioned in articles from UTA and elsewhere from the literature.

The Compressive Strength σ_{c11}^{o}, when available, is cited along with experimental measurement method.

Table A 5. Longitudinal properties of selected carbon fibers from literature. MC*: obtained using Micro-Compression method. BB*: obtained through Bending Beam method. For critical strain values: Pr*: provided by datasheet, if available.

Fiber	Tensile Modulus E(GPa)	Tensile Strength σ_{t11}^{o} (GPa)	Critical Tensile Strain $\varepsilon_{t11}^{o} = \sigma_{t11}^{o}/E_t$	**Compressive Strength $\boldsymbol{\sigma_{c11}^{o}}$ (GPa)**	**Critical Compressive Strain $\boldsymbol{\varepsilon_{c11}^{o} = \sigma_{c11}^{o}/E_t}$**
T300	230 [41]	3.53 [41]	1.53%	1.8 ($\pm$16.9%) [52] (MC*)	0.78%
T50	393 [59] 390 [133]	2.9 [133]	0.74% 0.6% (Pr*) [133]	4.09 [59] (BB*)	1.04% $\pm$ .08% [59]
T700S	230 [134]	4.9 [134]	2.13%	2.4 ($\pm$15.6%) [52] (MC*)	1.04%
T800 H	294 [42]	5.49 [42]	1.87%	2.3 ($\pm$14.6%) [52] (MC*)	0.78%
T1000	294 [135]	6.37 [135]	2.17%	2.8 ($\pm$18.8%) [52] (MC*)	0.95%
M40J	377 [136]	4.4 [136]	1.17%	1.8 ($\pm$13%) [52] (MC*)	0.48%
P75S	517 [59]	N/A		2.69 [59] (BB*)	0.52% $\pm$.07% [59]
M50J	475 [137]	4.12 [137]	0.87%	1.3 ($\pm$15.5%) [52](MC*)	0.27%
M60J	588 [138]	3.82 [138]	0.65%	1.0 ($\pm$13.9%) [52] (MC*)	0.17%
IM7	276 [40]	5.516 [40]	2.00%	N/A	N/A
HM63	435 [139]	4.826 [139]	1.11%	N/A	N/A
HS40	455 [113]	4.61 [113]	1.01%	N/A	N/A
MR70	325 [140]	7.0 [140]	2.16%	N/A	N/A

Fiber Critical Tensile Strain is estimated from frequently provided Tensile Strength and Tensile Modulus: $\varepsilon_{c11}^{o} = \sigma_{c11}^{o}/E_t$. In fact, this Critical Tensile Strain is very close to the value provided by the Fiber manufacturer when this parameter is available. This confirms the fragile nature of the Carbon Fiber, at least in tension.

There is currently no established method to measure directly a single fiber's Compressive Modulus E_c. Therefore, when **Critical Compressive Strength $\boldsymbol{\sigma_{c11}^{o}}$ is directly measured** (as the case with Micro-Compressive Method), its Critical Compressive Strain is estimated with Tensile Modulus E_t: $\varepsilon_{c11}^{o} = \sigma_{c11}^{o}/E_t$.

Inversely, in the **Bending Beam** method, the **experiment actually determines Critical Compressive Strain** $\boldsymbol{\varepsilon_c^{crit}}$. Then the authors estimate Critical Compressive stress using Fiber Tensile modulus:

$$\sigma_{c11}^{o} = \varepsilon_{c11}^{o} \times E_t$$

In some cases, datasheets provide Fiber Critical Tensile Strain. In such cases, in addition to the estimated value using the above formulae, the value is noted (Pr*) along with citation to the document.

Table A6 compares Composite critical strain with its corresponding Base Fiber's critical strain, for the fiber types in Table A5. Fiber Critical Compressive Strain from Table A5 is provided in the last column of Table A6 for quick reference and comparison. Typically, Composite compressive strength is provided. Composite critical compressive strain is estimated by dividing strength over modulus:

$$\varepsilon_c = \sigma_c / E$$

If Compressive Modulus E_c is provided, the above formula applies $E = E_c$, and in Table A6 the Modulus is also marked with "(comp)".

Else if Compressive Modulus E_c is unavailable and only Tensile Modulus E_t is available, the above formula applies $E = E_t$, and in Table A6 the Modulus is marked with "(tens)".

Table A 6. Longitudinal properties of selected CFRP composites, corresponding to fibers from Table A5. “comp”: compressive property; “tens”: tensile property.

Base Fiber	Composite Compressive Strength σ_c (GPa)	Composite Modulus E (GPa)	**Composite Critical Compressive Strain** $\varepsilon_c = \sigma_c/E$	**Base Fiber Critical Compressive Strain**
T300	1.57 [41]	125 (comp) [41]	1.18%	0.78%
T50	N/A	N/A	N/A	1.04%
T700S	1.47 [134]	125 (tens) [134]	1.18%	1.04%
T800H	1.57 [42]	145 (comp) [42]	1.08%	0.78%
T1000	1.57 [135]	165 (tens) [135]	0.95%	0.95%
M40J	1.27 [136]	226 (tens) [136]	0.56%	0.48%
P75S	N/A	N/A	N/A	0.52%
M50J	0.98 [137]	295 (tens) [137]	0.33%	0.27%
M60J	0.79 [138]	360 (tens) [138]	0.22%	0.17%
IM7	1.689 [40]	150 (comp) [40]	1.13%	N/A
HM63	1.31 [139]	221 (comp) [139]	0.59%	N/A
HS40	1.31 [113]	241 (comp) [113]	0.54%	N/A
MR70	N/A	N/A	N/A	N/A

Appendix D: Mesh and size convergence studies for Residual Stress Analysis using Fiber Push-Out experiment [109]

The mesh and size convergence analyses utilizes the reference FE geometry (Figure A5). Reference in-plane size is $30\ \mu m \times 40\ \mu m$. Convergence studies utilize the measurement of matrix sink-in following fiber push-out.

The FE model meshing utilizes three parameters (Figure A4): in-plane inner mesh density; in-plane outer mesh density; and through-thickness number of elements. A denser inner mesh around the push-out fibers allows efficient evaluation of the interested area. Mesh convergence is considered achieved when a doubled mesh density leads to less than 2% variation in matrix sink-in. Figures A6.a, b, c present the results of the mesh convergence studies. The following reference configuration was found to satisfy the convergence criterion: four (4) elements per μm^2 for the inner mesh, one (1) element per μm^2 for the outer mesh, and ten (10) elements through the membrane thickness.

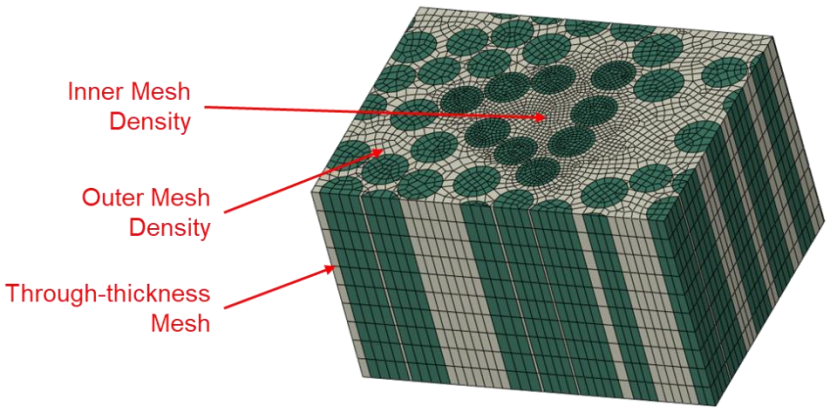

Figure A 4. Mesh parameters of the FE Model.

To evaluate model size convergence, each smaller-sized geometry is a rectangle central slice from a bigger-sized geometry, as illustrated in Figure A5. Size convergence analysis results are presented in Figure A6, suggesting that the presented FE model size convergence is achieved at a relatively small reference size that covers the push-out fibers and an outward in-plane expansion by a few fiber-diameters [109].

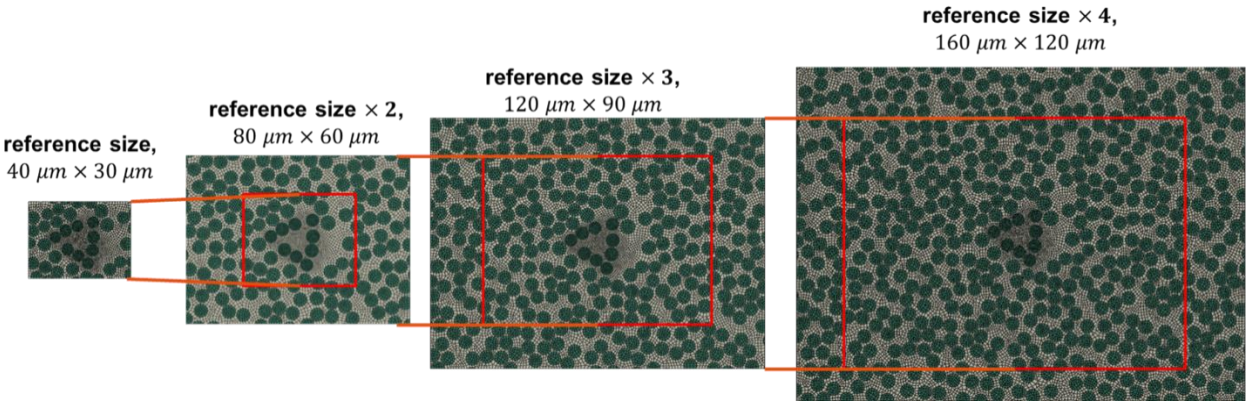

Figure A 5. Some FE models of different sizes for the convergence study.

Figure A7 reports the computation time for the mesh and size convergence studies. 11 CPUs of the Intel Xeon Processor X5650 were utilized in these analyses. The reference model took approximately 8 minutes, while the largest model took approximately 100 minutes.

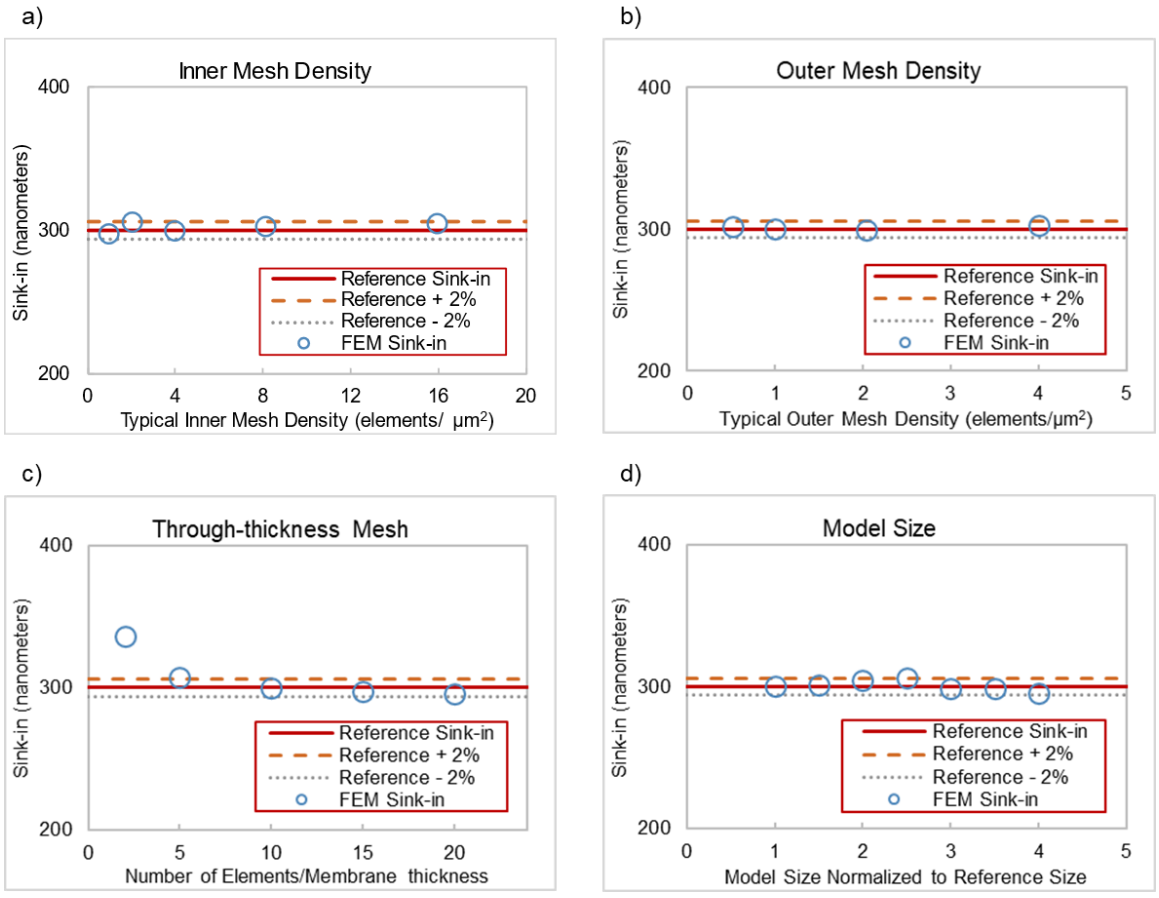

Figure A 6. Convergence analysis results: a) Inner mesh density; b) Outer mesh density; c) Through-thickness mesh; d) Model size. [109]

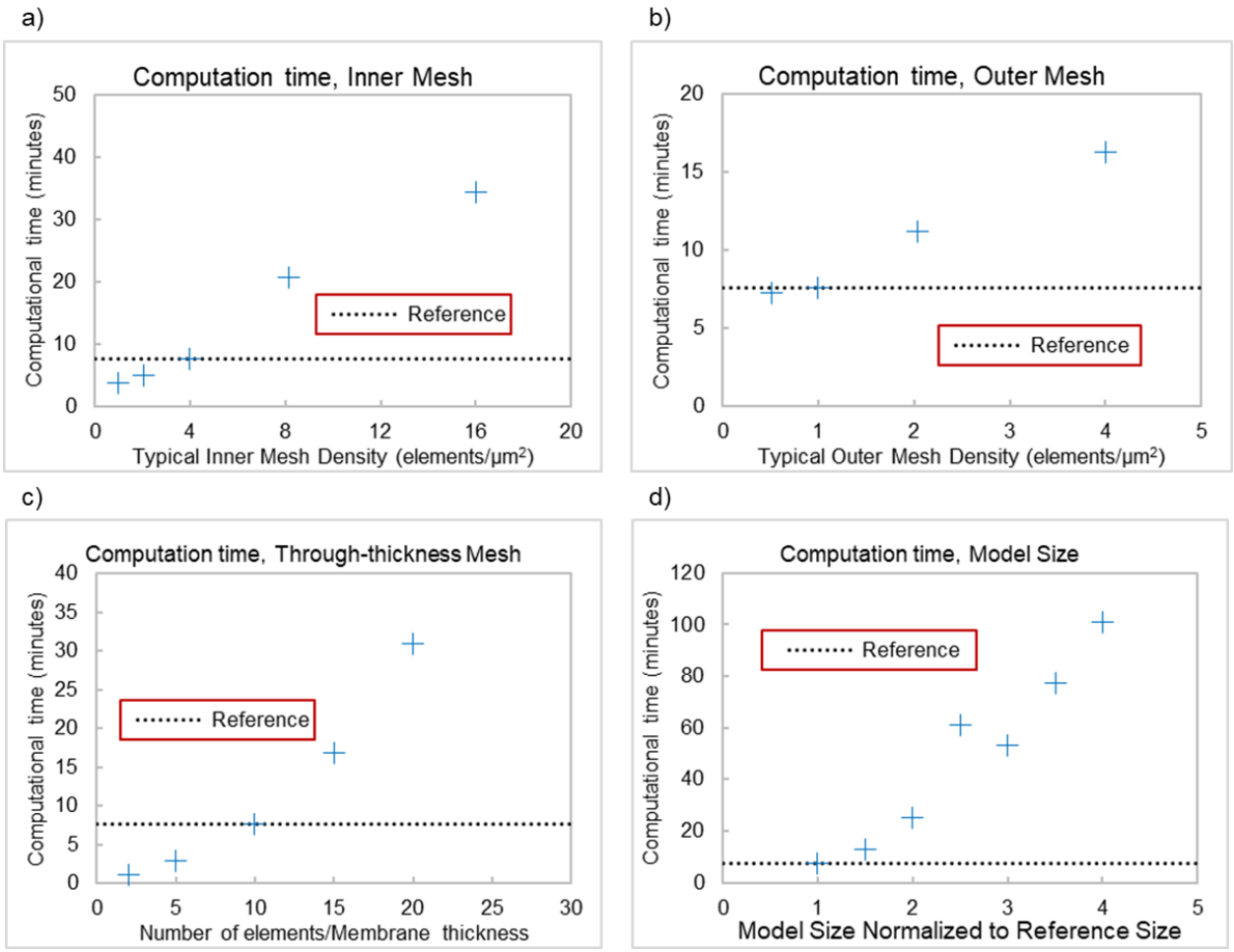

Figure A 7. Computation time for the convergence analyses: a) Inner mesh density; b) Outer mesh density; c) Through-thickness mesh; d) Model size. [109]

Appendix E: Size convergence analysis of Residual Stress to validate the application of far-field Boundary Conditions on micromodels [109]

To validate the application of far-field constraint-free boundary conditions at the in-plane limits of the FE micromodel during the curing stage, a size convergence analysis is conducted on the residual stress at the end of the curing process. The residual stress is examined across models with varying in-plane dimensions. The study analyzes the average residual stress generated in a Probed matrix volume containing matrix elements situated beneath the probed area (Figure A8.a), and the average residual stress across the entire matrix volume (Figure A8.c). The volume-averaged in-plane stresses Sxx, Syy and the through-thickness stress Szz are presented in Figure A8.b for the probed volume, and in Figure A8.d for the entire matrix volume. For some models of different sizes, on an in-plane cross-section cut through the midpoint of membrane thickness, Figure A9 visualizes the distribution of von Mises residual stress in the local fiber push-out area.

Within both the local probed volume and the entire matrix volume, convergence of residual stress is observed as the model size increases. The size of the FE model shows only a weak influence on the distribution of von Mises stress in the locality of the push-out area. These results suggest that with the application of the proposed boundary conditions (BCs), generated residual stress would be consistent irrespective of the model size. Through inductive inference, applying the far-field in-plane BCs of the macroscale specimen to the micromodel, starting from a certain minimum size, is valid for the purpose of residual stress analysis.

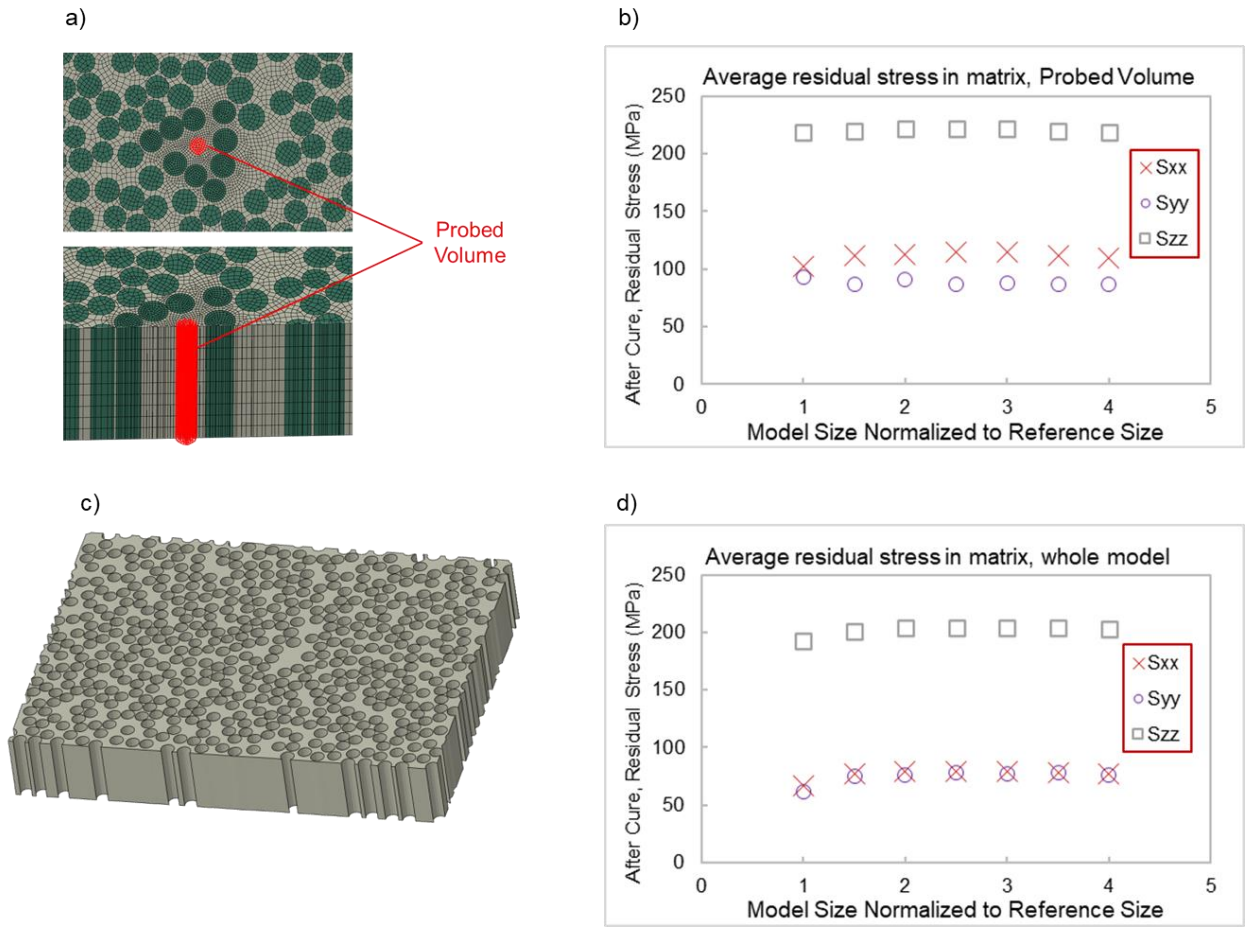

Figure A 8. a) Probed matrix Volume: matrix elements beneath the probed area; b) Average residual stress after curing within Probed Volume; c) Entire matrix volume; d) Average residual stress after curing within entire matrix volume. [109]

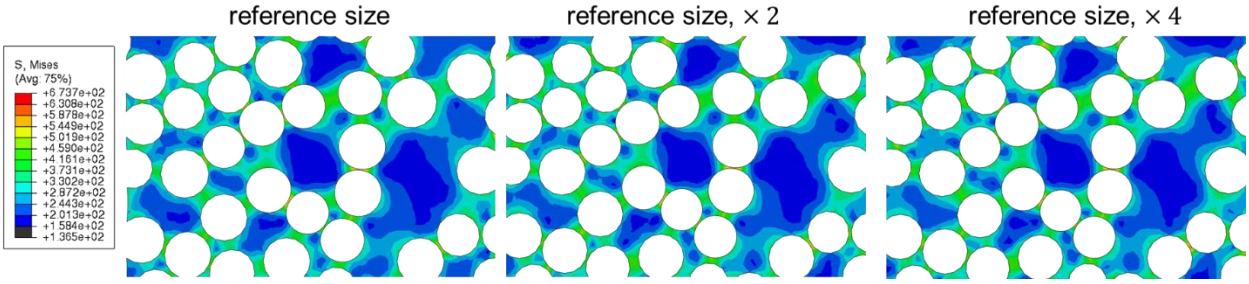

Figure A 9. After curing: von Mises residual stress within the central push-out region, observed on an in-plane cross-section positioned at the midpoint of the membrane thickness. Results are shown for several evaluated model sizes. [109]